Svein Arne Aase

Methods for improving quality and efficiency in quantitative echocardiography

- Aspects of using high frame rate

Thesis for the degree of philosophiae doctor

Trondheim, February 2008

Norwegian University of Science and Technology
Faculty of Medicine
Department of Circulation and Medical Imaging

NTNU
Norwegian University of Science and Technology

Thesis for the degree of philosophiae doctor

Faculty of Medicine
Department of Circulation and Medical Imaging

ISBN 978-82-471-6972-8 (printed version)
ISBN 978-82-471-6986-5 (electronic version)
ISSN 1503-8181

Doctoral theses at NTNU, 2008:53

Printed by NTNU-trykk

Metoder som forbedrer kvalitet og effektivitet i kvantitativ ultralyd av hjertet - aspekter ved bruk av høy datarate

Ultralyd er i dag et standardverktøy innen hjertediagnostikk. Analyse av ventrikkelfunksjon gjøres subjektivt ved å se på gråskala ultralydopptak av hjertet. Dette gjør dokumentasjon og opplæring vanskelig. Det er derfor ønskelig med kvantitative mål på ventrikkelfunksjon. Kvantitative metoder kan benytte høy tidsoppløsning og dermed også registrere flere detaljer. To teknikker for kvantitativ ventrikkelanalyse er vevs-Doppler og speckle tracking (mønsterfølging). Ved bruk av disse teknikkene er det viktig å sikre kvaliteten av resultatene samtidig som analyseprosessen kan gjennomføres så effektivt som mulig. I denne avhandlingen presenteres flere metoder for å sikre kvalitet og øke effektivitet ved kvantitativ ventrikkelanalyse som alle er relatert til bruk av høy tidsoppløsning.

For å kunne gjøre effektiv ventrikkelanalyse behøves analyseverktøy. Et slikt verktøy som fungerer med både vevs-Doppler og speckle tracking presenteres i denne avhandlingen. Dette verktøyet har gjort flere store kliniske studier mulig. Ved analyse av hendelsene som skjer innen en hjertesykel er det viktig å dele opp hjertesykelen i ulike faser. Venstre ventrikkels tømmingsfase avsluttes ved at aortaklaffen lukkes, og denne hendelsen må derfor bestemmes før kvantitative parametre i slutten av tømmingsfasen og i overgangen til fyllingsfasen kan bestemmes. I denne avhandlingen vurderes og testes ulike kandidater for bestemmelse av lukkingen. To gunstige kandidater i hastighetskurver fra basale deler av ventrikkelen ble funnet: andre nullkryssing etter tømming og høyeste positive akselerasjon etter tømming før fylling. Et eget bidrag viser at den siste av disse kan bestemmes automatisk. For å oppnå høy tidsoppløsning kreves høy datarate. En populær metode for å øke datarate er flere parallelle mottaksstråler for hver sendestråle. I vanlig gråtoneavbilding av hjertet er det imidlertid observert at dette medfører uønskede linjelignende strukturer i bildet. I denne avhandlingen vises det at årsaken til dette er at de parallelle strålene deformeres når de passerer strukturene mellom hjertet og proben. Avhandlingen inneholder også et bidrag som viser hvordan bruk av parallelle mottakstråler kan medføre at vevs-Doppler kurver blir hentet fra et annet sted i hjertet enn det intensjonen var. Samlet er avhandlingen et bidrag til fortsatt utvikling og forbedring av kvantitative ultralydmetoder innen hjertediagnostikk.

Svein Arne Aase
Institutt for sirkulasjon og bildediagnostikk, NTNU
Hovedveileder: Hans Torp, Biveileder: Asbjørn Støylen

Ovennevnte avhandling er funnet verdig til å forsvares offentlig for graden philosophiae doctor (PhD) i medisinsk teknologi. Disputas finner sted i auditoriet, medisinsk teknisk forskningssenter, onsdag 27. februar 2008 kl. 12:15.

Abstract

Echocardiography is a well established method for assessing cardiac function and health. Quantitative methods in echocardiography are much desired, as operator independence, training and reporting are expected to improve with such methods. Such methods are also expected to reveal details of cardiac function not visible to the human eye in real-time. Two promising quantitative methods for evaluation of left ventricular function are tissue Doppler imaging (TDI) and speckle tracking. In the implementation and use of quantitative methods, two challenges quickly appear: The challenge of maintaining good quality of the resulting parameters and the challenge of making the analysis process as efficient as possible. In this thesis several contributions to both challenges that are all related to high temporal resolution are presented.

To support a rapid analysis process, an automated analysis system is of great importance. A functional analysis of the left ventricle includes the analysis of 16 segments. To do so in many patients requires automation of as many tasks as possible. In this thesis an automated system for myocardial deformation analysis is presented. This system has enabled several clinical studies on large materials.

Aortic valve closure (AVC) is of special importance in automated myocardial analysis systems. AVC is needed because the cardiac cycle must be segmented into the different cardiac phases before parameters such as end-systolic strain and peak-systolic strain rate can be extracted. Two thesis chapters address AVC detection. In the first, it is shown that AVC can indeed be detected automatically in TDI velocity/time curves. The second shows that the time point of peak positive acceleration after ejection before early filling is a suitable event marker of AVC in TDI velocity/time curves. The initial negative velocity after ejection is shown to be a faulty marker of AVC.

Several approaches for achieving high frame rates exist. One popular approach is multiple line acquisition (MLA), where several receive beams are collected for each transmit beam. This thesis includes a contribution regarding how the use of MLA will influence B-mode imaging in the cardiac situation. Not using several receive beams in an aberrated cardiac situation or using MLA in a non-aberrated situation resulted in nice images. But the combination of MLA and aberration caused artifacts. Temporal resolution in speckle tracking would increase greatly if MLA in cardiac B-mode could work. An additional contribution investigates how using MLA influences the regions of origin of data in TDI. A special tool was developed and used to show that with non-optimal setups, the user can get velocity estimates from other locations than intended.

Preface

The present thesis is submitted in partial fulfillment of the requirements for the degree of PhD at the Faculty of Medicine at the Norwegian University of Science and Technology (NTNU). The PhD work was funded by the Research Council of Norway (NFR) in a user-managed project named Intelligent Cardiac Imaging (ICI) with GE Vingmed Ultrasound AS as the external user. The research was carried out at the Department of Circulation and Medical Imaging, NTNU. The main supervisor has been Professor Hans Torp, and co-supervisor has been Associate Professor Asbjørn Støylen, both from the Department of Circulation and Medical Imaging, NTNU.

Acknowledgments

Several people have been involved in work behind this thesis. Sigmund Frigstad has been the GE Vingmed representative concerning the ICI project. He has been of great help with issues ranging from scanner software to discussions concerning which candidate projects to follow. The other GE Vingmed Ultrasound employees in Trondheim have also been helpful. Many thanks to Vidar Lundberg, Kjetil Viggen, Arve Stavø, Jens Lien and Tor Arne Grindal. I have also very much valued the discussions and meetings with the rest of the ICI team including Jøger Hansegård, Bjørn Olstad, Stein-Inge Rabben, Erik Steen, Eva Nilssen and Kjell Kristoffersen.

The Trondheim ultrasound group is well known for a working collaboration between technology and medicine. In addition to Asbjørn Støylen, my great supervisor in medicine related issues, I have also very much appreciated discussions and collaboration with the following clinicians: Charlotte Bjørk-Ingul, Brage Amundsen, Siri Malm, Einar Sagberg and Stig Slørdahl. My fellow PhD students have made the daily work rewarding by creating a very positive and encouraging atmosphere in the corridors as well as being valuable discussion partners concerning technical issues. I would especially want to thank Jonas Crosby, Lasse Løvstakken, Torbjørn Hergum and Svein-Erik Måsøy. The last years of my PhD work I shared office with fellow PhD student Tore Grüner Bjåstad. Thank you very much for your humor, insight and good collaboration Tore!

A good wife is the best support a man can have. Thank you for love and patience Mette Marie.

Finally, thank you very much Hans for your patience in guiding my journey through the fields of ultrasound.

Table of Contents

Chapter 1

Introduction

Svein Arne Aase
Dept. Circulation and Medical Imaging, NTNU

Echocardiography is an important method in the diagnosis and monitoring of cardiac patients. Both coronary artery disease (CAD), valve diseases and synchronization issues of the left ventricle can be investigated by this method.

To date the most common echocardiographic tools for assessing left ventricular health is visual assessment of B-mode images. Although widely used and much appreciated, visual methods have inherent weaknesses such as dependency on training and experience and limitations in the way findings may be reported and communicated. With increasingly mature technology, several quantitative methods have been suggested. These methods include simple geometry measurements and thereby volume calculations, attempts at tissue characterization, various approaches for measuring synchronicity and methods for assessing global and local deformation.

For assessing CAD robust quantitative measures of global and local deformation is highly wanted. Several ultrasound technologies for estimating parameters such as velocity, displacement, strain rate and strain have been introduced [1, 2, 3, 4, 5]. Such technologies have also been used for measuring synchronicity [6, 7, 8].

From a technical viewpoint, the most popular technologies for myocardial deformation quantification can be coarsely divided into two approaches, although more or less overlapping approaches also exist. The first approach is referred to as tissue Doppler imaging (TDI), color Doppler myocardial imaging or tissue velocity imaging [1, 9]. The TDI approaches are characterized by the use of autocorrelation to estimate phase shifts on data recorded in a separate acquisition than the B-mode images. The basic data produced by this approach is velocities. In the most promising CAD related use of TDI, strain and strain rate are calculated from the velocity data [3].

The other group of approaches use the B-mode images. The technology in use for actually measuring displacement is typically some sort of speckle tracking or feature tracking [2, 5, 8]. Using several displacement measurements, other deformation parameters can be calculated. While such methods promise several advantages compared to TDI, some of the challenges remain. Two of the major challenges for quantitative myocardial analysis are the quality of the estimated parameters and the efficiency at which such parameters can be extracted from recordings.

For myocardial deformation parameters to be accurate, high temporal resolution is preferable, especially in the phases of the cardiac cycle where the largest accelerations occur [10]. Aortic Valve Closure (AVC) occurs in such a phase, and the timing of AVC is important to separate the ejection and diastolic phases of the cardiac cycle. Doing timing of AVC as well as integrating all the aspects of an myocardial deformation analysis system is therefore a challenge for quantitative myocardial analysis.

In the present thesis, contributions to the challenges of efficiency, quality and high frame rate are made by introducing an automated myocardial deformation analysis system with integrated automatic AVC detection. Special attention is made to AVC detection, and both automatic detection algorithms and various candidates for AVC are tested and evaluated.

To obtain high temporal resolution, frame rate increasing techniques such as multi line acquisition (MLA) have been tried in TDI. The use of MLA introduces some uncertainty concerning where velocity estimates originate from. If techniques similar to MLA could be used in B-mode imaging, the frame rate of B-mode images could be increased greatly. The temporal resolution of speckle tracking would then also be increased accordingly.

The present thesis includes a contribution where a more true region of origin for TDI based data is visualized. Also included is a paper regarding the use of MLA in cardiac B-mode imaging.

1.1 Tissue Doppler imaging and speckle tracking

1.1.1 Tissue Doppler imaging acquisition

Standard TDI acquisition is, like Color Flow imaging [11] acquisition, based on pulsed wave packet acquisition [1]. A complete TDI two-dimensional (2-D) data frame is made by scanning an ultrasound sector beam by beam and transmitting several pulses in each direction. The received backscattered signals are sampled at time delays after transmission representing the depths of the TDI cells in the sampling grid of the sector. The sampling grid is defined by the number of ranges along each beam and the number of beams used to cover the sector.

Each cell will then contain a packet with a number of signal samples, a packet size, corresponding to the number of pulses sent in each direction. The signal samples at the cell have all been sampled at the same time delay after transmission of the consecutive pulses.

With TDI, autocorrelation has typically been used to estimate phase shifts and thus calculate velocities. To do so, a packet size of at least two signal samples is needed. Together, the sampling grid with the packet in each cell, constitute one frame.

The rate at which pulses in one direction are sent is the pulse repetition frequency (PRF). This will also equal the sample rate of the packet signal. There are two ambiguities related to the PRF, the range ambiguity related to using high PRFs compared to the depth of the ultrasound scan and the aliasing ambiguity related to observing high velocities compared to the PRF.

In order to be able to estimate without ambiguity at which depth received signals originate, new signals in a single direction can not be sent before the old signals have returned from the maximum depth. This is shown in Eq 1.1

$$PRF_{Max} = c/(2 * depth) \tag{1.1}$$

where c is the speed of sound in tissue. Exceeding this PRF would introduce ambiguity concerning the origin of the received signals.

By the Nyquist theorem, aliasing will generally occur if the signal variation frequency exceeds half the sampling rate. In TDI, this means that the maximum observerable velocity, the Nyquist velocity, will be limited by the PRF. If velocities exceeding this threshold are present, they will wrap the velocity range. If a positive velocity slightly higher than the positive Nyquist velocity is present, it will be represented as a large negative velocity value. Assuming that the maximum velocities are known, e.g. 0.16 m/s for typical myocardial motion, a corresponding PRF can then be calculated by equation 1.2

$$PRF = v4f_0/c = 0.16m/s \times 4 \times 2.5MHz/1540m/s \approx 1000Hz \tag{1.2}$$

where v is the Nyquist velocity, f_0 is the center frequency, and c is the speed of sound in tissue. If velocities beyond the Nyquist velocity, as given by the PRF, are present in the ultrasound sector, aliasing will occur. If a higher PRF than necessary is used, each velocity estimate will be calculated using a shorter observation time than it could have had and will thus be less robust.

The frame rate (FR) is the rate at which frames are recorded. This will determine the temporal resolution of all calculated deformation parameters. The time between each temporal sample will be $\Delta_t = 1/FR$. High frame rate is necessary for discerning short lived cardiac events [10].

With low PRF requirements, the time between subsequent pulses in the same direction is relatively long compared to the time used for one pulse to reach the bottom of the sector and be reflected back to the probe. The latter is given by $1/PRF_{max}$ and will with approximately 15 cm depth of sector be approximately 0.2 ms. The time between pulses will in the described case be $1/PRF = 1/1000Hz = 1ms$. A simple implementation of this is shown in the left panel of Fig 1.1 where the width of the bars correspond to the time used for each signal of a packet. Beam interleaving is a technique for using the time between subsequent signals in a packet to send pulses in other directions [12]. This is illustrated in the right part of Fig 1.1. The technique makes packet acquisition with low PRF more efficient and thus frame rate is increased.

Given a certain PRF, a certain beam interleaving scheme and a certain ultrasound sector, the frame rate and the number of beams are directly related. By reducing the number of beams, the frame rate will increase and vice-versa. Fewer beams means coarser lateral sampling of the ultrasound sector and, this will reduce the quality of the data in discerning local deformations. A simple approach for reducing the number of beams without reducing the lateral sampling resolution is to reduce the width and depth of the ultrasound sector.

More complicated approaches for increasing frame rate also exist. One is the use of multi line acquisition (MLA) [13, 14]. Normal acquisition progresses by first focusing

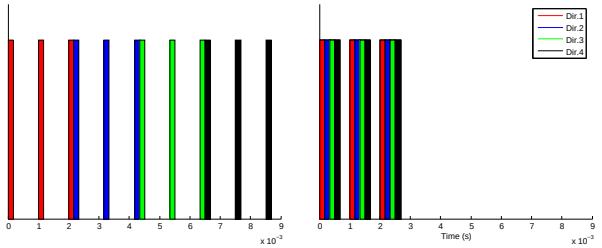

Figure 1.1: Packet acquisition with four directions with and without beam interleaving. Left: In normal packet acquisition the packet of one direction is sent and received before the packet of the next direction. Right: With beam interleaving, pulses in other directions are sent and received before the next pulse of the first direction is sent and received.

a transmit beam to insonate part of the ultrasound scanning sector. Then a receive beam is focused at the same area as the transmit beam. This is illustrated in the left part of Fig 1.2. With MLA, several receive beams are focused in parallel within the area covered by a single transmit beam (right part of Fig. 1.2). Using MLA, the number of receive beams can thus be larger than the number of transmit beams. As the receive beams are formed in parallel, MLA acquisition is faster than regular acquisition with the same number of transmit beams. This increases frame rate. The increased frame rate is however achieved at the cost of sensitivity and resolution. To use broader transmit beams, a smaller part of the probe aperture is used on transmit, and the signal-to-noise ratio (SNR) as well as resolution are thus reduced. Apodization techniques on transmit and receive can be used to generate broader beams while still using a larger part of the probe aperture [15]. Additionally to these limitations, artifacts related to MLA and aberration may appear [16].

When recording TDI, B-mode is typically also recorded. The B-mode and TDI frames can be recorded interweaved with a separate acquisition for each mode. The primary reason why a separate acquisition is preferable is the PRF and frame rate requirements. As discussed above, a PRF at approx 1000 Hz is needed to measure unaliased cardiac velocities. Normal B-mode is acquired without packet acquisition (packet size is 1). The PRF for data cells at the same position in the ultrasound sector would then equal the frame rate. As typical B-mode frame rates are well below 100 Hz, such an acquisition would cause aliasing if used for TDI processing. In the simplest implementation, an interweaved acquisition of B-mode and TDI frames would have equal frame rate in both the B-mode data set and the TDI data set. But as high temporal resolution typically has been prioritized in TDI, a technique for splitting B-mode scan in sub scans is needed to have higher TDI frame rate than B-mode frame rate [17]. In addition, the TDI sampling grid is typically much coarser than a standard B-mode sampling grid and this also improves frame rate.

With a separate acquisition for TDI, it is also possible to have a different pulse length in TDI than in B-mode. Some of the SNR lost by using broader transmit

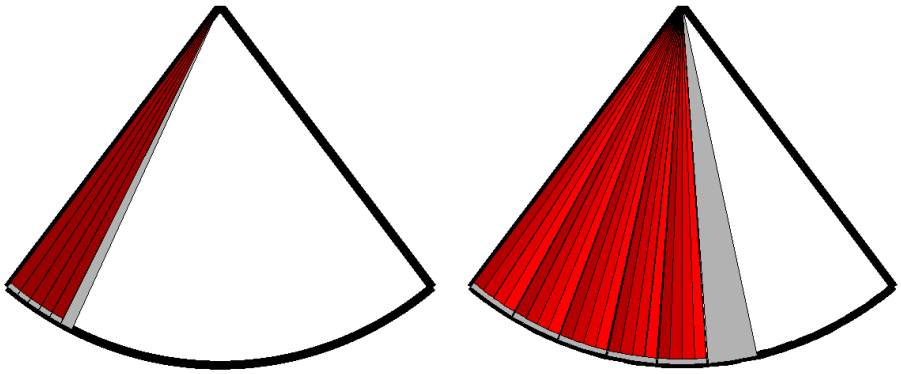

Figure 1.2: MLA acquisition, snapshot during scanning of a single frame. The sixth transmit beam has just been sent. Left: In normal acquisition transmit and receive beams are of equal size and cover approximately the same area. Right: With MLA, several (here four) parallel receive beams are located inside each transmit beam. Thus a larger percentage of the sector is scanned during the same time as used in normal acquisition.

beams with MLA can then be gained by using longer pulses as the bandwidth will be narrower. But this is achieved at the expense of axial resolution. With better axial resolution, more averaging can be applied.

1.1.2 Tissue Doppler imaging processing

The recorded signal of each TDI packet is an ultrasound radio frequency (RF) signal. Before further TDI processing is done and phase shifts are estimated, a complex base-band modulation technique, known as IQ-demodulation [18], is applied to the packet signals. The result of this operation is a complex packet signal vector for each cell in the sampling grid.

The further processing from IQ signals to velocities is based on estimating the autocorrelation function. Autocorrelation can be estimated for the complex IQ signal $z(k)$ as (from [19])

$$\hat{R}_N(m) = \frac{1}{N} \sum_{k=1}^{N-m} z(k+m) z(k)^* \tag{1.3}$$

where m is lag and N is the packet size. Larger numbers of N than two would give more robust estimates.

To estimate the mean frequency of the signal, the autocorrelation estimator with lag $m = 1$, $\hat{R}_N(1)$ can be used as

$$\omega = phase(\hat{R}_N(1)) = \arctan_2(Im(\hat{R}_N(1)), Re(\hat{R}_N(1))) \tag{1.4}$$

where $arctan_2$ is the four quadrant inverse tangent function.

From the angular mean frequency ω the mean axial velocity v can be calculated by using a scaling factor as

$$v = \frac{cPRF}{2\omega_0}\omega \tag{1.5}$$

where c is the speed of sound in tissue, PRF is the pulse repetition frequency and ω_0 is the received angular mean frequency.

The velocity estimates can be considerably improved by using spatial averaging. Such averaging should be applied to autocorrelation estimates, not velocities, to get maximum variance reduction [20].

To get strain rate from velocities, the velocity gradient or the difference in velocities at two neighboring locations are used as

$$strainrate = \frac{v_2 - v_1}{L} \tag{1.6}$$

where v_1 and v_2 are velocities from two neighboring locations and L is the distance between these locations. To get strain, the strain rate data must be integrated over time. This will result in Eulerian (natural) strain (S_N). To get Lagrangian strain (S) a correction factor must be used, $S = e^{S_N} - 1$. [9]

1.1.3 Is Tissue Doppler Imaging a Doppler method?

Velocities in TDI are calculated from phase shifts estimated by an autocorrelation method. The acquisition is pulsed, not continuous. This raises the issue whether the TDI method deserves to have "Doppler" in its name or not. A possible definition of the Doppler effect is "any phenomenon for which a change occurs in the spectral content due to a relative motion of the source and target and from which the relative velocity can be estimated" [18]. This definition would not cover TDI, as velocities in TDI are not estimated from the spectral content of one received pulse, but instead by using an autocorrelation method on several pulses. The argument that pulsed methods for velocity estimation are not using the Doppler effect by strict definitions has been elaborated by Jensen [21]. Gill, however, defines the Doppler effect as "the change in apparent time interval between two events, which arises from the motion of an observer, together with the finite velocity of transmission of information about the events" [22]. Such a definition would include pulsed methods such as TDI.

Either way, the methods used for estimating velocity in TDI at least have strong similarities with "Doppler methods", even though the Doppler effect as defined by the strictest definition above is not used. However, to be compatible with prior published work from this institution, the pulsed wave color overlaid tissue velocity imaging method described and used in this thesis will be referred to as tissue Doppler imaging (TDI).

1.1.4 Acquisition for speckle tracking

Standard speckle tracking approaches use gray-scale B-mode data from normal B-mode acquisition, but some optimization of the acquisition for speckle tracking purposes can improve results.

Normal cardiac B-mode acquisition for real-time human eye assessment does not need a frame rate of more than 30 frames pr second but, when doing quantitative analysis, the temporal resolution of the processed deformation parameters/curves will correspond to the frame rate of acquisition. Therefore a higher frame rate might be preferable. Additionally, given the same image quality, speckle tracking will be more accurate with higher frame rates as there will be less motion from frame to frame. If the frame rate is too low compared to the velocities of the tissue, decorrelation from frame to frame might occur, and thereby the quality of tracking is reduced. Too high frame rate might also be a challenge, as the speckle tracking algorithm in such situations might estimate that no displacement has occurred from one frame to the next. If not handled correctly, a corresponding velocity by differentiation would then be zero. Frame rate increasing techniques such as MLA must be used with caution as they can remove the shift invariance property of the system [16].

1.1.5 Speckle tracking: algorithms and processing

Ultrasound images have a distinct look when compared to other imaging modalities. One of the characteristics of the ultrasound images is the intensity variations visible at locations where complex targets like tissue are present. Such patterns are known as speckles. Speckles arise when there are a large number of randomly spaced scatterers within cells of the ultrasound sampling grid. When scatterers within a cell are insonified, there will be a variance in the intensity and phase reflected by each scatterer. If the interference effect reflected to the transducer from this cell is mostly constructive, the cell will have a bright value. If the interference effect is mostly destructive, the cell will have a dark value. As this effect will vary from cell to cell, intensity variations will appear in the resulting image.

The concept of speckle tracking, also known as block matching, is illustrated in Fig 1.3. At time point t0, a region of interest (ROI) is defined somewhere in the myocardium. In the following frame, t1, a search area is placed around the location of the ROI. Then a matching algorithm is employed inside this search area to find the best match at t1 corresponding to the ROI at t0. The result will be a directional vector representing the motion of the ROI from time t0 to time t1. By repeating this for every frame, the total movement of the ROI can be estimated.

The first speckle tracking approaches for estimating soft tissue motion from ultrasound B-mode images were based on using the correlation coefficients for calculating the best match [23]. This is a rather computation intensive method. Later, Bohs and Trahey [5] showed that the sum of absolute differences (SAD) algorithm (Eq. 1.7) was equally good and much faster to implement. The equation gives the non normalized absolute error, ϵ, between regions in two images (frames) X and Y by

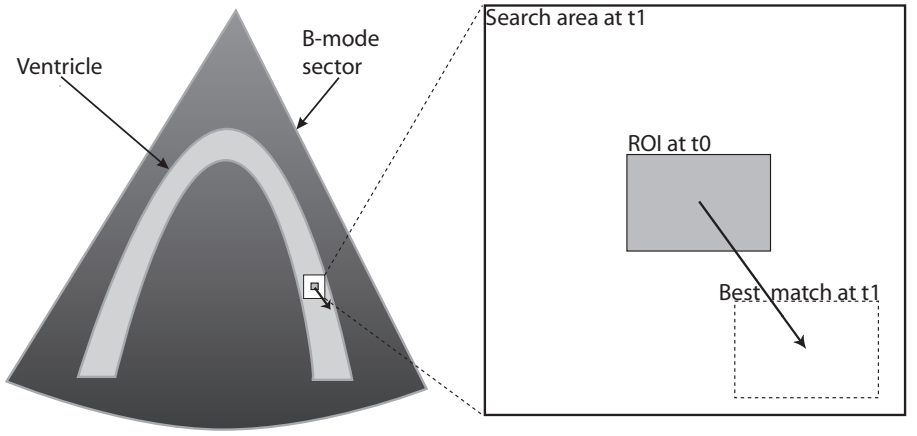

Figure 1.3: Speckle tracking illustration. An ROI at one frame (t0) is searched for in a search area in another frame (t1). The best match provides a directional vector.

(from [24])

$$\epsilon_{m,n} = \sum_{i=1}^{l} \sum_{j=1}^{k} |X_{i,j} - Y_{i+m,j+n}| \tag{1.7}$$

where $l \cdot k$ is the size of the ROI while (m, n) are coordinates within the search area in Y. By performing this calculation over the entire search area in Y, a minimum $\epsilon_{m,n}$ can be found, and (m, n) will then give the coordinates for the best match [5]. In modern CPUs, the SAD algorithm is even implemented as part of the multimedia instruction sets and is thus highly optimized for fast execution [25].

Speckle tracking can be done on either detected B-mode data or raw radio-frequency (RF) data. By using RF data, improved resolution of tracking along the beams can be achieved at the cost of denser sampling and thus longer processing time [5, 26]. For large strains, better results might be achieved using detected signals than using RF signals [27]. RF tracking was initially a 1D method, but has recently been extended to 2-D and validated [28].

Fig 1.3 illustrates speckle tracking on scan converted data. This means that the ultrasound data has been geomtrically positioned in the scan grid before the speckle tracking algorithm is employed. It is also possible to do speckle tracking on the beam space data available before scan conversion.

Important parameters when using a speckle tracking algorithm on a specific dataset are the ROI size (often denoted as kernel in speckle tracking literature) and the search area size. With larger ROIs, a more distinct speckle pattern is achieved, and thus it will be more noise resistant, but the spatial resolution of the resulting tracking will be reduced [26]. By using larger search areas, higher velocities (larger displacements from frame to frame) can be detected, but this will require more calculations than smaller search areas. The robustness of the tracking will also be reduced with large

search areas as the probability of finding false matches increases.

The point-spread-function (PSF) of an ultrasound system represents the ultrasound response (image) when imaging a single point. A PSF will have a certain extent laterally and axially in the ultrasound image. To do effective tracking, the ROI should at least cover two PSFs in each direction.

The resolution of a speckle tracking algorithm as described above is limited by the grid resolution in the scan grid. This means that motion less than one cell can not be detected. To achieve sub-cell resolution in speckle tracking, several interpolation algorithms have been suggested [29]. The interpolation can be done on the B-mode data before tracking is started or on the SAD function or the correlation function. Some kind of interpolation is essential to avoid the discretization error introduced by the sampling of the scan grid. This is especially important when tracking objects over several frames, as the error accumulates.

The output of a speckle tracking algorithm is the frame to frame displacement of each of the points tracked by the algorithm. By accumulating such displacements over a cardiac cycle, the total displacement of each tracked point is found. By using this information together with the frame rate, the velocities of each tracked point can be calculated. Combining displacements with the distances between points, strain and strain rate can also be calculated. To get more robust data, the displacement of several tracked points can be averaged or regularized in various ways before velocities, strain and strain rate are calculated [30]. This will also reduce discretization errors. Thus, the actual velocity, strain and strain rate curves achieved will depend heavily on the specific implementation used for calculating these parameters.

The displacement output from a speckle tracking algorithm can be used to calculate Lagrangian strain using equation 1.8,

$$strain = (L - L_0)/L_0 \tag{1.8}$$

where L is the length at the latest point in time and L_0 is the length at the first point in time. To do this tracking of at least two points is needed. The points can be positioned, depending on the ultrasound view used, to calculate longitudinal, radial or circumferential strain. When calculating longitudinal strain L_0 would typically represent the distance along the myocardium between the two points at end-diastole. L would the be the distance along the myocardium between the two points at some later frame in the cardiac cycle. The resulting strain is the relative change in length of the segment since end-diastole.

Strain rate from Tissue Doppler is normally given as Eulerian strain rate. To get Eulerian (normal) strain rate from Lagrangian strain, the temporal derivative of strain is taken and the values are multiplied with a correction factor $1/(1 + strain)$.

1.1.6 Tissue Doppler imaging vs. speckle tracking

Tissue Doppler imaging possibilities on commercial ultrasound machines appeared nearly 15 years ago. The advantage of TDI over speckle tracking at that time was that TDI could run in real time. Additionally, the B-mode quality was poorer as fundamental B-mode imaging was used. Today, the second harmonic B-mode quality is sufficient for tracking and speckle tracking can be done in near real time. Strain and strain rate analysis has so far usually been done as post processing and real time performance is therefore not essential. However, for Tissue Synchronization Imaging (TSI) real time velocity information is useful [6, 7].

The acquisition used for speckle tracking purposes, is the same as used for the standard B-mode images. By looking at the quality of the B-mode image, the experienced user can immediately be able to predict the quality of the resulting tracking. This is not the situation for TDI. As TDI data are recorded in a separate acquisition, the relation between the visible B-mode quality and the TDI data is much weaker.

The dynamical range when imaging tissue is large. This means that if a part of the myocardium with weak intensities is investigated by TDI, neighboring structures with strong intensities may influence the measured velocities [31].

The native deformation parameter produced by TDI is velocities while the corresponding native deformation parameter produced by speckle tracking is displacement. Strain rate relates directly to velocities while strain relates directly to displacement. Displacement and strain parameters are inherently more robust when calculated from speckle tracking than TDI since displacement and strain from TDI involves integration, and thus accumulation of measurement errors over time.

Speckle tracking is based on displacement calculations from two consecutive frames. As long as the speckle pattern is conserved, the events between the two frames do not influence the result. In TDI, only the velocities present in an area while a packet is recorded are dectected. Events happening in an area between packets are not detected.

In speckle tracking based on RF data and in TDI, the recorded phase information is used for calculations. In speckle tracking on detected B-mode data the phase information is not used. The 2-D nature of speckle tracking can be used to provide a 2-D deformation vector while TDI can only be used to provide a 1-D deformation vector. A limitation of speckle tracking methods is that the temporal resolution is limited by the B-mode frame rate.

For instantaneous imaging of velocities and strain rate, TDI is well suited. A single velocity/strain rate image by TDI is recorded over only 2-3 ms. Producing a single velocity/strain rate image by speckle tracking would at least involve two B-mode frames and doing differentiation. Additionally, TDI may be used to measure very high velocities as long as the PRF can be increased. In speckle tracking, too high velocities with respect to the B-mode frame rate used would cause decorrelation of the speckle pattern. Because TDI is recorded as an independent acquisition mode from B-mode, TDI acquisition settings such as frame rate, PRF and pulse length may be modified according to the intended use of the data.

In summary, for some types of quantitative analysis of the myocardium TDI is still

the best choice. One such type of analysis is real-time 1-D strain rate or velocities at high temporal resolution. An example of this kind of analysis is synchronization imaging. When strain or displacement is needed or 2-D measurements are important, speckle tracking is a better option.

1.2 Aims of study

The overall aim of this work is to increase quality and efficiency of quantitative echocardiographic methods. To be able to assess the health of left ventricular tissue, both with respect to CAD and synchronicity, tissue deformation parameters are of special interest. Tissue deformation analysis systems can be implemented in many different ways. For research purposes, a system supporting several different combinations of data and algorithms while still being efficient to use is interesting. An important part of such a system is automatic AVC detection, as deciding this time point is time-consuming and the event must be decided before parameters close to AVC can be determined. The first aim of study would therefore regard a fast and flexible tissue deformation analysis system with automatic AVC detection.

Good temporal resolution is preferable in myocardial deformation analysis, especially when considering the phases of the cardiac cycle with highest accelerations. To get good temporal resolution, frame rate increasing techniques such as MLA has been tried in TDI. But the effect MLA has on the quality of the estimates is largely unknown. If MLA techniques could be used in regular B-mode, the B-mode frame rate would increase and hence also the temporal resolution of speckle tracking. The second aim is therefore to investigate the influence of MLA in B-mode and TDI.

The formalized aims thus become:

Aim 1: Address possibilities of a fast and flexible tissue deformation analysis system analysis with automatic AVC detection.

Aim 2: Address the possibilities for using MLA in regular cardiac B-mode and the effects of using MLA in TDI.

1.3 Summary of presented work

In this section, a summary of the original contributions of the present thesis is presented. An overview of the contributions is shown in Table 1.1. The individual contributions of this author are highlighted in cases of joint work.

Contribution no. 1: (chapter 2)
Automated strain and strain rate
Charlotte Bjork-Ingul and Svein A. Aase

Table 1.1: Original contributions

#	Chapter	Contribution title	Challenge	Publication status
1	2	Automated strain and strain rate	Efficiency	Published Sep 2007
2	3	Automatic Timing of Aortic Valve Closure in Apical Tissue Doppler Images	Efficiency, Quality	Published Jan 2006
3	4	Aortic Valve Closure: relation to tissue velocities by Doppler and speckle tracking in normal subjects	Quality	Accepted for publication 2008
4	5	Velocity Sensitivity Mapping in Tissue Doppler Images	Quality	Published Sep 2005
5	6	The Impact of Aberration on High Frame Rate Cardiac B-Mode Imaging	Quality	Published Jan 2007

Dept. Circulation and Medical Imaging, NTNU

This text concerns systems for automated strain and strain rate analysis. Such systems are important for clinical research in strain and strain rate and might in some form eventually be used in clinical practice.

A flexible automated myocardial deformation analysis system made by the Trondheim ultrasound group is described. Its features include detection of the myocardium, segment border definition, support for both TDI , speckle tracking or a combination of both for tracking of segment borders, several algorithms for calculating strain and strain rate, automatic timing of AVC and parameter detection on resulting strain and strain rate curves.

Such a system is a contribution to the efficiency challenge of quantitative myocardial analysis as it makes the analysis of strain and strain rate progress more quickly while still enabling good quality of the results.

The text also includes an overview of clinical use of automated strain and strain rate analysis methods and discusses some future directions of such systems.

Specific contribution of this author (as this is a joint work): The author contributed to the implementation of the first version of the system, and did support, tuning and updates in further versions up to date. The article was written jointly 50%/50% with clinician Charlotte Björk-Ingul. The technical sections, including "Future automated analysis systems" were mainly written by this author while the clinical sections were mainly written by the clinical author. The remaining sections were co-written. The AutoStrain software has been programmed by the following persons: Prof. Hans Torp,

students Sigrid Berg and Anna Leivestad, and Ph.D. students Svein A. Aase and Jonas Crosby.

This text was published as chapter 24 in Marwick TH, Yu C-M, Sun PS, eds. Myocardial Imaging - Tissue Doppler and Speckle Tracking: Blackwell Publishing 2007:278-87.

Contribution no. 2: (chapter 3)
Automatic Timing of Aortic Valve Closure in Apical Tissue Doppler Images
Svein Arne Aase[1], Asbjørn Stoylen[1,2], Charlotte Bjork Ingul[1], Sigmund Frigstad[3] and Hans Torp[1]
[1] Dept. Circulation and Medical Imaging, NTNU
[2] Dept. Cardiology, St. Olav Hospital, Trondheim, Norway
[3] GE Vingmed Ultrasound, Horten, Norway

In this paper, methods for automatic timing of AVC in apical tissue Doppler images are suggested and tested. This has special interest when analyzing strain and strain rate data and extracting parameters from various parts of the cardiac cycle. To be able to partition the cardiac cycles in its phases, an accurate measure of AVC must be achieved. With automatic timing a contribution to the efficiency challenge of analyzing TDI data is made. Additionally, AVC is extracted from the same cardiac cycle as used in analysis. Compared to alternative approaches this would also constitute a contribution to the accuracy of AVC and thus also the strain and strain rate parameters occurring near AVC.

The event in velocity/time curves used for AVC detection was the peak positive acceleration after ejection and before the E-wave. To get robust estimates for this event, mitral ring (atrioventricular plane) movement, the opening of the mitral valve and the time point of early relaxation were first estimated. Both automated and automatic approaches are described in the article. For the automatic approaches the positions and motion of the mitral ring are detected automatically, otherwise the mitral ring is located manually and tracking is used to detect the motion. The performance of the automatic AVC detection methods was evaluated with phonocardiogram of the second heart sound. The best automatic method estimated AVC within 25 ms of the reference in 98% of the cardiac cycles.

This paper was published in Ultrasound in Medicine and Biology 2006;32(1):19-27.

Contribution no. 3: (chapter 4)
Aortic Valve Closure: relation to tissue velocities by Doppler and speckle tracking in normal subjects
Svein Arne Aase[1], Asbjørn Stoylen[1,2], and Hans Torp[1]
[1] Dept. Circulation and Medical Imaging, NTNU
[2] Dept. Cardiology, St. Olav Hospital, Trondheim, Norway

This paper is an evaluation of different methods for AVC timing in velocity data, concerning whether they produce the correct result or not compared to high frame rate B-mode images of the aortic valve. It is shown that the the initial negative velocity after ejection, widely reported as a marker of AVC, actually positions AVC approximately 20 ms too early. Better candidates compared to the B-mode reference were the peak positive acceleration after the initial negative velocity after ejection and the zero crossing after the initial negative velocity after ejection. As such, the article is a contribution to the improved accuracy and correctness of parameters estimated by TDI methods. The article also introduces AVC timing on speckle tracking data and discusses the relation of these results to TDI color M-mode and the pulsed wave tissue Doppler spectrum.

This paper is accepted for publication in European Journal of Echocardiography.

Contribution no. 4: (chapter 5)
Velocity Sensitivity Mapping in Tissue Doppler Images
T. Bjåstad and S. A. Aase, and H. Torp
Dept. Circulation and Medical Imaging, NTNU

This paper addresses the issue of the invisible image quality of TDI recordings. When using TDI velocities (and extracted parameters such as strain and strain rate) the user has selected an area in the image to extract data from. But the real area of origin might be different from the selected area due to the imaging system and the object being imaged. By using simulated pulse echo responses and regarding the B-mode image as a model for the imaged object, this work suggests a method to visualize a more real area of origin for TDI data. As such, this work is a contribution to the quality of TDI measurements.

Specific contribution of this author (as this is a joint work): This work is a joint work 50%/50% with fellow PhD student Tore Bjåstad. The original issue and problem setting was of interest for this author. Tore Bjåstad was brought into the project to contribute with simulation expertise. The project was completed as a joint work and the text was co-written 50%/50%.

This paper was published in the proceedings of the IEEE Ultrasonics Symposium 2005:4:1968-1971.

Contribution no. 5: (chapter 6)
The Impact of Aberration on High Frame Rate Cardiac B-Mode Imaging
T. Bjåstad and S. A. Aase, and H. Torp
Dept. Circulation and Medical Imaging, NTNU

This paper concerns the multiple line acquisition, MLA, technique typically used in TDI to increase frame rate. To better understand the influence of MLA on image

quality, the effect MLA of on B-mode images in situations similar to cardiac imaging is investigated. The main finding was that MLA in combination with aberration as typically present in cardiac imaging will degrade the image quality by the introduction of block artifacts which are not easily compensated for. Not using MLA will not introduce such artifacts while imaging with MLA in a case without aberration will only introduce artifacts that can easily be compensated for. By simulations, the main effects causing these artifacts were found to be skewing and warping of the beams. Warping describes the phenomenon that the direction of the two-way beam differs from the receive direction. Skewing describes the phenomenon that neighboring beam profiles vary in shape and are asymmetrical.

Specific contribution of this author (as this is a joint work): This work is a joint work 50%/50% with fellow PhD student Tore Bjåstad. Tore Bjåstad had the simulation part of the work as his main responsibility while this author had scanner modifications and recording analysis as the main area of responsibility. The text was co-written 50%/50%.

This paper was published in the IEEE Transactions on Ultrasonics, Ferroelectrics, and Frequency Control 2007;54(1):32-41.

1.4 General discussion

The present thesis is a contribution to the ongoing research in improving quantitative methods for myocardial analysis. This field is more active than ever with new methods appearing and an enormous volume of clinical work being done in testing the methods on various clinical cases. In the present thesis contributions to the improvement of both efficiency and quality of quantitative methods for myocardial analysis are introduced. All contributions are related to the issue of high frame rate.

With high frame rate, strain and strain rate analysis with high temporal resolution becomes possible. The suggested automated myocardial deformation analysis system (AutoStrain) enables such analysis to be done in relatively short time (chapter 2). This software has been used as a research tool by the clinicians of the Trondheim ultrasound group in several studies [32, 33, 34, 35]. In addition to increased analysis speed and thus efficiency, another important feature of this system is that the clinicians are able to study and control how the resulting curves appear by changing the parameters used in the analysis. Such parameters include the degree of smoothing, the size of ROIs, search areas and strain rate lengths and different strain and strain rate estimation strategies. They are also able to control whether to use TDI alone, speckle tracking alone or a combination of the two modalities. In the combination mode, low frame rate speckle tracking can provide lateral tracking of material points while TDI can provide axial tracking and high temporal resolution curves. The system has had a limited distribution as it was made to be a internal research tool and thus limited efforts was made in usability, stability and portability. Further development of this tool will address these issues and also allow even more flexibility in how speckle tracking and TDI can be combined.

An important part of the AutoStrain automated myocardial deformation analysis system is the automatic AVC detection algorithm. AVC detection is needed to partition the cardiac cycle into the ejection and diastolic phases to extract parameters such as end-systolic strain and peak systolic strain rate. With high temporal resolution strain and strain rate curves, the AVC marker must also be correspondingly accurate. By initial studies of TDI velocity/time curves, the maximum positive acceleration after ejection was found to be a candidate event for representing AVC [36, 37]. Based on these observations the automatic method for AVC detection was suggested. There are many possible approaches for detecting this event. An approach based on first limiting the search area both spatially and temporally was chosen. With this approach other and more easily detected markers in the ventricle and the velocity/time curves are first detected. Based on available clinical knowledge, the search area for AVC can then be set accordingly. The automatic AVC detection algorithm was developed using one data set and was validated against the second heart sound in phonocardiogram recordings in another data set. This work concluded that automatic AVC detection in TDI velocity/time curves was feasible and that the chosen event, as automatically detected, corresponded well to the start of the second heart sound in the phonocardiogram (chapter 3). But phonocardiogram as a reference for AVC was coarse due to noise and filtering issues. With automatic AVC detection in velocity/time curves, velocity, strain and strain rate analysis can be more efficient and also of better quality as the AVC time point originates from the same cardiac cycle as the data to be analyzed.

The time point of maximum positive acceleration after ejection used for detection of AVC in the automatic algorithm was found to correspond well with the start of the second heart sound in phonocardiograms. However, much of TDI literature actually displaying AVC on TDI velocity/time curves place AVC earlier in the cardiac cycle. Motivated by this lack of consensus regarding the exact event in TDI curves representing AVC, the study comparing different AVC candidates in normal subjects was initiated (chapter 4). The goal of this work was to find which AVC candidate in velocity/time curves best corresponded with AVC. This time the reference method was valve closure as visible in narrow sector B-mode images recorded at the same frame rate as TDI. Alternating frames of B-mode and TDI were recorded, and possible sources of errors were thus reduced. The B-mode images were also used for speckle tracking, thus two independent velocity/time curves, one based solely on speckle tracking and one based on TDI, were made for each recording.

Even though the results of this study do not conclude 100% on exactly what event represents AVC, the study shows that the time point of initial negative velocities after ejection, which is a popular candidate for AVC, is faulty. The maximum positive acceleration event used in automatic AVC detection in chapter 3 is a much closer alternative. This result was apparent both from the TDI curves and the speckle tracking curves and this is an additional argument that the result is correct. Investigations of TDI color M-mode and pulsed wave tissue Doppler showed that the same results appear to be valid in those modalities. This has implications for normal physiology as seen by tissue Doppler and speckle tracking. Using a more correct estimate for AVC may also increase the quality of parameters such end-systolic strain and peak-systolic strain rate. The study also shows that AVC detection by all the

candidate events can be done both in TDI and in high frame rate B-mode based speckle tracking.

The segment of the velocity/time curves between candidate A and candidate C of chapter 4 will eventually disappear as frame rate drops. This might make AVC detection troublesome. However, in such a situation, the temporal accuracy of all other parameters will also have been reduced, and accurate AVC detection is therefore not essential.

Velocity/time curves from pathological ventricles are expected to differ somewhat from the normal curves. Work on establishing the performance of the AVC candidates in such ventricles is in progress. Initial results on an example case with inferior infarction are included in Appendix A. While the velocity/time curve in this example is different from the normal curves, the main features of the curves are still present and all candidates can still be detected. In this example it also seems likely that the conclusions from the normal curves regarding which candidates represent AVC still are valid.

Further work on the subject of AVC detection could include:

- Testing which candidate corresponds best to the B-mode reference and is convenient to use in pathological curves and in stress echocardiography
- Investigating the errors introduced in peak-systolic strain rate and end-systolic strain estimates by using faulty AVC candidates
- Exploring the relationship between AVC by TDI, minimum strain and minimum ventricle volume
- Exploring the mechanics of how the shape of the velocity/time curve at AVC is created

The work on MLA in combination with aberration (chapter 6) shows that achieving high frame rate with MLA in the cardiac setting introduces unwanted effects. In B-mode images the resulting degradation of image quality is easily visible. The effect on TDI is harder to detect. This is part of the general problem with parametric imaging modalities separate to the main imaging modality used for visual assessment. By using the suggested Velocity Sensitivity Mapping (VSM) approach (chapter 5), a more correct estimate of the origin of velocity data in TDI becomes available based on the pulse echo responses and the B-mode images. To some degree this will reveal the quality of the recording. By using VSM a clinician can interrogate the area he or she is interested in and thus decide whether to trust the resulting curve or not. This could potentially improve the quality of the results.

Typically, strain and strain rate by TDI are calculated by using velocities from an area of some extent. Since each of these velocities again originates from an area, the total area of origin used for strain and strain rate could be rather large. Further work on VSM would include visualizing this area and studying how large areas in various cases might influence strain and strain rate values.

Parallel receive techniques such as MLA are among the most promising techniques for increasing temporal resolution without reducing lateral resolution, reducing sector

width, reducing penetration or using stitching of several heart beats. In cardiac B-mode, increased frame rate would increase the temporal resolution of speckle tracking approaches. So far, widespread use of MLA with more than two parallel receive beams in B-mode has been limited. This is probably due to the block-like artifacts appearing in cardiac B-mode images when MLA is used. The origin of these artifacts has been object of much speculation but no studies on this issue has previously been published. With the article on aberration and MLA (chapter 6), the origin of the artifacts are discussed and explained. The reason why correction techniques successful on phantoms fail in the cardiac setting is explained as a result of the combination of aberration and MLA. Two major effects in generating the artifacts are identified as skewing and warping and, these effects are studied by simulations and beam profiles.

As simple warp correction and gain correction algorithms were shown to be insufficient for getting proper results in cardiac imaging, further work in this area would investigate alternative MLA correction strategies. One approach is including some kind of aberration correction [38], another is methods for compensating and correcting for the misalignment of the transmit and receive beam directions in MLA [39]. If such techniques are successful in cardiac B-mode and handles phase information correctly, they could also be interesting for improving data quality in TDI.

The chapters of the present thesis are contributions to the still ongoing quest of increasing frame rate, efficiency and quality of quantitative echocardiography. During the last years and also the time of this PhD project the interest from the clinicians has been steadily increasing. The distant goal of this field is of course to introduce quantitative echocardiography into daily clinical practice and thereby achieve better quality diagnosis and monitoring than previously possible. While this technology is very useful in some cases already, it seems that it will still have to mature even more before the goal can be achieved.

1.5 Thesis outline

The present thesis is organized as follows. In this chapter, the background of the main ultrasound methods used in the papers has been covered. This background should enable readers unfamiliar with TDI and speckle tracking to understand the main content of the papers. A summary of papers and a general discussion concerning the entire thesis has also been given. In chapters 2-6 the thesis papers are presented. The content of the papers is as originally published except for a few minor corrections. The layout, reference style and the variant of english (British/American) of the papers have been adapted to fit the thesis.

The papers are not appearing in chronological order. Although the paper concerning the automatic AVC detection algorithms was published first, the article concerning the AutoStrain myocardial deformation analysis system has been positioned as the first contribution, presented in chapter 2, to introduce a setting where automatic AVC detection is needed. In chapter 3 the automatic AVC detection algorithms are presented while the study comparing several AVC candidates to a B-mode reference is presented in chapter 4.

The paper on MLA with respect to TDI is presented in chapter 5 while the paper on MLA with respect to B-mode is presented in chapter 6.

1.6 Publication list

Not all publications during the course of the Ph.D. work are included in the thesis. The following is a list of all publications related to the Ph.D. project to which this author has contributed.

Peer reviewed papers

1. Aase, Svein Arne; Støylen, Asbjørn; Ingul, Charlotte Bjørk; Frigstad, Sigmund; Torp, Hans. Automatic timing of aortic valve closure in apical tissue Doppler images. Ultrasound Med Biol 2006;32(1):19-27.

2. Bjåstad, Tore; Aase, Svein Arne; Torp, Hans. The Impact of Aberration on High Frame Rate Cardiac B-Mode Imaging. IEEE Trans Ultrason Ferroelectr Freq Control 2007;54(1):32-41 (50% contribution).

3. Aase, Svein Arne; Støylen, Asbjørn; Torp, Hans. Aortic Valve Closure: relation to tissue velocities by Doppler and speckle tracking in normal subjects. Accepted for publication in Eur J Echocardiogr.

Book Chapter

4. Bjork-Ingul, Charlotte; Aase, Svein A. Automated strain and strain rate. In: Marwick TH, Yu C-M, Sun PS, eds. Myocardial Imaging - Tissue Doppler and Speckle Tracking: Blackwell Publishing 2007:278-87 (50% contribution).

Patent

5. Aase, Svein Arne; Frigstad, Sigmund; Torp, Hans. Method and apparatus for detecting cardiac events. U.S. Patent Application 20060058673, 2006.

Conference proceeding papers

6. Aase, Svein Arne; Støylen, Asbjørn; Ingul, Charlotte Bjørk; Frigstad, Sigmund; Torp, Hans. Automated Detection of Aortic Valve Closure in Apical Tissue Doppler Images. Proc IEEE Ultrason Symp 2004:3:2061-2064.

7. Bjåstad, Tore; Aase, Svein Arne; Torp, Hans. Velocity Sensitivity Mapping in Tissue Doppler Imaging. Proc IEEE Ultrason Symp 2005:4:1968-1971 (50% contribution).

Abstracts

8. Aase, Svein Arne; Støylen, Asbjørn; Ingul, Charlotte Bjørk; Frigstad, Sigmund; Torp, Hans. Automatic timing of aortic valve closure using tissue Doppler imaging. Eur J Echocardiogr 2005;6(Suppl 1):S93.

9. Aase, Svein Arne; Torp, Hans; Støylen, Asbjørn. Relation between Aortic Valve Closure by high frame rate B-mode and end systolic events in Tissue Doppler velocity/time curves. Eur J Echocardiogr 2006;7(Suppl 1):S5.

10. Aase, Svein Arne; Torp, Hans; Støylen, Asbjørn. The duration of aortic valve closure. Eur J Echocardiogr 2006;7(Suppl 1):S121.

Contributions to the work of others

11. Ingul, Charlotte Bjørk; Torp, Hans; Aase, Svein Arne; Berg, Sigrid; Støylen, Asbjørn; Slørdahl, Stig Arild. Automated analysis of strain rate and strain: Feasibility and clinical implications. J Am Soc Echocardiogr 2005;18:411-418.

12. Brekke, Svein.; Ingul, Charlotte Bjørk.; Aase, Svein Arne; Torp, Hans G.; Increasing frame rate in ultrasound imaging by temporal morphing using tissue Doppler. IEEE Trans Ultrason Ferroelectr Freq Control 2006:53(5):936-946.

13. Støylen, Asbjørn; Malm, Siri; Aase, Svein Arne; Sagberg, Einar. Aortic closure can be timed by tissue Doppler. Eur J Echocardiogr 2004;5(Suppl. 1):S159.

14. Støylen, Asbjørn; Malm, Siri; Sagberg, Einar; Aase, Svein Arne. Initial diastolic deformation occurs before aortic valve closure in mid septum. Eur J Echocardiogr 2004;5(Suppl. 1):S159.

15. Ingul, Charlotte Bjørk; Støylen, Asbjørn; Slørdahl, Stig Arild; Bjørnstad, Knut; Aase, Svein Arne; Torp, Hans; Marwick, Thomas. Automated peak systolic strain rate increases the accuracy of dobutamine stress echocardiography. European Heart Journal 2005;26(Suppl 1):230.

16. Ingul, Charlotte Bjørk; Torp, Hans; Berg, Sigrid; Aase, Svein Arne; Støylen, Asbjørn; Slørdahl, Stig Arild. Automatic measurement of strain rate is timesaving and has comparable accuracy to manual measurement. European Heart Journal 2004:25(Suppl 1):473-474.

References

[1] W. McDicken, G. Sutherland, C. Moran, and L. Gordon, "Colour Doppler velocity imaging of the myocardium," *Ultrasound Med Biol*, vol. 18, pp. 651–654, 1992.

[2] M. Leitman, P. Lysyansky, S. Sidenko, V. Shir, E. Peleg, M. Binenbaum, E. Kaluski, R. Krakover, and Z. Vered, "Two-dimensional strain-a novel software for real-time quantitative echocardiographic assessment of myocardial function," *J Am Soc Echocardiogr*, vol. 17, pp. 1021–9, Oct 2004.

[3] A. Heimdal, A. Stoylen, H. Torp, and T. Skjaerpe, "Real-time strain rate imaging of the left ventricle by ultrasound," *J Am Soc Echocardiogr*, vol. 11, pp. 1013–1019, 1998.

[4] L. A. Brodin, J. van der Linden, and B. Olstad, "Echocardiographic functional images based on tissue velocity information," *Herz*, vol. 23, no. 8, pp. 491–8, 1998.

[5] L. Bohs and G. Trahey, "A novel method for angle independent ultrasonic imaging of blood flow and tissue motion," *IEEE Trans Biomed Eng*, vol. 38, pp. 280–286, 1991.

[6] A. Heimdal, *Method and apparatus for automatically measuring delay of tissue motion and deformation*. U. S. Patent Application 20040254486, 2004.

[7] J. Gorcsan, H. Kanzaki, R. Bazaz, K. Dohi, and D. Schwartzman, "Usefulness of echocardiographic tissue synchronization imaging to predict acute response to cardiac resynchronization therapy," *Am J Cardiol*, vol. 93, pp. 1178–1181, 2004.

[8] M. A. Vannan, G. Pedrizzetti, P. Li, S. Gurudevan, H. Houle, J. Main, J. Jackson, and N. C. Nanda, "Effect of cardiac resynchronization therapy on longitudinal and circumferential left ventricular mechanics by velocity vector imaging: description and initial clinical application of a novel method using high-frame rate B-mode echocardiographic images," *Echocardiography*, vol. 22, pp. 826–30, Nov 2005.

[9] G. R. Sutherland, L. Hatle, P. Claus, J. D'hooge, and B. Bijnens, *Doppler Myocardial Imaging*, vol. 1. Hasselt, Belgium: BSWK, 2006.

[10] B. Lind, J. Nowak, J. Dorph, J. van der Linden, and L. A. Brodin, "Analysis of temporal requirements for myocardial tissue velocity imaging," *Eur J Echocardiogr*, vol. 3, pp. 214–9, Sep 2002.

[11] L. Løvstakken, *Signal processing in diagnostic ultrasound: Algorithms for real-time estimation and visualization of blood flow velocity*, vol. 25, pp. 29–78. [Doctoral thesis]. Trondheim: NTNU, 2007.

[12] R. Chesarek, *Ultrasound imaging system for relatively low-velocity blood flow at relatively high frame rates.* U.S. Patent 4.888.694, 1989.

[13] D. P. Shattuck, M. D. Weinshenker, S. W. Smith, and O. T. von Ramm, "Explososcan: A parallel processing technique for high speed ultrasound imaging with linear phased arrays," *J Acoust Soc Amer*, vol. 75, no. 4, pp. 1273–1282, 1984.

[14] O. T. von Ramm, S. W. Smith, and H. G. Pavy, "High-speed ultrasound volumetric imaging system – part II: Parallel processing and image display," *IEEE Trans Ultrason Ferroelectr Freq Control*, vol. 38, pp. 109–115, March 1991.

[15] D. A. Guenther and W. F. Walker, "Optimal apodization design for medical ultrasound using constrained least squares part I: theory," *IEEE Trans Ultrason Ferroelectr Freq Control*, vol. 54, pp. 332–42, Feb 2007.

[16] T. Bjastad, S. A. Aase, and H. Torp, "The impact of aberration on high frame rate cardiac B-mode imaging," *IEEE Trans Ultrason Ferroelectr Freq Control*, vol. 54, pp. 32–41, Jan 2007.

[17] J. Kirkhorn, S. Bjærum, B. Olstad, K. Kristoffersen, and H. Torp, "A new technique for improved spatial resolution in high frame rate color Doppler imaging," *Proc IEEE Ultrason Symp*, pp. 1947–1950, 2003.

[18] R. Cobbold, *Pulsed Methods for Flow Velocity Estimation and Imaging.* Oxford University Press, 2007.

[19] H. Torp, "Estimation of blood velocities from Doppler signals," in *Ultrasound Imaging - Waves, Signals, and Signal Processing* (B. Angelsen, ed.), vol. II, pp. 10.1–10.46, Emantec AS, 2000.

[20] H. Torp, K. Kristoffersen, and B. Angelsen, "On the joint probability density function for the autocorrelation estimates in ultrasound color flow imaging," *IEEE Trans Ultrason Ferroelectr Freq Control*, vol. 42, pp. 899–906, 1995.

[21] J. A. Jensen, *Estimation of Blood velocities using ultrasound.* Cambridge: Cambridge University Press, 1996.

[22] T. Gill, *The Doppler Effect: An Introduction to the Theory of the Effect.* Logos Press Limited, 1965.

[23] I. Akiyama, A. Hayama, and M. Nakajima, "Movement analysis of soft tissues by speckle patterns' fluctuation," *JSUM Proc*, pp. 615–616, Oct 1986.

[24] D. I. Barnea and H. Silverman, "A class of algorithms for fast digital image registration," *IEEE transactions on computers*, vol. 21, no. 2, pp. 179–186, 1972.

[25] D. Boggs, A. Baktha, J. Hawkins, T. Marr, J. Miller, P. Roussel, R. Singhal, B. Toll, and S. Venkatraman, "The microarchitecture of the intel pentium 4 processor on 90nm technology," *Intel Technology Journal*, vol. 8, pp. 1–17, 2004.

[26] B. S. Ramamurthy and G. E. Trahey, "Potential and limitations of angle-independent flow detection algorithms using radio-frequency and detected echo signals," *Ultrason Imaging*, vol. 13, pp. 252–68, Jul 1991.

[27] S. K. Alam and J. Ophir, "On the use of envelope and RF signal decorrelation as tissue strain estimators," *Ultrasound Med Biol*, vol. 23, no. 9, pp. 1427–33, 1997.

[28] S. Langeland, J. D'Hooge, P. F. Wouters, H. A. Leather, P. Claus, B. Bijnens, and G. R. Sutherland, "Experimental validation of a new ultrasound method for the simultaneous assessment of radial and longitudinal myocardial deformation independent of insonation angle," *Circulation*, vol. 112, pp. 2157–62, Oct 4 2005.

[29] B. J. Geiman, L. N. Bohs, M. E. Anderson, S. M. Breit, and G. E. Trahey, "A novel interpolation strategy for estimating subsample speckle motion," *Phys Med Biol*, vol. 45, pp. 1541–52, Jun 2000.

[30] J. D'hooge, "Principles and different techniques for speckle tracking," in *Myocardial Imaging - Tissue Doppler and Speckle Tracking* (T. Marwick, C.-M. Yu, and J. Sun, eds.), pp. 17–25, Blackwell Publishing, 2007.

[31] T. Bjåstad, S. Aase, and H. Torp, "Velocity sensitivity mapping in tissue Doppler imaging," *Proc IEEE Ultrason Symp*, vol. 4, pp. 1968–1971, 2005.

[32] C. B. Ingul, H. Torp, S. A. Aase, S. Berg, A. Stoylen, and S. A. Slordahl, "Automated analysis of strain rate and strain: feasibility and clinical implications," *J Am Soc Echocardiogr*, vol. 18, pp. 411–8, may 2005.

[33] B. H. Amundsen, T. Helle-Valle, T. Edvardsen, H. Torp, J. Crosby, E. Lyseggen, A. Stoylen, H. Ihlen, J. A. Lima, O. A. Smiseth, and S. A. Slordahl, "Noninvasive myocardial strain measurement by speckle tracking echocardiography: validation against sonomicrometry and tagged magnetic resonance imaging," *J Am Coll Cardiol*, vol. 47, pp. 789–93, Feb 21 2006.

[34] C. B. Ingul, A. Stoylen, S. A. Slordahl, R. Wiseth, M. Burgess, and T. H. Marwick, "Automated analysis of myocardial deformation at dobutamine stress echocardiography: an angiographic validation," *J Am Coll Cardiol*, vol. 49, pp. 1651–9, Apr 2007.

[35] C. Bjork Ingul, E. Rozis, S. A. Slordahl, and T. H. Marwick, "Incremental value of strain rate imaging to wall motion analysis for prediction of outcome in patients undergoing dobutamine stress echocardiography," *Circulation*, vol. 115, pp. 1252–9, Mar 13 2007.

[36] A. Stoylen, S. Malm, S. Aase, and E. Sagberg, "Aortic valve closure can be timed by tissue Doppler," *Eur J Echocardiogr*, vol. 5 Suppl 1, p. 159, 2004.

[37] S. A. Aase, A. Stoylen, C. B. Ingul, S. Frigstad, and H. Torp, "Automated detection of aortic valve closure in apical tissue Doppler images," *Proc IEEE Ultrason Symp*, pp. 2061–2064, 2004.

[38] S. W. Flax and M. O'Donnell, "Phase-aberration correction using signals from point reflectors and diffuse scatterers: basic principles," *IEEE Trans Ultrason Ferroelectr Freq Control*, vol. 35, no. 6, pp. 758–767, 1998.

[39] T. Hergum, T. Bjåstad, and H. Torp, "Parallel beamforming using synthetic transmit beams," *IEEE Trans Ultrason Ferroelectr Freq Control*, vol. 54, pp. 271–280, 2007.

Chapter 2

Automated strain and strain rate

Charlotte Bjork-Ingul and Svein A. Aase
Dept. Circulation and Medical Imaging, NTNU

2.1 Benefits of an automated method

Quantitative analysis of echocardiography has been a great technical challenge, and this is especially true for stress echocardiography. Deformation analysis from tissue Doppler imaging (TDI) has been considered to be a truly quantitative approach, but its clinical interpretation can be subjective and, therefore, requires a high level of expertise. Speckle tracking has been recently introduced as an alternative quantitative technique, but application of this method to echocardiography and stress echocardiography is in its infancy.

The clinical adaptation of strain and strain rate has been slow, due to variable data quality and time-consuming analysis. In the first applications using TDI for strain and strain rate analysis, manual positioning of the region of interest in each of the 16 segments was required. To obtain reliable data of the standard analysis myocardial segments have to be tracked through each frame to follow the myocardium throughout the cardiac cycle. Segment size, reverberations, and deviations between the axis of the wall and the directions of the ultrasound beams are all important additional considerations. The timing of cardiac events, such as aortic valve closure (AVC) and opening (AVO), has to be set manually. Both inter- and intra-observer variability are high, as the method is subjective and dependent on where the operator places the region of interest, as well as data-dependent. Traps for less-expert users abound, and apparently adequate curves can be obtained even if the region of interest is misplaced too close to the ventricle. [1]

In contrast, an automated approach could provide objective and rapid analysis as well as high feasibility and repeatability. In this chapter, we will describe in detail an example of an automated method for analyzing strain and strain rate that has been developed in our laboratory, called the Trondheim AutoStrain method.

2.1.1 Segmentation

Automatic segmentation requires automatic localization of anatomical landmarks (the mitral plane and the apex) and automatic localization of the myocardium. Automatic post-processing will give segmental values once the region of interest is defined. As regional variation is responsible for much of the variation of deformation measurements, ensuring full repeatability of segmentation would increase reproducibility of the automated method, compared to a manual method. Indeed, the variability of automated speckle-based strain has varied from 4-5% within observers to 7-10% between observers [2, 3, 4]. In contrast, an automated study based on combined TDI and speckle tracking has shown a higher variability compared to the B-mode-based modalities (Figure 2.1) [5].

Nonetheless, the automated setting of the region of interest with the automated approach may paradoxically reduce the feasibility of this method relative to the manual method. This is because the manual method allows the region of interest to be adjusted to avoid unsuitable areas such as reverberations. Automated analysis with a combination of TDI and speckle tracking has been shown to have a feasibility of between 75% and 80% of segments, compared to 92% with manual analysis by TDI [5]. Automated analysis using only speckle tracking resulted in a feasibility of 80% [3].

The issue of feasibility is balanced by analysis time. The total time used for analysis with an automated method was 2 minutes for 16 segments [5] compared to 11 minutes by the manual analysis. Another automated study has shown the duration of analysis to be 3 to 4 minutes per patient for the right ventricle [6].

2.1.2 Tracking

When tracking is used, a region of interest is set automatically in the myocardium at one frame and then tracked automatically through the cardiac cycle. This method allows the movement of cardiac tissue to be taken into account when extracting curves, although tracking is not mandatory for automated analysis of TDI. The region of interest is defined automatically, eliminating the search for suitable curves, thus resulting in more objective traces.

2.1.3 Timing

The Trondheim AutoStrain method includes algorithms for automatic timing of the cardiac events. This feature allows the analysis process to become more efficient. The use of timing data from the same cardiac cycle used in analysis also ensures more reliable timing than timing acquired from a different cardiac cycle.

2.2 Acquisition of data using tissue Doppler imaging, B-mode imaging, and combined imaging

Deformation measurements can be derived both from TDI data and B-mode data. Until recently, the predominant method has involved TDI, and most reported studies

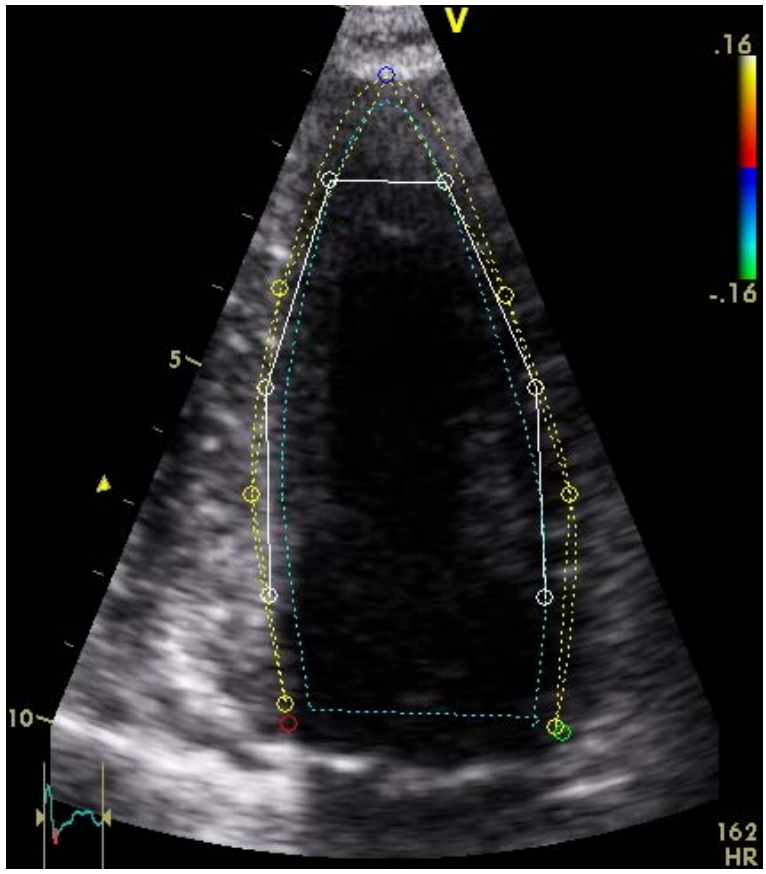

Figure 2.1: An automated system using TDI for tracking along the ultrasound beam and speckle tracking perpendicular to the ultrasound beam. In this apical four-chamber view from a healthy subject undergoing dobutamine stress echocardiography at peak stress, the left ventricle has been divided automatically into six segments, divided by yellow points. The white points represent the middle of each segment.

are based on this method. Improvements in two-dimensional (2-D) image resolution and post-processing algorithms have enabled speckle tracking in B-mode images. TDI and strain rate imaging (SRI) are limited to assessment along the ultrasound beam, but speckle tracking can in addition assess deformation perpendicular to the beam.

2.2.1 Tissue Doppler imaging

The high temporal resolution of TDI permits quantitation of brief events, such as isovolumetric contraction, and it enables cardiac events to be timed accurately. However, this high frame rate is achieved at the cost of spatial resolution. Analysis based on

tissue Doppler is dependent on B-mode for identifying the location of the cardiac structures. The restriction of accurate analysis to velocities along the ultrasound beam makes the technique angle-dependent, as well as restricting tracking to a single dimension.

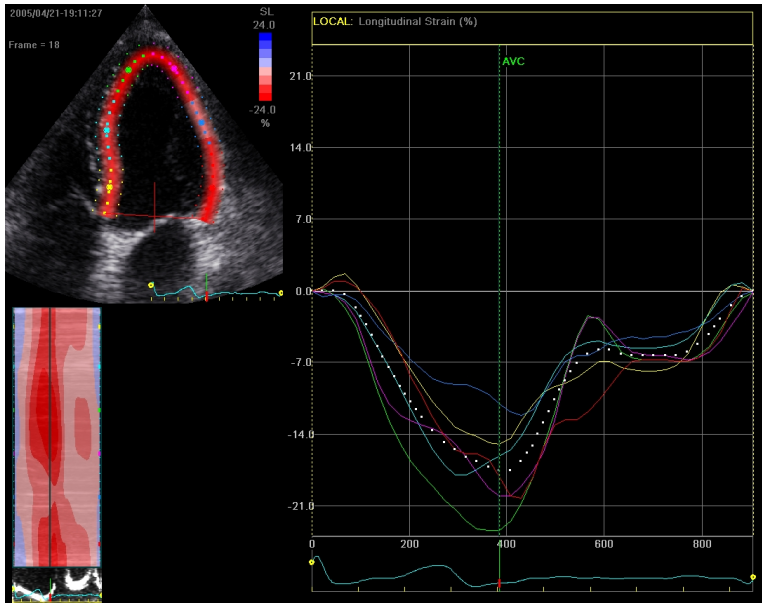

Figure 2.2: The 2D strain software package is illustrated in a healthy volunteer in an apical four-chamber view. The top left image shows a tracked curve at end-systole with the inner points representing the endocardial line, the midpoints the myocardium, and the outer points the epicardial line. Strain curves are illustrated to the right, and a curved anatomical strain M-mode is shown in the lower left image.

2.2.2 Speckle tracking

This new technique has been implemented in commercial software such as the 2D strain software package, part of EchoPAC (GE Medical Systems, Horten, Norway) and Velocity Vector Imaging (Siemens Medical Solutions, California, USA). Speckle tracking involves following the speckle pattern from frame to frame. Strain is derived through the relative displacement between two kernel regions by following the changes during several frames. However, if the frame rate is too low, large changes in the interference pattern are present from frame to frame and tracking will be poorer compared to higher frame rates. On the other hand, if the frame rate is too high, the spatial resolution will be poorer, making the speckles harder to recognize and follow. The advantage of these methods relative to TDI are that they are angle-independent and allow the possibility of tracking in two dimensions (hence, the software package

is denoted "2D strain"). On the other hand, their accuracy is dependent upon B-mode image quality and frame rate. The automated measurement of strain by speckle tracking has been validated by ultrasonomicrometry [3]. Commercially available software for the analysis of 2-D strain has been described as having the potential of becoming a standard for real-time automatic echocardiographic assessment of cardiac function (Figure 2.2) [2]. However, the current implementation of the 2D strain software package is not automatic but automated. The operator defines the endocardium at end-systole by placing two markers at the annular ring and one marker in the apex. Then AVC is defined manually, using the electrocardiogram (ECG). Tracking is then performed automatically, but the position of the endocardial line can be manipulated if the tracking quality is insufficient. Two additional lines are produced by the software - a middle line identifying the myocardium and the middle area of interest and an outer line that can be manipulated over the epicardium (but free of the pericardium) by the operator changing the width of the region of interest. This procedure takes approximately 35 sec per view. The software indicates if the B-mode frame rate is too low or if the tracking quality is insufficient.

Tracking of radiofrequency (RF) data can also be used for 2-D strain echocardiography and has been evaluated in an experimental work by Langeland et al. [7]. The method is based on finding the velocity vectors by tracking patterns in the RF image between consecutive frames.

Anatomic tracking is performed automatically after first manually defining the endocardial and epicardial borders of the region of interest in the beginning of systole. Velocity Vector Imaging has also been introduced recently. This technique has been applied to not only the left but also the right ventricle (Figure 2.3) [6].

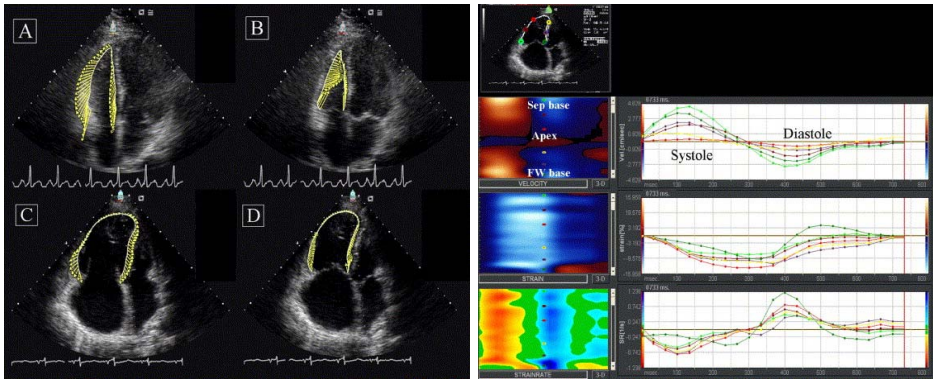

Figure 2.3: Velocity Vector Imaging is illustrated in a right ventricle. After manually drawing the endocardial border in one frame, the endocardial border is then automatically tracked throughout the cardiac cycle. The vectors indicate the direction of the motion and the amplitude of the velocity. A and B represent a healthy individual, and C and D show a patient with severe pulmonary hypertension. The right column images show velocity, strain, and strain rate curves to the right and curved anatomical M-modes to the left. From Pirat et al. [6]

2.2.3 Combination of tissue Doppler imaging and speckle tracking

The commercially available systems are based on either TDI or B-mode, which have unique advantages as well as disadvantages. The combination of both modalities allows their strengths to be combined (Table 2.1). TDI can provide the high temporal resolution necessary for accurate timing of the cardiac events and for quantification of cardiac events requiring high frame rate, as well as more accurate measurements of displacement along the ultrasound beam. Speckle tracking allows tracking and measurement of deformation in more than one direction.

2.3 Automated deformation analysis system

Functional analysis of the left ventricle requires knowledge of the location of the myocardium. To automate the analysis of cardiac ultrasound images, both the location of cardiac structures and information concerning the temporal relation between the images and the cardiac events are needed. In the Trondheim AutoStrain method [5], this knowledge is gained by first locating the positions of the apex and the two landmarks defining the atrioventricular plane (Figure 2.4A). This is achieved by an automatic method that uses TDI velocities and scores candidate landmarks based on gray-scale intensity, velocity profiles, and depth [11]. Having found the apex and the two atrioventricular landmarks, a simple initial generically shaped contour is fitted to these three points. This contour will then very roughly approximate the endocardium. Then, search lines are placed over the contour (Figure 2.4B). Candidate points representing the endocardial border along the search lines are found using an active contour model with a scoring function expressing the strength of candidate gradients from cavity to myocardium [12, 13, 14]. After identifying points at each search line, spline fitting is used to produce an endocardial contour (Figure 2.4B). The length of the endocardial contour is then divided into six equal-length segments and the seven points needed for defining the segments are relocated slightly to be 3 mm into the myocardium (Figure 2.4C). Thus, six segments in the myocardium are detected automatically in the end-diastolic frame of the ultrasound recording (Figure 2.4D).

The entire process, including landmark detection, endocardial detection, and segment border marker placement, is automatic and can be applied to all three standard apical views. The process does not always produce perfectly detected landmarks and a perfect endocardial contour, but this is not critical as the goal of the process is to automatically place the segment border markers. After the segment border markers are placed, the locations can be manually adjusted.

Having determined the segment border markers in end-diastole, tracking can be used to find the location of the markers in all frames of the cardiac cycle. In the Trondheim method [5], a combination of TDI and speckle tracking is used; axial tracking using TDI and lateral tracking using a sum of absolute differences speckle tracking algorithm [15]. TDI tracking of a marker at a given frame simply consists of calculating the displacement (in axial direction) of that marker from the velocity

Table 2.1: Methods using speckle tracking and/or TDI with automatic/automated technique.

Author	Number/ category	Method/ longi- tudinal, circum- ferential, radial	Reference	Feasibility	Intra- and inter- observer reprodu- cibility
Becker et al. [4]	64/MI	Speckle/ circ,rad	MRI	88%(rad strain)	4.4%/7.3% (rad strain)
Cho et al. [8]	30/ known or suspected CAD	Speckle/ circ,rad, long/ TDI/ rad,long	MRI	87% (TDI) 90% (speckle)	11%/21%(long TDI),17%/23%, (rad TDI),8%/ 15%(long speckle), 18%/22%(rad speckle),18%/ 17%(circ speckle)
Ingul et al. [5]	60/normal + MI	Speckle + TDI/ long,rad	Coro- nary angio- graphy	81%(strain rate)/80% (strain)	15%/15% coefficient of variation
Ingul et al. [9]	198/DSE	Speckle + TDI/ long,rad	Coro- nary angio- graphy	86%(strain rate)/79% (strain)	10%/16% coefficient of variation
Ingul et al. [10]	614/DSE	Speckle + TDI/ long,rad	Survival	93%(strain rate)/87% (strain)	
Amundsen et al. [3]	9 dogs ischemia/ 11 subjects	Speckle/ long,rad	Sono- micro- metry/MRI	85%/90% (strain)	5.2%/8.6% (strain)
Leitman et al. [2]	20 MI/ 10 normal	Speckle/ long,rad	Coro- nary angio- graphy	86%	5%/10%
Pirat et al. [6]	58 PAH/ 19 normal	Speckle/ VVI		82%/76%	4.7±4.7% (strain)/ 0.51±0.41 sec-1 (strain rate)
Langeland et al. [7]	5 sheep	Speckle	Sono- micrometry	90%	Correlation coefficient 0.72 radial/0.8 longitudinal strain

MI, myocardial infarction; DSE, dobutamine stress echocardiography; PAH, pulmonary arterial hypertension; VVI, Velocity Vector Imaging;rad radial; long longitudinal; circ circumferential.

at that location. B-mode intensity-based speckle tracking is performed in the lateral direction (Figure 2.5). To avoid drift, the tracking algorithm is applied both forward and backward through the cardiac cycle, and the results are averaged.

The results of tracking are visualized in the ultrasound sector as markers moving during the cardiac cycle. By visual assessment, the users can then discard or relocate and re-track markers with bad tracking.

Although the described landmark detection method is TDI-dependent, manually

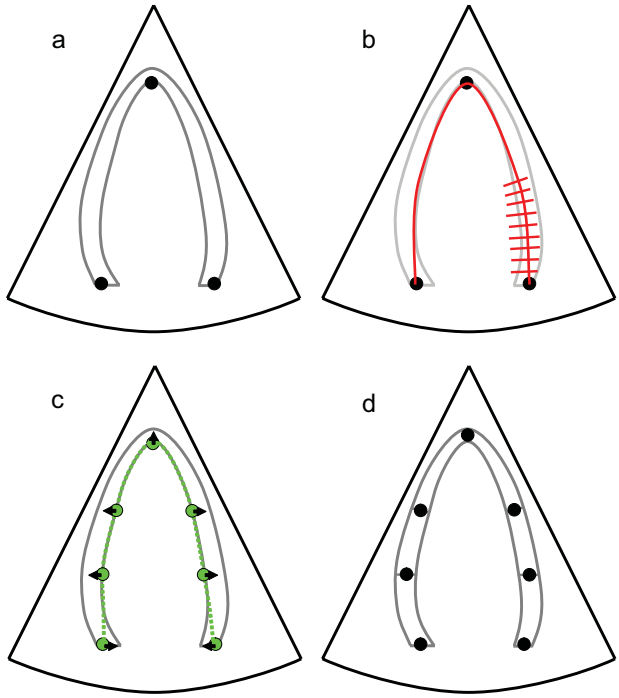

Figure 2.4: Ultrasound sector with apical view of left ventricle illustrating the initial steps of an automated analysis method. (A) Automatic detection of the landmarks defining the atrioventricular plane and the apex. (B) A generic ventricle-shaped initial contour is adapted to the detected points, and search lines for endocardial detection are placed over the contour. (C) The length of the detected endocardial contour is divided into six segments. The seven segment border markers are then pushed slightly to be positioned in the myocardium. (D) The segment border markers defined at one frame (end-diastole) can be tracked to get the location of the segment borders during the cardiac cycle.

setting the seven segment border markers with speckle tracking in both directions allows dynamic positioning of segment border markers to be achieved without TDI [3]. Based on this information concerning the segment markers, we tried four methods for strain and strain rate calculation to investigate the strengths and weaknesses of the different methods.

2.3.1 Static velocity gradient method

First, the geometric mid-point of each segment is located in the end-diastolic frame. The closest TDI beam to this point is then selected, and velocities from a predefined

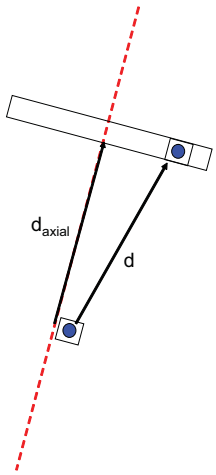

Figure 2.5: Tracking using the combination of TDI and speckle tracking. A pattern is displaced a distance (d) between two consequent frames. With TDI, the axial component (d_{axial}) of the displacement can be estimated. Using the estimated axial displacement, a limited search area for the lateral displacement can be positioned at the axial depth determined by TDI, thus speeding up the speckle tracking. To increase robustness, this process can be repeated with several neighboring kernels at the position of the pattern, and the resulting displacement vectors averaged.

distance in both directions along this beam are extracted for each frame in the cardiac cycle. The difference between the extracted velocities is then divided by the predefined geometrical distance, thus calculating strain rate. Strain is calculated by temporal integration and Lagrangian correction of strain rate (Figure 2.6) [16, 17].

2.3.2 Dynamic velocity gradient method

The position of the mid-point of each segment is located in all frames in the recording using the described tracking scheme. Then for all frames and segments, the closest TDI beam is located and strain and strain rate is calculated as in the static velocity gradient method (Figure 2.6).

2.3.3 Segment length method using tissue Doppler imaging for tracking

The positions of all segment border markers are located during all frames. For each pair of segment border points and each adjacent pair of frames, strain is calculated from the variation in segment length (L) in relation to starting length (L0), so strain is derived from the equation (L - L0)/L0. Strain rate is calculated as the temporal

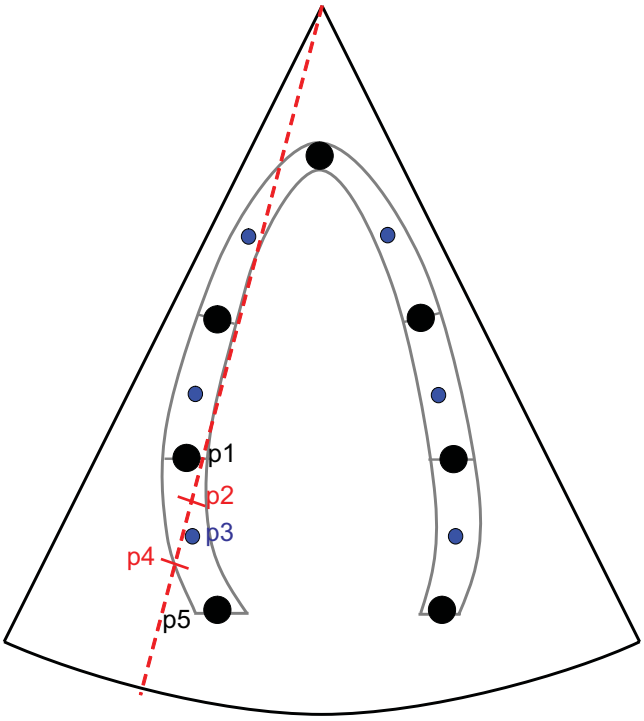

Figure 2.6: Ultrasound sector with apical view of the left ventricle illustrating differences between methods for calculating strain and strain rate. In the static velocity gradient and the dynamic velocity gradient methods, the closest TDI beam to the middle point (p3) of the segment is located, and velocities from two points along this beam (p2 and p4) are then extracted and used for strain rate calculations. In the static velocity gradient method, the middle point (p3) is static for all frames, whereas in the dynamic velocity gradient method, the middle point (p3) is at a new location for each frame. In the segment length methods, strain is calculated based on the dynamic positions of the segment border points (p1 and p5).

derivative of strain with Eulerian correction (Figure 2.6) [16, 17].

2.3.4 Segment length method without using tissue Doppler imaging

This method works as the previous method, but segment length variation is tracked by speckle tracking only (Figure 2.6).

Before automated analysis of the calculated strain and strain rate curves can be performed, the timing of cardiac events, especially AVC, must be determined.

2.4 Automatic timing of cardiac events

The major cardiac events (ejection and filling with consequent valve closure and opening) determine the movement of cardiac tissue. Therefore, extracted curves for displacement, velocity, strain, and strain rate from ultrasound recordings can, to varying degrees, be used for timing of cardiac events.

The four left ventricular events related to the left ventricular valves divide the cardiac cycle into its main phases. AVO and AVC are particularly needed to be able to determine several parameters related to ejection and shortening. The simplest approaches for timing AVC are the use of spectral Doppler of the blood flow through the aortic valve, or parasternal M-mode of the aortic valve. Several other methods have been used, including those using TDI and color M-mode [18, 19, 20], detection of the T-wave in ECG, phonocardiography of the second heart sound, and empirical regression relations based on heart rate calculated from ECG [21]. In some of these modalities, the timing of AVC is extracted from a separate recording and cardiac cycle than the recording where the timing of AVC is needed for analysis. Such approaches are not optimal, as the heart rate varies from cycle to cycle, even at rest [22].

With high frame rate TDI recorded from the apical position, the timing of AVC can be determined manually in all standard views (two-, three-, and four-chamber) [19, 23]. The detection of AVC is based on a short oscillation in the base of the left ventricle, provoked by AVC [24]. During closure, the basal tissue of the ventricle is moving away from the apex but stops with a slight "bounce" at the time of AVC. This event results in a shift from negative to positive velocities and also a positive acceleration peak (Figure 2.7).

Methods for automatically estimating the timing of AVC using TDI have been discussed by Aase et al. [21]. These automatic methods all rely on an automatic curve analyzer first identifying other events of the cardiac cycle (E-wave and mitral valve opening) and, thereafter, searching for AVC as the highest acceleration within a temporal search interval. Additionally, the methods rely on mechanisms for limiting the spatial area from which the velocity/time curves are extracted, such that the influence of mitral valve movement on the data is limited. The temporal resolution of the velocity/time curves is sufficient for AVC detection with TDI [5, 21]. If sufficient B-mode frame rate is provided and speckle tracking-based velocities are generated, such curves can probably also be used for AVC detection.

In the Trondheim AutoStrain method, the timing of AVO was automatically detected from peak acceleration in a search interval between 15 and 120 msec from the QRS complex using the same curves as used for timing of AVC. However, both the timing of AVO and AVC can be manually adjusted by the user with respect to the velocity, ECG, and strain and strain rate curves (when calculated).

The combination of a strain/strain rate curve with reasonable quality with knowledge of AVC and AVO allows several SRI parameters, such as peak systolic strain rate, time to end of shortening, postsystolic shortening, peak systolic strain, endsystolic strain, and time-to-peak systolic strain rate, to be identified automatically and placed on the curves. For analysis of the iso-volumetric relaxation and iso-volumetric relaxation phases, mitral valve opening and mitral valve closure are also

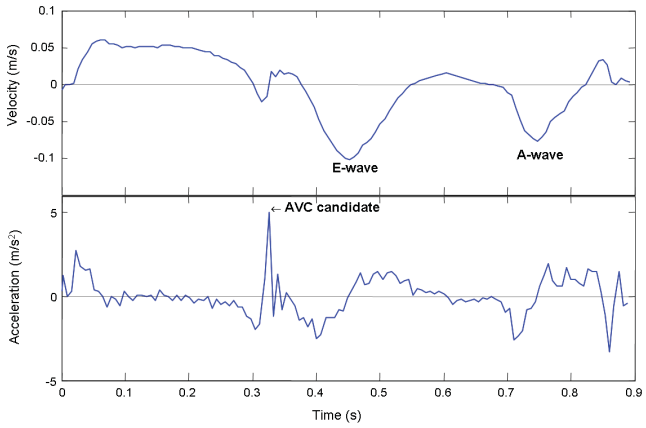

Figure 2.7: AVC can be detected as the peak positive acceleration in velocity/time curves extracted from the base of the left ventricle in the apical views.

needed.

2.5 Clinical use of an automated method

The automated analysis of strain and strain rate has been shown to be a clinically promising tool for the assessment of wall motion at rest and stress echocardiography.

One of the greatest potential benefits of the automated application is the ability to quantify wall motion changes with stress echocardiography and, thereby, develop an objective and rapid test of the functional significance of coronary artery disease (CAD). Clinical studies using TDI, speckle tracking, or a combination have been published over the past few years. In 197 patients referred for dobutamine stress echocardiography with clinically suspected CAD, 137 of whom had undergone coronary angiography [9], the number of analyzable segments at peak was highest for the manual method with 98%, followed by 84% for the speckle tracking method, and finally 80% for the TDI/speckle tracking method. Peak systolic strain rate and end-systolic strain were found to be the optimal variables for both automated TDI and speckle tracking methods to distinguish between CAD and no CAD. For peak systolic strain rate, the combined TDI/speckle tracking technique gave an overall sensitivity of 89%, specificity of 93%, and accuracy of 90%. The speckle tracking technique gave an overall sensitivity of 84%, specificity of 92%, and accuracy of 87%. Conventional wall motion score was, in comparison, significantly less sensitive (75%), but the specificity of 81% and accuracy of 77% were not significantly different from those of strain rate and end-systolic strain.

There have been three comparative studies between manual and automated analysis of strain and strain rate [2, 5, 8]. The first study compared 30 patients with acute myocardial infarction and 30 subjects with a normal left ventricle [5]. Echopac PC (GE Vingmed) was used for the manual analysis of strain and strain rate. The automated method was feasible, but with 12% fewer segments analyzable. The reproducibility was highest for the automated speckle tracking method. The second study included 20 patients with myocardial infarction, 10 healthy subjects, and 10 patients for comparing the 2D strain software package with manual TDI [2]. Among the segments that were suitable for wall motion analysis, 85% of the segments could be adequately tracked by the automated software. The correlation between the 2D strain software package and TDI was better for strain (r = 0.74) than for strain rate (r = 0.52). The third comparative study evaluated 30 patients with known or suspected ischemic heart disease with manual method and the 2D strain software package, validated by magnetic resonance imaging (MRI) [8]. They found radial 2-D strain to be more accurate and feasible to quantify regional function compared to TDI. Another study using automated speckle tracking and MRI tagging as reference compared seven patients with myocardial infarction and four healthy volunteers [3]. The 95% limits of agreement were -9% to 8% and the correlation for strain was good (r = 0.87).

We have also applied the automated method to predict outcome in patients undergoing dobutamine stress echocardiography with known or suspected CAD [10]. In this study of 646 patients with an average follow-up time of 5.2 years, automated SRI analysis of dobutamine stress echocardiography response gave independent and incremental information to standard wall motion score index. Segmental peak systolic strain rate had better predictive value than strain. Automated Velocity Vector Imaging was tested in a study of right ventricular function, including 48 patients and 19 age-matched controls. The optimal cutoff value for determining pulmonary artery systolic pressure >50 mm Hg using receiver operating characteristic curves was a strain rate of $-1.7sec^{-1}$ with a sensitivity of 80% and a specificity of 78% [6].

2.6 Future automated analysis systems

Research and development in ultrasound technology is likely to permit a higher acquisition rate than is currently available for both B-mode and TDI images. One promising technology to deliver this increase in data rate is the use of multiple parallel receive beams [25, 26]. Increased data rate can provide either increased temporal resolution, or improved lateral resolution, or a combination of both.

Automated analysis of such data would be facilitated by including features for automatically detecting artifacts - both those related to the methods used for high data rate imaging [27] and artifacts related to reverberations. If the analysis system could automatically detect the areas of the ultrasound sector with low quality data, the user could be made aware that further processing of such data would give uncertain results.

In the near future, the increased data rate will probably improve the data sets

used for 2-D strain and strain rate analysis. With even further increases in data rate, 3-D recordings with sufficient temporal and lateral resolution for strain and strain rate calculation may emerge. To calculate strain and strain rate in all directions, 3-D speckle tracking may be used [28]. The problem of features moving out of plane in 2-D speckle tracking can be avoided by using 3-D speckle tracking. A 3-D ultrasound recording will provide the possibility of analyzing all six walls using one recording. Analysis can be done on both long-axis and short-axis projections. Three-dimensional cardiac ultrasound will possibly speed up acquisition and provide more information than current 2-D recordings.

An automated analysis system for 3-D will provide some means of detecting and segmenting the myocardium (endocardium and epicardium) as well as a means for detecting the main cardiac events. Myocardial detection might be built on automated methods used for ventricular volume detection. As with the 2-D system, a 3-D system will also have to illustrate the tracking and preferably the calculated parameters for the user to evaluate.

2.7 Conclusion

The development of an automated strain and strain rate method for analyzing echocardiography and stress echocardiography has been shown to be feasible, time-saving, and more accurate than conventional wall motion scoring. The automated methods define the region of interest, and objective traces are obtained as there is no possibility of searching for a suitable curve. However, the feasibility is lower than for manual analysis. Strain and strain rate assessment by the automated method has been shown to increase accuracy compared to wall motion score for dobutamine stress echocardiography and to be a stronger predictor for the prognosis of all cause mortality.

The automated methods have so far been used only by experts. The critical next phase will be to move them to a non-expert environment.

References

[1] C. Ingul, *Quantification of regional myocardial function by strain rate and strain for evaluation of coronary artery disease*, vol. 163, p. 22. [Doctoral thesis]. Trondheim: NTNU, 2006.

[2] M. Leitman, P. Lysyansky, S. Sidenko, V. Shir, E. Peleg, M. Binenbaum, E. Kaluski, R. Krakover, and Z. Vered, "Two-dimensional strain-a novel software for real-time quantitative echocardiographic assessment of myocardial function," *J Am Soc Echocardiogr*, vol. 17, pp. 1021–9, Oct 2004.

[3] B. H. Amundsen, T. Helle-Valle, T. Edvardsen, H. Torp, J. Crosby, E. Lyseggen, A. Stoylen, H. Ihlen, J. A. Lima, O. A. Smiseth, and S. A. Slordahl, "Noninvasive myocardial strain measurement by speckle tracking echocardiography: validation against sonomicrometry and tagged magnetic resonance imaging," *J Am Coll Cardiol*, vol. 47, pp. 789–93, Feb 21 2006.

[4] M. Becker, E. Bilke, H. Kuhl, M. Katoh, R. Kramann, A. Franke, A. Bucker, P. Hanrath, and R. Hoffmann, "Analysis of myocardial deformation based on pixel tracking in two dimensional echocardiographic images enables quantitative assessment of regional left ventricular function," *Heart*, vol. 92, pp. 1102–8, Aug 2006.

[5] C. B. Ingul, H. Torp, S. A. Aase, S. Berg, A. Stoylen, and S. A. Slordahl, "Automated analysis of strain rate and strain: feasibility and clinical implications," *J Am Soc Echocardiogr*, vol. 18, pp. 411–8, may 2005.

[6] B. Pirat, M. L. McCulloch, and W. A. Zoghbi, "Evaluation of global and regional right ventricular systolic function in patients with pulmonary hypertension using a novel speckle tracking method," *Am J Cardiol*, vol. 98, pp. 699–704, Sep 1 2006.

[7] S. Langeland, J. D'Hooge, P. F. Wouters, H. A. Leather, P. Claus, B. Bijnens, and G. R. Sutherland, "Experimental validation of a new ultrasound method for the simultaneous assessment of radial and longitudinal myocardial deformation independent of insonation angle," *Circulation*, vol. 112, pp. 2157–62, Oct 4 2005.

[8] G. Y. Cho, J. Chan, R. Leano, M. Strudwick, and T. H. Marwick, "Comparison of two-dimensional speckle and tissue velocity based strain and validation with

harmonic phase magnetic resonance imaging," *Am J Cardiol*, vol. 97, pp. 1661–6, Jun 1 2006.

[9] C. B. Ingul, A. Stoylen, S. A. Slordahl, R. Wiseth, M. Burgess, and T. H. Marwick, "Automated analysis of myocardial deformation at dobutamine stress echocardiography: an angiographic validation," *J Am Coll Cardiol*, vol. 49, pp. 1651–9, Apr 2007.

[10] C. Bjork Ingul, E. Rozis, S. A. Slordahl, and T. H. Marwick, "Incremental value of strain rate imaging to wall motion analysis for prediction of outcome in patients undergoing dobutamine stress echocardiography," *Circulation*, vol. 115, pp. 1252–9, Mar 13 2007.

[11] A. H. Torp, S. I. Rabben, A. Stoylen, H. Ihlen, K. Andersen, L. A. Brodin, and B. Olstad, "Automatic detection and tracking of left ventricular landmarks in echocardiography," *Proc IEEE Ultrason Symp*, pp. 474–477, 2004.

[12] M. Kass, A. Witkin, and D. Terzopoulos, "Snakes: active contour models," *Int J Comput Vision*, vol. 1, pp. 321–31, 1987.

[13] B. Olstad and A. Torp, "Encoding of a priori information in active contour models," *IEEE Trans Pattern Anal Mach Intell*, vol. 18, pp. 863–72, 1996.

[14] S. I. Rabben, A. H. Torp, A. Stoylen, S. Slordahl, K. Bjornstad, B. O. Haugen, and B. Angelsen, "Semiautomatic contour detection in ultrasound m-mode images," *Ultrasound Med Biol*, vol. 26, pp. 287–96, Feb 2000.

[15] L. Bohs and G. Trahey, "A novel method for angle independent ultrasonic imaging of blood flow and tissue motion," *IEEE Trans. Biomed. Eng.*, vol. 38, pp. 280–286, 1991.

[16] A. Heimdal, *Doppler based ultrasound imaging methods for noninvasive assessment of tissue viability*, pp. 51–3. [Doctoral thesis]. Trondheim: NTNU, 1999.

[17] A. Stoylen, *Strain rate imaging of the left ventricle by ultrasound. Feasibility, clinical validation and physiological aspects*, pp. 64–9. [Doctoral thesis]. Trondheim: NTNU, 2001.

[18] F. Weidemann, M. Kowalski, J. D'Hooge, B. Bijnens, and G. R. Sutherland, "Doppler myocardial imaging. A new tool to assess regional inhomogeneity in cardiac function," *Basic Res Cardiol*, vol. 96, pp. 595–605, Nov 2001.

[19] J. U. Voigt, G. Lindenmeier, B. Exner, M. Regenfus, D. Werner, U. Reulbach, U. Nixdorff, F. A. Flachskampf, and W. G. Daniel, "Incidence and characteristics of segmental postsystolic longitudinal shortening in normal, acutely ischemic, and scarred myocardium," *J Am Soc Echocardiogr*, vol. 16, pp. 415–23, may 2003.

[20] F. Jamal, T. Kukulski, J. Strotmann, M. Szilard, J. D'Hooge, B. Bijnens, F. Rademakers, L. Hatle, I. De Scheerder, and G. R. Sutherland, "Quantification of the spectrum of changes in regional myocardial function during acute ischemia in closed chest pigs: an ultrasonic strain rate and strain study," *J Am Soc Echocardiogr*, vol. 14, pp. 874–84, Sep 2001.

[21] S. A. Aase, A. Stoylen, C. B. Ingul, S. Frigstad, and H. Torp, "Automatic timing of aortic valve closure in apical tissue Doppler images," *Ultrasound Med Biol*, vol. 32, pp. 19–27, Jan 2006.

[22] A. Stoylen, U. Wisloff, and S. Slordahl, "Left ventricular mechanics during exercise: a Doppler and tissue Doppler study," *Eur J Echocardiogr*, vol. 4, pp. 286–91, Dec 2003.

[23] A. Stoylen, S. Malm, S. Aase, and E. Sagberg, "Aortic valve closure can be timed by tissue Doppler," *Eur J Echocardiogr*, vol. 5 Suppl 1, p. 159, 2004.

[24] M. Kupari, "Aortic valve closure and cardiac vibrations in the genesis of the second heart sound," *Am J Cardiol*, vol. 52, pp. 152–4, Jul 1983.

[25] D. P. Shattuck, M. D. Weinshenker, S. W. Smith, and O. T. von Ramm, "Explososcan: A parallel processing technique for high speed ultrasound imaging with linear phased arrays," *J Acoust Soc Am*, vol. 75, no. 4, pp. 1273–1282, 1984.

[26] T. Hergum, T. Bjåstad, and H. Torp, "Parallel beamforming using synthetic transmit beams," *IEEE Trans Ultrason Ferroelectr Freq Control*, vol. 54, pp. 271–280, 2007.

[27] T. Bjåstad, S. Aase, and H. Torp, "The impact of aberration on high frame rate cardiac B-mode imaging," *IEEE Trans Ultrason Ferroelectr Freq Control*, vol. 54, pp. 32–41, 2007.

[28] J. Meunier, "Tissue motion assessment from 3D echographic speckle tracking," *Phys Med Biol*, vol. 43, pp. 1241–54, may 1998.

Chapter 3

Automatic Timing of Aortic Valve Closure in Apical Tissue Doppler Images

Svein Arne Aase[1], Asbjørn Stoylen[1,2], Charlotte Bjork Ingul[1], Sigmund Frigstad[3] and Hans Torp[1]
[1] Dept. Circulation and Medical Imaging, NTNU
[2] Dept. Cardiology, St. Olav Hospital, Trondheim, Norway
[3] GE Vingmed Ultrasound, Horten, Norway

Ultrasound color tissue Doppler imaging (TDI) can be used to estimate velocities of moving left ventricular cardiac tissue. Aortic valve closure (AVC) can be observed as a notch in apical TDI velocity/time curves occurring after ejection, but before early relaxation. This work sought to evaluate automatic and automated algorithms using TDI for timing AVC. Mitral valve position and the time point of early relaxation were extracted and used to accomplish the task. To test the algorithms, phonocardiogram of the second heart sound was recorded simultaneously with TDI and used as a reference method. The algorithms were tested on apical views of 16 healthy subjects. In 98% of the cardiac cycles, the automatic algorithm estimated the time point of AVC within 25 ms of the reference. Automatic detection of AVC might save manual effort and provide a marker separating ejection and diastole for further automated analysis. (E-mail: sveinaaa@ntnu.no)

3.1 Introduction

To evaluate specific parts of the cardiac cycle, information about timing is needed. Aortic valve closure (AVC) is important, marking the transition from end ejection to start of diastole. Several methods for timing AVC exist. Echocardiographic methods include parasternal M-mode of the aortic valve and spectral Doppler of the blood flow through the aortic valve. Other methods include phonocardiography of the second heart sound and empirical regression relations based on heart rate. Echocardiographic tissue Doppler recordings from the apical position are used for analysis, but conventional echocardiographic methods for timing AVC usually use other views or recording modalities; hence, giving timing information in separate cardiac cycles. The heart rate varies from cycle to cycle even during rest. At resting heart rate, the diastolic filling period varies far more with the cycle length than ejection period [1]. This means that the end ejection point (i.e., AVC) cannot be measured exactly from a different cardiac cycle or from heart rate, and timing of end ejection should be done in each cardiac cycle. Therefore, a method for determining AVC in the same cardiac cycle used for analysis will be useful, allowing parameters requiring accurate definition of end-systole to be more easily detected. Examples of such parameters are time-to-peak velocity as used in tissue synchronicity imaging [2, 3], systolic displacement [4], end-systolic strain [5], postsystolic strain index [6, 7] and IVR/ES strain index [8].

3.1.1 The timing of the cardiac cycle

The cardiac cycle is divided into different phases, opening and closure of the valves being the dividing events, as illustrated in Fig. 3.1 [9]. The initial deflections in ventricular activation (QRS) in an electrocardiogram (ECG) starts shortly before mitral valve closure (MVC), but detection of the first part of QRS is dependent on electrode position on the chest. The leading edge of the R-peak can be used as a rough reference point for the start of the contraction cycle. When ventricular contraction has raised the pressure above the atrial pressure, the mitral valve closes at the transition from diastolic filling to isovolumic contraction (IVC), during which, further contraction increases the pressure up to the level of the aortic pressure, without ejection or change in ventricular volume. As ventricular pressure exceeds aortic, aortic valve opens and ejection period (EP) commences. At about one third into EP, myocardial contraction terminates and relaxation starts, resulting in a decline in force. This causes ventricular pressure to fall slightly below aortic pressure, but the built up velocity continues ejection by inertia during the rest of the ejection period. Thus, there is volume reduction resulting in chamber narrowing and muscle fiber shortening during the whole of EP. The aortic valve closes (AVC) when ventricular pressure plus flow inertia drops below aortic pressure. Further relaxation results in a pressure drop with constant volume: isovolumic relaxation (IVR). When ventricular pressure drops below atrial pressure, mitral valve opens (MVO) at the start of diastolic filling period (DFP). Ventricular relaxation continues into early filling phase (E), creating a "suction" from the atria. DFP then has a purely passive flow phase (diastasis), and late filling caused

by atrial contraction (A), ending with MVC. The mitral valve separation during filling is proportional to the varying flow during this phase. The valve closures are audible in a stethoscope; first heart sound marking MVC and the second, AVC. P marks the start of atrial electrical activation and T marks the ventricular electrical deactivation.

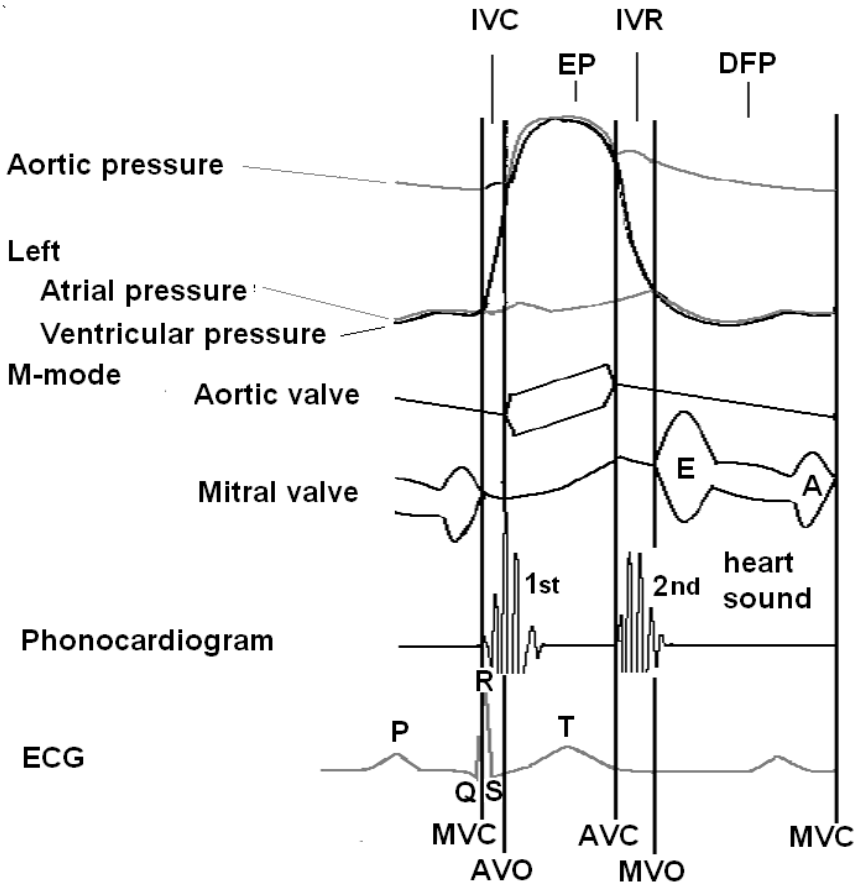

Figure 3.1: The phases of the cardiac cycle (after Opie [9])

3.1.2 Tissue Doppler imaging

Ultrasound (US) color tissue Doppler imaging (TDI) uses the Doppler effect to measure tissue velocities. The velocities are presented in a two-dimensional (2-D) color image similar to Doppler color flow imaging (CFI). TDI was introduced by McDicken et al. [10] and is implemented in several commercial US scanners. A higher frame rate is possible with TDI than with CFI. With the Vivid 7 scanner (GE Vingmed Ultrasound

AS, Horten, Norway), TDI frame rates of 160 frames/s simultaneously with grey-scale images at 40 frames/s are well within reach for apical images covering the entire left ventricle [11]. TDI is also the basis for strain rate imaging (SRI), imaging deformation of the cardiac muscle [12]. It is possible to extract the quantitative velocities used in a tissue Doppler image at each positional and temporal point. The TDI velocity of a tissue sample, however, only represents the velocity vector parallel to the ultrasound beam.

Normal tissue velocities of left ventricle by TDI are positive during IVC and EP, negative during E and A phases (denoted as E-wave and A-wave), and close to zero during diastasis, as shown in Fig. 3.2.

3.1.3 Timing of aortic valve closure using tissue Doppler imaging

Using phase analysis of US radio frequency (RF) signals, Kanai and Koiwa [13] were able to detect a steep pulse occurring at the time point of AVC. The available conventional TDI method did not have a sufficient frame rate for such detection. With improvements in acquisition, higher tissue Doppler frame rates, concurrently with grey-scale B-mode images at lower frame rates became possible [11]. With high frame rate TDI, Stoylen et al. [14] were able manually to detect AVC in the entire base of the left ventricle using apical views (four-chamber, two-chamber and long-axis views). As the open aortic valve suddenly closes, there is a slight motion away from the US probe, stopping with a slight "bounce" at the time point of the AVC, resulting in a shift from negative to positive velocity and a peak positive acceleration, as shown in Fig. 3.2 [14].

In the present work, we describe both automatic and automated (some manual effort needed) approaches for detecting AVC using TDI data from apical views, as well as a study validating the algorithms against phonocardiographic detection of the second heart sound. Previous work on this subject was presented by Aase et al. [15].

3.2 Methods

Information about other cardiac markers and cardiac events can be used to limit the search for AVC temporally and spatially. In this paper, the mitral ring points and events related to MVO and early relaxation (the E-wave) are detected first and used to guide search for AVC. A block diagram of the tested algorithms is shown in Fig. 3.3. The algorithms evaluated in this paper use the motion of the mitral ring points, which can be located in all apical views. Mitral ring points usually produce strong echoes and have higher velocity values during the cardiac cycle. TDI velocity/time curves from tracked mitral ring points are, thus, the most robust with respect to noise.

In the upper branch of Fig. 3.3, the user manually sets the two mitral ring points at one time instance on the 2-D grey-scale image. The points are then tracked through the cardiac cycle by a speckle tracking algorithm [16] in combination with TDI, as used by Ingul et al. [17]. Alternatively, the motion of the mitral ring points is

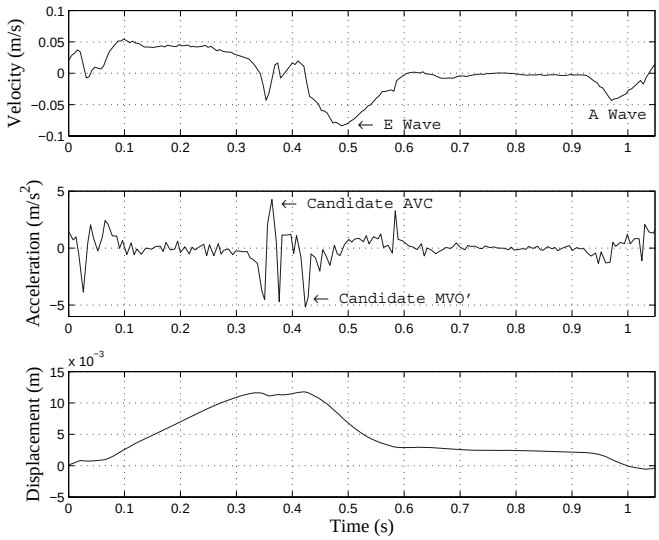

Figure 3.2: (top) TDI velocity curve with marked early relaxation (E-wave) and atrial contraction (A-wave); (middle) TDI velocity curve derived to get acceleration with candidate peak positive acceleration before MVO (AVC) and candidate peak negative acceleration within E-wave (MVO'); and (bottom) TDI velocity curve integrated to displacement.

automatically detected using a mitral ring detector [18] (lower left branch of Fig. 3.3). TDI velocity/time curves originating from the mitral ring points are then extracted and the E-wave is detected. The next step is a search for a MVO-related value (denoted MVO') in space and time. A temporal search interval for AVC is then set.

In the upper right branch of Fig. 3.3, AVC search is done in both time and space in the same manner as MVO'. The alternative (lower right branch in Fig. 3.3) is only searching in the velocity/time curves of the tracked mitral ring points. With both approaches, the result is one estimate for AVC for each wall in the image. The major steps of the algorithm are explained in more detail below.

3.2.1 Detecting the E-wave

The E-wave is detected as the first of the large negative dips of the velocity/time curves from the mitral ring points (Fig. 3.2). To do robust E-wave detection the velocity/time curves originating from the two mitral ring points were averaged. An automatic curve-analysis algorithm incorporating prior knowledge of length, excursion and rough timing of the E-wave and the A-wave, determined using the training set described in the "Data set for development" section, was used for actual detection of

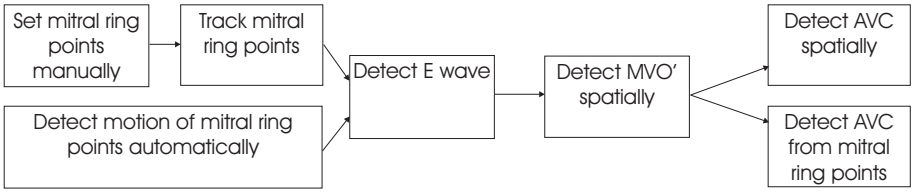

Figure 3.3: Block diagram showing an overview of AVC algorithms. Algorithms using the upper left blocks are automated algorithms (need some manual effort). Algorithms using the lower left block are automatic. Algorithms using the upper right block do both spatial and temporal searches for AVC, and algorithms using the lower right block only search for AVC temporally in velocity/time curves from the mitral ring.

the E-wave in the averaged curve.

3.2.2 Spatial and temporal search for MVO'

The mitral valve opens between AVC and peak negative E-wave. MVO causes very high acceleration values at certain points of the image, as the rapidly moving valve passes the points. A temporal search interval for MVO' was set from start, to peak E-wave (Fig. 3.4, top). The region-of-interest (ROI) for spatial MVO' search should cover the mitral valve when it opens. A region was defined midway between the tracked mitral ring points, limited above to be in the lower three fifths part of the image and below to match the deepest position of the tracked mitral ring points. This is shown in Fig. 3.5. Velocities for all cells within the ROI were extracted for all frames in the temporal search interval. The velocities were then differentiated and, for each cell, the time point and value of the largest negative acceleration was found. Finally, the cell in the ROI having the largest negative acceleration was found and, thereby, the point in the time interval and the ROI having the largest negative acceleration. Thus, a candidate time point for MVO' occurring slightly later than MVO was found.

3.2.3 Detecting AVC

After finding MVO', the temporal interval for AVC detection was set to avoid acceleration values occurring during the motion of the mitral valve (Fig. 3.4, middle and bottom). The start of the AVC interval was set at 22% of the cardiac cycle length before MVO' and the end of the interval at 5% of the cardiac cycle length before MVO'. AVC interval parameters were determined using the training set described in the "Data set for development" section. In the spatial search for AVC (upper right branch of Fig. 3.3), a procedure similar to that of MVO' was used. ROIs in space were set around the positions of each of the tracked mitral ring points, limited to the lower three fifths part of the image, and AVC was searched for in both ROIs (Fig. 3.5). Timing of AVC was then done by first extracting and differentiating the velocities for all frames in the ROIs and time interval. Then the cell in time and space, for each wall, having the largest positive acceleration value was used as the AVC estimate. Using

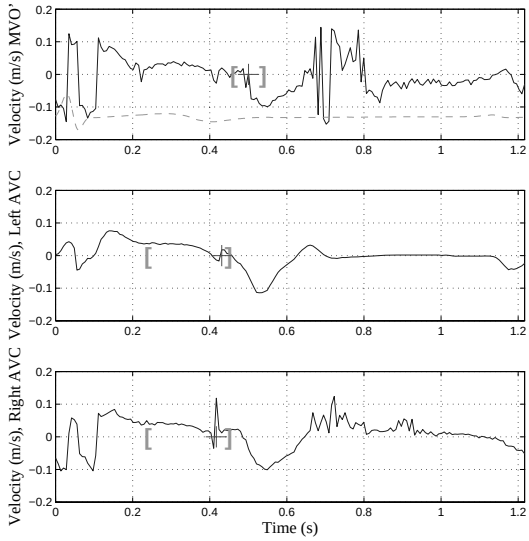

Figure 3.4: (top) TDI velocity curve from mitral ROI and scaled ECG; (middle) TDI velocity curve from left AVC ROI; and (bottom) TDI velocity curve from right AVC ROI. Brackets=temporal search intervals; crosses=detected timing estimates.

only the velocity/time curves of the mitral ring points (lower right branch of Fig. 3.3) was simpler. The velocities in the interesting time interval were differentiated and the time point of the largest positive acceleration value was detected. Again, one AVC estimate for each wall was produced.

3.2.4 Combining search methods

Although spatial search for AVC (upper right branch of Fig. 3.3) and mitral ring based search for AVC (lower right branch of Fig. 3.3) are separate methods, it is also possible to combine them. The tested combination consisted of primarily choosing timing by spatial search, but choosing mitral ring-based AVC timing when the difference between the timing estimates of the two methods exceeded 20 ms.

3.2.5 Data set for development

The algorithms were developed using apical TDI images from 30 patients with coronary heart disease and 28 healthy subjects, a total of 167 views/cardiac cycles (apical four-chamber, two-chamber and long axis). The images were recorded using a Vivid 5 and a Vivid 7 scanner (GE Vingmed) using the cardiac application with the 3S and M3S probes. TDI data were recorded concurrently with grey-scale B-mode data using

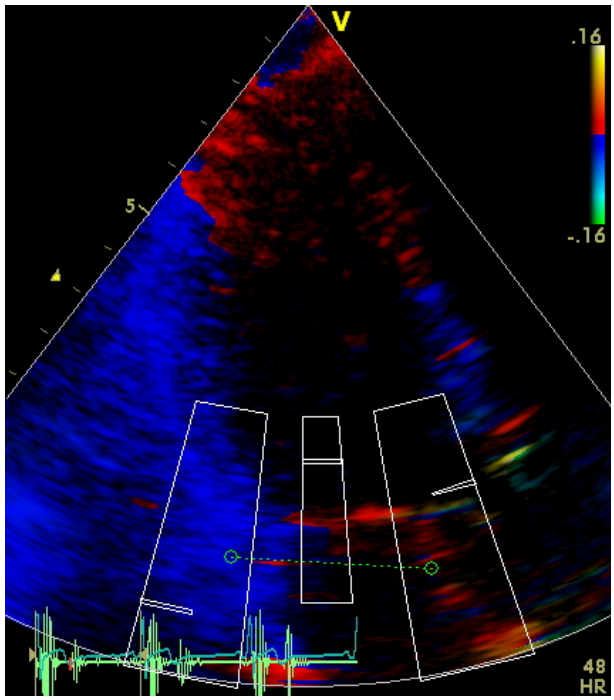

Figure 3.5: GcMat TDI screen-shot showing (green circles) tracked mitral ring points, (large rectangles) left AVC ROI, mitral ROI and right AVC ROI, (small boxes) locations of detected left AVC, MVO' and right AVC. The frame shown is that corresponding to the time point when right wall AVC was detected.

tissue velocity imaging (TVI) mode.

3.2.6 Analysis

The algorithms for detecting AVC were implemented as plug-ins to a customized US analysis toolbox (GcMat, GE Vingmed) for Matlab (MathWorks Inc, Natick, MA, USA). The toolbox features capabilities for automatic mitral ring detection, speckle tracking and extraction of velocities from TDI images at any time step and location of the images. To test the algorithms, apical TDI images were recorded for 16 healthy subjects (12 men, 4 women, 25-51 years old) examined during rest, in the left lateral supine position, using a Vivid 7 scanner. Recordings were made using the cardiac application with the M3S probe. TDI data were recorded using TVI mode. The mean resting heart rate was 63 bpm. Phonocardiographic recordings of the heart sounds (valve clicks) were acquired and displayed simultaneously with the echo recordings. The temporal resolution of the phonocardiographic signals used was 1.7 ms. Basically, the start of the second sound wave (A2) marks the valve closure, but low level noise as well as noise filtering can result in the observable start of the A2 signal not correctly

representing AVC. Therefore, the phonocardiographic signal was temporally calibrated by the valve click visible in Doppler flow recordings. Pulsed Doppler from the left ventricular outflow was recorded with simultaneous phonocardiographic signals and the average offset between the true valve click and the start of A2 in phonocardiogram was computed for each subject (Fig. 3.6). The average offset was then used for temporal calibration of the phonocardiographic signal recorded simultaneously with apical TDI. A2 in calibrated phonocardiogram was then used as the reference timing for AVC in apical TDI recordings. For each subject, three cardiac cycles were used (one from each of the apical four-chamber, two-chamber and long-axis views), a total of 48 cardiac cycles. The mean frame rate of the TDI images was 147 frames/s. To get robust estimates, velocities were averaged over three beams and ranges corresponding to 1 cm in the direction of the beams. No temporal averaging was applied. The algorithm steps before AVC timing were only validated by inspection. For the automatic mitral ring point detector, failure of detection was noted when the mitral ring points were detected at a distance more than 1 cm from the correct position. The performance of E-wave detection was evaluated by inspecting velocity/time curves with the detected E-wave indicated. Likewise, MVO' detection was evaluated by inspecting figures such as Fig. 3.4 and Fig. 3.5.

The difference between timing estimates of AVC by calibrated phonocardiogram and by the algorithms was then calculated for each cardiac cycle and analyzed using Bland-Altman analysis [19].

Empirical regression relations can be used to estimate AVC from heart rate. To compare the performance of such relations with the described algorithms, two linear relations were tested on the material against the calibrated phonocardiogram. Relation 3.1 [20] and relation 3.2 [21, 22] express the total electromechanical systole (QS_2) from the onset of the QRS complex on ECG to AVC as A2 on phonocardiogram with respect to heart rate. The data material used in the making of the relations were 86 boys, 13-19 ys for relation 3.1, and 121 men, 19-65 ys for relation 3.2. HR is heart rate in bpm, QS_2 in ms.

$$QS_2 = 498 - 1.6 * HR \tag{3.1}$$

$$QS_2 = 546 - 2.1 * HR \tag{3.2}$$

3.3 Results

Inspection of automatically detected mitral ring points showed successful detection in 43 (89.6%) of 48 cases. Failing cases were all apical long-axis views and, in four cases, only the right (anterioseptal) point failed. The E-wave detection, when the mitral points were set manually, was successful in all but three cases. Failure was noted caused by aliasing at the peak negative E-wave value. The same result was observed with automatic detection of the mitral ring points. MVO' detection seemed reasonable in all cases.

The automated algorithm (manual indication of mitral ring points) with spatial AVC search, selecting AVC from the wall with largest acceleration at AVC, had mean

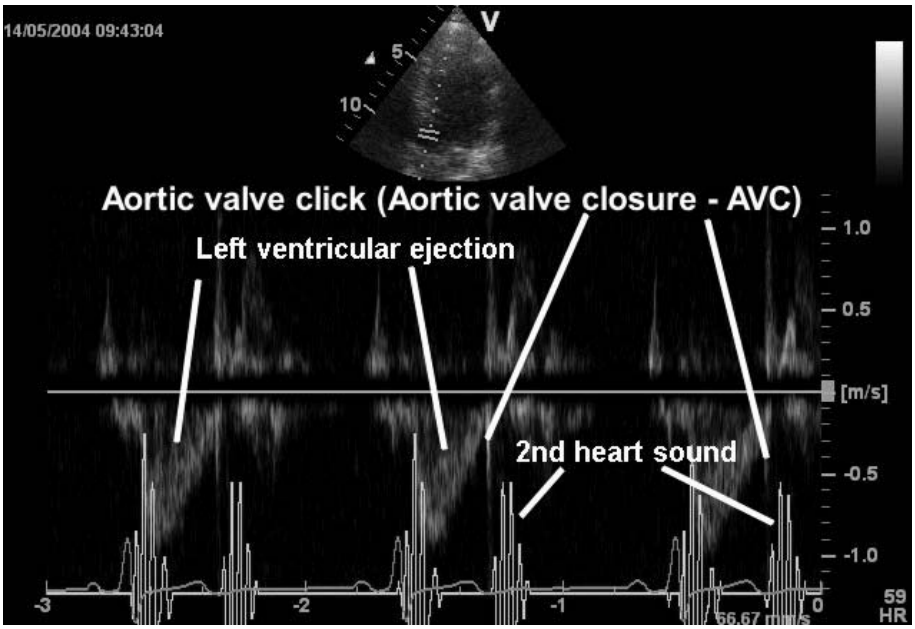

Figure 3.6: Doppler flow from left ventricular outflow tract. Ejection velocities are seen as the negative spectral curve and aortic valve closure click as the sharp spike at end ejection. ECG and phonocardiogram were recorded simultaneously. The audible sound of valve click is the start of the second heart sound. Because of filtering, first and second heart cycles show the start of the second heart sound slightly later than the Doppler spike but, in the third cycle, the start of the signal is not filtered and is truly simultaneous with AVC.

difference ± SD of 2.0 ± 16.3 ms against A2 in calibrated phonocardiogram (Fig. 3.7, upper left). Using the same algorithm, but always selecting AVC from left (septal, inferior, inferolateral) wall resulted in a mean difference ± SD of 1.7 ± 20.3 ms (Fig. 3.7, upper right). Always choosing AVC from the right (lateral, anterior, anterioseptal) wall resulted in a mean difference ± SD of 1.5 ± 26.2 ms. For each view, choosing the wall closest to the aortic valve resulted in a mean difference ± SD of 3.0 ± 15.7 ms.

Using the automated algorithm (manual indication of mitral ring point locations) with AVC search only in the velocity/time curves of the mitral ring points, selecting AVC from the wall with largest acceleration at AVC resulted in a mean difference ± SD of 3.8 ± 12.4 ms. The mean difference ± SD when always choosing AVC from the left wall was 0.5 ± 11.5 ms (Fig. 3.7, lower left) and, when always choosing AVC from right wall, was 1.6 ± 11.9 ms. Selecting AVC from the wall closest to the aortic valve resulted in a mean difference ± SD of 3.4 ± 11.6 ms.

Combining the two search methods (spatial and mitral based) by using AVC timing from the mitral ring points when the difference between the two methods exceeded 20 ms, resulted in a mean difference ± SD of -0.9 ± 10.1 ms (Fig. 3.7, lower right).

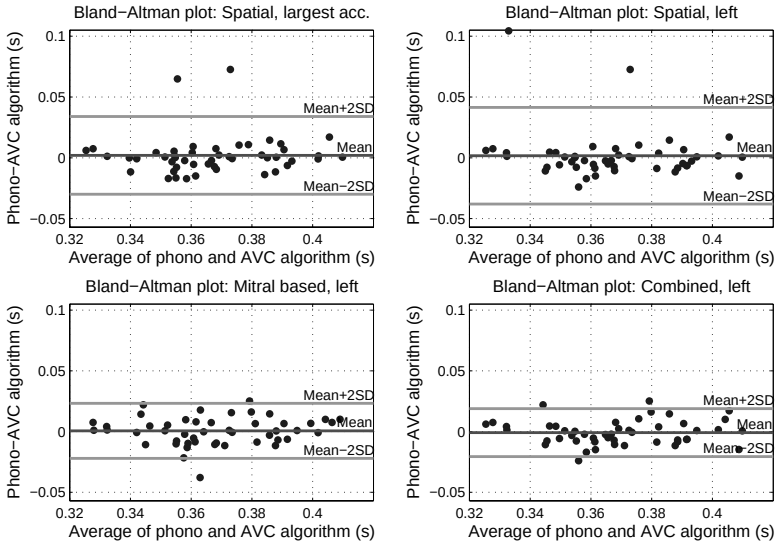

Figure 3.7: Bland-Altman plots of difference between A2 in calibrated phonocardiogram and AVC by automated algorithms. (top left) Spatial search, choosing AVC with largest acceleration; (top right) spatial search, choosing left AVC; (bottom left) mitral ring AVC search, choosing left AVC; (bottom right) combined search, choosing left AVC.

Using the automatic method (automatic mitral ring detector), the results were dependent on the success of the automatic mitral ring detector. Discarding one case with failed detection of left mitral ring point and using spatial search for AVC resulted in a mean difference ± SD of 1.3 ms ± 20.5 ms (Fig. 3.8, upper left). Search for AVC using the mitral ring point velocities resulted in a mean difference ± SD of -2.7 ± 8.9 ms (Fig. 3.8, upper right). For the 47 evaluated cases (98%), the difference between AVC by phonocardiography and by algorithm was less than 25 ms.

Combining the search methods, as for the automated method, the combined performance of the spatial search method and the mitral velocity method gave a mean difference ± SD of -3.1 ± 9.0 ms (Fig. 3.8, lower left, 47 cases of successful left point tracking).

The time usage of Matlab running the automatic algorithm with spatial search for AVC was 4.6 s (mean), and the automatic algorithm with temporal search for AVC in mitral point based velocities had a time usage (mean) of 4.5 s on a standard Pentium M 1.6 GHz computer. Using the empirical regression relations resulted in a mean difference ± SD of -28.1 ± 14.5 ms for relation 3.1 (Fig. 3.8, lower right) and -44.4 ± 16.2 ms for relation 3.2.

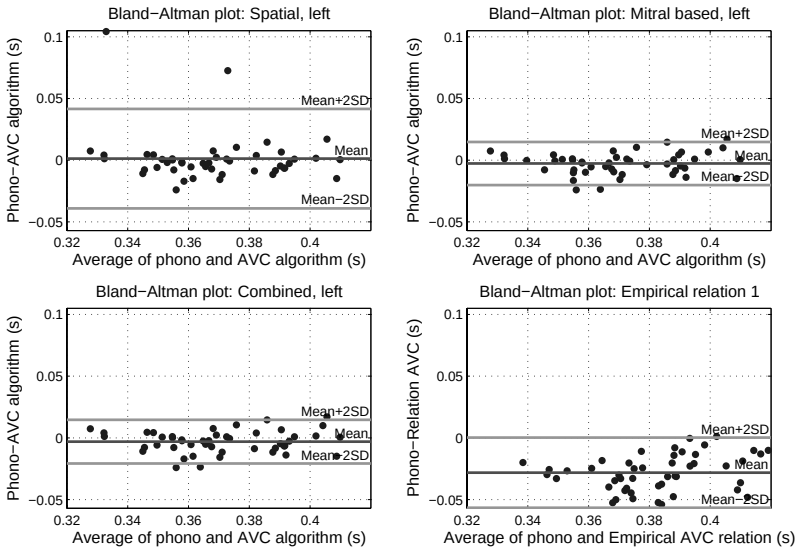

Figure 3.8: (Top left, top right, bottom left) Bland-Altman plots of difference between A2 in calibrated phonocardiogram and AVC by automatic algorithm (47 cases of successful left mitral ring point detection). (top left) Spatial search for AVC; (top right) AVC search using mitral ring point velocities; (bottom left) combination; (bottom right) Bland-Altman plot of difference between calibrated phonocardiogram and AVC by empirical regression relation 1.

3.4 Discussion

This study showed that automated and automatic algorithms for determining AVC using TDI were feasible and reliable during rest. The manual method for identifying mitral ring points, combined with speckle tracking, is reliable and quality is easily controlled visually [17]. The algorithm for automatic detection of mitral ring points used in this work also worked well in most tested cases (right point: 89.6%; left point: 98%). E-wave detection in this study was used for more robust AVC detection, not for E-wave measurement in itself. In three cases, aliasing at the E-wave caused failure in detecting the time point of E peak, but the timing estimate was close enough for further use by the AVC algorithm. Detection and automatic measurement of the E-wave is also valuable in itself, as the peak mitral ring E-wave velocity is an important measure of left ventricular diastolic function [23, 24]. Two methods for AVC search were considered, searching both spatially and temporally and searching for AVC only temporally in the mitral ring curves. The results showed that the latter was the more robust and faster alternative. However, discarding outliers, the results of the spatial search method seemed to be closer to zero, at least for the automated algorithm. This observation motivated testing the combination of the methods and, as seen in the

lower right plot of Fig. 3.7, SD was reduced compared with the method using the mitral ring points. In the spatial search with the automated algorithm, choosing AVC from the wall closest to the aortic valve resulted in lowest SD of differences. For the mitral-ring based approach, always choosing the left wall resulted in the lowest SD of differences. The mean of differences was clinically negligible in all cases. With the automatic algorithms, only the left wall was considered and therefore only results from always choosing the left wall were presented.

The automatic algorithm performed very well compared with the automated (partly manual) algorithm (Figs. 3.7 and 3.8). Again, the mitral ring based approach gave less variability than the spatial search method. The trend seen with the automated algorithms regarding combining search methods was not evident. The mitral ring based search was more robust than the spatial search. This might have been caused by the strong echoes and large longitudinal excursion evident at the mitral ring points, limiting the search to velocity/time curves from the mitral ring points and ensuring that the velocities used represented tissue motion.

Although the mitral ring-based method ensured that the velocities originated from the mitral ring, it might not have been the case that the mitral ring was the best location for detecting AVC effects. Although the spatial search method was more prone to hit estimates not related to AVC, it might also hit AVC better than the mitral ring-based method, when it actually hits as it searches in more locations. This observation was also the idea behind the combined approach, using the mitral ring-based approach when the absolute difference between the two methods exceeded a threshold and otherwise using the spatial approach. The AVC estimates by empirical regression relations are only rough estimates, not based on actual detection, but on a statistical relationship between heart rate and the time point of AVC. Such estimates can be calculated automatically as long as heart rate estimation with ECG triggering is automatic. The empirical regression relations both produce results with large negative bias (mean difference) when compared with the calibrated phonocardiogram reference. This might be caused by the regression relations expressing AVC from the start of QRS in ECG, and the triggering used as starting point for the calibrated phonocardiogram was closer to peak R in ECG. SD of differences was 39% lower for the best automatic algorithm compared with the best regression relation, showing that the regression gives a high variability because of the variation in diastole/systole ration with heart rate. To determine AVC by phonocardiography, the microphone placed on the chest of the subject must record the onset of A2. This was not trivial in all cases and required manual effort in adjusting filtering of the signal and the position of the microphone. Automatic AVC estimation using apical TDI as presented in this paper is an alternative to phonocardiography and empirical regression relations. The automatic algorithm with lowest SD of differences against phonocardiography had a mean difference $\pm$ SD of -2.7 $\pm$ 8.9 ms. This corresponds to 95% limits of agreement as used in Bland-Altman analysis of -20.1 ms and 14.7 ms, which are small enough for the automatic algorithm to be clinically useful.

3.5 Summary

Automated and automatic detection of AVC using TDI with apical insonation on resting subjects is feasible and reliable. In this study, automatic algorithms were also more accurate than empirical regression relations. TDI recordings and grey-scale images can be acquired simultaneously, resulting in an AVC estimate for the current cardiac cycle. This might save manual effort and open possibilities for further automated and automatic analysis of left ventricular function. Further work will include extending and testing the algorithms for cases with pathology and higher heart rates.

3.6 Acknowledgment

This work was supported by the Research Council of Norway and GE Vingmed Ultrasound AS, Horten, Norway.

References

[1] A. Stoylen, U. Wisløff, and S. Slørdahl, "Left ventricular mechanics during exercise: a Doppler and tissue Doppler study," *Eur J Echocardiogr*, vol. 4, pp. 286–291, 2003.

[2] A. Heimdal, *Method and apparatus for automatically measuring delay of tissue motion and deformation*. U. S. Patent Application 20040254486, 2004.

[3] J. Gorcsan, H. Kanzaki, R. Bazaz, K. Dohi, and D. Schwartzman, "Usefulness of echocardiographic tissue synchronization imaging to predict acute response to cardiac resynchronization therapy," *Am J Cardiol*, vol. 93, pp. 1178–1181, 2004.

[4] S. Bjaerum, B. Olstad, and K. Kristoffersen, *Ultrasound display of displacement*. U. S. Patent 6.592.522, 2002.

[5] C. Pislaru, C. Bruce, P. Anagnostopoulos, J. Allen, J. Seward, P. Pellikka, E. Ritman, and J. Greenleaf, "Ultrasound strain imaging of altered myocardial stiffness: Stunned versus infarcted reperfused myocardium," *Circulation*, vol. 109, pp. 2905–2910, 2004.

[6] T. Kukulski, F. Jamal, L. Herbots, J. D'hooge, B. Bijnens, L. Hatle, I. D. Scheerder, and G. Sutherland, "Identification of acutely ischemic myocardium using ultrasonic strain measurements. A clinical study in patients undergoing coronary angioplasty," *J Am Coll Cardiol*, vol. 41, pp. 810–819, 2003.

[7] F. Weidemann, C. Dommke, B. Bijnens, P. Claus, J. D'hooge, P. Mertens, E. Verbeken, A. Maes, F. V. de Werf, I. D. Scheerder, and G. Sutherland, "Defining the transmurality of a chronic myocardial infarction by ultrasonic strain-rate imaging: Implications for identifying intramural viability: An experimental study," *Circulation*, vol. 107, pp. 883–888, 2003.

[8] C. Pislaru, P. Anagnostopoulos, J. Seward, J. Greenleaf, and M. Belohlavek, "Higher myocardial strain rates during isovolumic relaxation phase than during ejection characterize acutely ischemic myocardium," *J Am Coll Cardiol*, vol. 40, pp. 1487–1494, 2002.

[9] L. Opie, "Contractile function of the intact heart," in *Heart disease: A textbook of cardiovascular medicine 6th ed.* (E. Braunwald, D. Zipes, and P. Libby, eds.),

pp. 462–464, Philadelphia London New York St. Louis Sydney Toronto: W.B. Saunders Co., 2001.

[10] W. McDicken, G. Sutherland, C. Moran, and L. Gordon, "Colour Doppler velocity imaging of the myocardium," *Ultrasound Med Biol*, vol. 18, pp. 651–654, 1992.

[11] J. Kirkhorn, S. Bjærum, B. Olstad, K. Kristoffersen, and H. Torp, "A new technique for improved spatial resolution in high frame rate color Doppler imaging," *Proc IEEE Ultrason Symp*, pp. 1947–1950, 2003.

[12] A. Heimdal, A. Stoylen, H. Torp, and T. Skjaerpe, "Real-time strain rate imaging of the left ventricle by ultrasound," *J Am Soc Echocardiogr*, vol. 11, pp. 1013–1019, 1998.

[13] H. Kanai and Y. Koiwa, "Myocardial rapid velocity distribution," *Ultrasound Med Biol*, vol. 27, pp. 481–498, 2001.

[14] A. Stoylen, S. Malm, S. Aase, and E. Sagberg, "Aortic valve closure can be timed by tissue Doppler," *Eur J Echocardiogr*, vol. 5 Suppl 1, p. 159, 2004.

[15] S. A. Aase, A. Stoylen, C. B. Ingul, S. Frigstad, and H. Torp, "Automated detection of aortic valve closure in apical tissue Doppler images," *Proc IEEE Ultrason Symp*, pp. 2061–2064, 2004.

[16] L. Bohs and G. Trahey, "A novel method for angle independent ultrasonic imaging of blood flow and tissue motion," *IEEE Trans Biomed Eng*, vol. 38, pp. 280–286, 1991.

[17] C. Ingul, H. Torp, S. Aase, S. Berg, A. Stoylen, and S. Slordahl, "Automated analysis of strain rate and strain: Feasibility and clinical implications," *J Am Soc Echocardiogr*, vol. 18, pp. 411–418, 2005.

[18] A. H. Torp, S. I. Rabben, A. Stoylen, H. Ihlen, K. Andersen, L. A. Brodin, and B. Olstad, "Automatic detection and tracking of left ventricular landmarks in echocardiography," *Proc IEEE Ultrason Symp*, pp. 474–477, 2004.

[19] J. Bland and D. Altman, "Measuring agreement in method comparison studies," *Stat Methods Med Res*, vol. 8, pp. 135–160, 1999.

[20] K. Wanderman, Z. Hayek, I. Ovsyshcher, G. Loutaty, A. Cantor, Y. Gussarsky, and M. Gueron, "Systolic time intervals in adolescents. Normal standards for clinical use and comparison with children and adults," *Circulation*, vol. 63, pp. 204–209, 1981.

[21] A. Weissler, W. Harris, and C. Schoenfeld, "Systolic time intervals in heart failure in man," *Circulation*, vol. 37, pp. 149–159, 1968.

[22] A. Weissler, "Systolic time intervals: Man.," in *Respiration and Circulation* (Altman and Dittmer, eds.), p. 310, USA: Federation of American Societies for Experimental Biology, 1971.

[23] S. Nagueh, K. Middleton, H. Kopelen, W. Zoghbi, and M. Quiñones, "Doppler tissue imaging: A noninvasive technique for evaluation of left ventricular relaxation and estimation of filling pressures," *J Am Coll Cardiol*, vol. 30, pp. 1527–1533, 1997.

[24] D. Sohn, I. Chai, D. Lee, H. Kim, H. Kim, B. Oh, M. Lee, Y. Park, Y. Choi, J. Seo, and Y. Lee, "Assessment of mitral annulus velocity by Doppler tissue imaging in the evaluation of left ventricular diastolic function," *J Am Coll Cardiol*, vol. 30, pp. 474–480, 1997.

Paper III is not included due to copyright.

Aase, Svein Arne ; Stoylen, Asbjørn ; Torp, Hans:
Aortic Valve Closure: relation to tissue velocities by Doppler and speckle tracking in normal subjects. European Journal of Echocardiography(2008) (Accepted)

Chapter 5

Velocity Sensitivity Mapping in Tissue Doppler Images

T. Bjåstad and S. A. Aase, and H. Torp
Dept. Circulation and Medical Imaging, NTNU

Tissue Doppler Imaging (TDI) velocities are estimated from a weighted averaged Doppler shift originating from a region with relatively large lateral span. The size and intensity of this region is not available to the TDI user and changes depending on scan settings and the imaged object. In this work a method for estimation and visualization of this region (the velocity sensitivity region) is presented. The method relies on B-mode images combined with simulated pulse echo responses.
In case studies the method highlighted the changing extent and intensities of the sensitivity region during the cardiac cycle. The method was also used for evaluating various scan setups. In a case with a high frame rate scan setup, the method clearly illustrated the advantage of applying Hamming apodization on receive compared to rectangular apodization.

5.1 Introduction

Ultrasound tissue Doppler imaging (TDI) uses the Doppler effect to measure tissue velocities. The velocities are presented in a two-dimensional color image similar to Doppler color flow imaging (CFI). TDI was introduced by McDicken et al. in 1992 [1] and is implemented in several commercial ultrasound scanners. A higher frame rate is possible with TDI compared with CFI due to shorter packet size.

Quantitative usage of TDI includes setting a region-of-interest (ROI) indicating the area from which velocities are to be extracted. Depending on the TDI scan settings, the region from which the velocities in fact are extracted might be substantially larger than indicated by the ROI (Fig. 5.1).

In this paper we introduce a method that estimates and visualizes the actual region from which a velocity estimate is acquired (the velocity sensitivity map, VSM), hence alerting the user when an inappropriate ROI is selected. The proposed method will also assist users to optimize their TDI setup.

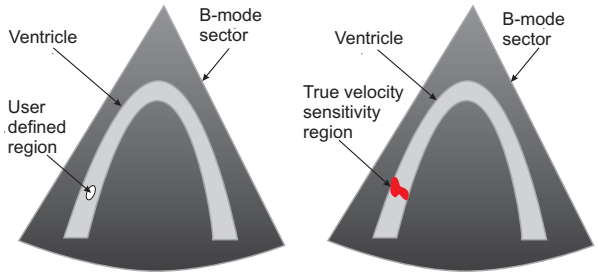

Figure 5.1: In quantitative TDI the user marks a region (left); The real sensitivity region where velocities originate from might be larger than the region marked by the user (right).

First the theoretical background and algorithm are described. Then the algorithm is evaluated in two case studies. In the last sections aspects of TDI sensitivity regions and the method are discussed along with the results.

5.2 Method

5.2.1 Theory

Using a linear model of an ultrasound imaging system, the received signal from a single insonification of an object can be described as the spatial convolution between the object scattering function and the imaging system's pulse-echo response,

$$p_r(t) = h_{pe}(\vec{r}, t) \otimes f_m(\vec{r}) \tag{5.1}$$

$$h_{pe}(\vec{r}, t) = h_{tx}(\vec{r}, t) \otimes h_{rx}(\vec{r}, t) \otimes v_{pe}(t) \tag{5.2}$$

where $\vec{r}$ is the spatial position, h_{pe} is the pulse-echo response, f_m is the object scattering function, accounting for the inhomogeneities in the imaged object, h_{tx} and h_{rx} is the spatial impulse response of the transmit and receive aperture and v_{pe} is the pulse-echo wavelet which includes transducer excitation and electro-mechanical impulse response during reception and transmission of the pulse [2].

Simplified, the RF-data from an image scan is a bandpass filtered version of the imaged object's scattering function. Since the lateral bandwidth of a B-mode scan is higher than for a TDI scan (assuming a small transmit aperture in TDI), the B-mode image is a reasonable estimate of the object scattering function. This under the assumption that the correlation length of the object scattering function is short, and that the power density spectrum of the B-mode pulse echo response is flat within the bandwidth of the TDI scan.

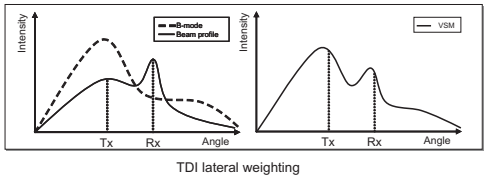

Figure 5.2: Strong scatterer in Tx direction causes highest image intensity in Tx direction (left). Beam profile has highest intensity in Rx direction but also a high side lobe in Tx direction (left). The resulting measured signal in Rx direction is more influenced by the signal in Tx direction than in Rx direction (right).

5.2.2 Algorithm

To calculate a VSM, velocity sensitivity mapping was performed using a B-mode image and a simulated pulse echo response as input:

$$VSM(\phi_m, r_n|\theta, R) = |h_{pe}(\phi_m, r_n|\theta, R)|^2 \cdot B_p(\phi_m, r_n) \tag{5.3}$$

$$B_p(\phi_m, r_n) = 10^{\frac{B_{log}(\phi_m, r_n)}{10}} \tag{5.4}$$

where B_{log} is the log compressed B-mode image at all image angles $\phi_m, m = 1, ..., M$, and image depths $r_n, n = 1, ..., N$. B_p is the log compressed B-mode image converted to power. h_{pe} is the pulse-echo response corresponding to an user specified point given in polar coordinates by θ and R.

As shown in Eq. 5.3 and Fig. 5.2, the pulse echo response simulated for a single selected position in the image (a given angle and depth) is combined with the intensity values of the current B-mode image to produce the VSM. To make the VSM correspond to a ROI of arbitrary extent, VSMs from several positions within the ROI are averaged:

$$VSM(\phi_m, r_n|\theta_k, R_k, k = 1, ..., K) = \sum_k w(k) \cdot |h_{pe}(\phi_m, r_n|\theta_k, R_k)|^2 \cdot B_p(\phi_m, r_n) \tag{5.5}$$

where $w(k)$ is a weighting function corresponding to the TDI samples contained inside the user specified ROI and K is the total number of ROI samples.

5.2.3 Setup

All B-mode images were recorded using a GE Vingmed Vivid 7 scanner with a M3S probe and 75° sector width. The pulse echo responses were all simulated using Field II [3], a Matlab simulation library based on linear propagation and spatial impulse responses [4]. The simulation software was set to emulate the M3S probe with several different hypothetical TDI-setups. Using the B-mode images and pre-calculated pulse-echo responses as input, the creation and visualization of VSMs were performed using Matlab (MathWorks Inc, Natick, MA, USA) and a customized ultrasound analysis

Table 5.1: Altered parameters in the simulated TDI setups.

	Rx apodization	TxAp diameter	# tx beams
1st setup	Rectangular	5.8	5
2nd setup	Hamming	5.8	5
3rd setup	Rectangular	8.9	10
4th setup	Hamming	8.9	10

toolbox (GcMat, GE Vingmed Ultrasound Horten, Norway). The VSM indicator was calculated for all frames in the B-mode recordings and presented as an overlay in the original B-mode images.

The applied ROIs in the experiments were set to be strictly longitudinal along one of the receive directions. To produce the VSM for a selected ROI in the image, pulse echo responses corresponding to the ROI were combined with each of the B-mode image frames in the cardiac cycle. This resulted in a dynamic VSM changing simultaneously with the underlying B-mode image cycle. The dynamic range of the displayed VSMs were set to 20 dB.

The following three beamforming parameters were altered: Receive apodization, transmit aperture diameter and number of transmit beams. All these parameters influence the lateral extent of the pulse-echo response, hence also the VSM. Pulse-echo responses from four hypothetical TDI setups were simulated. An overview of the altered parameters in the different setups is listed in Tab. 5.1.

To ensure high spatial resolution even at high frame rates, TDI-setups with parallel receive beams were simulated. In such a setup the pulse echo response from the receive beam midway between two transmit beams will have the highest side lobe level. This is referred to as worst case positions. The worst case beam profiles of the four tested setups are shown in Fig. 5.3. As can be seen in this figure, all simulated transmit aperture diameters were set to allow all parallel receive beams within the main lobe of the transmit beam. A Hamming window was applied on transmit to suppress sidelobes.

5.2.4 Setup for case study: Left ventricle, four chamber (4CH) view

During the cardiac cycle the left ventricle contracts and the walls thicken. The aim of this case study was to see how a VSM positioned in the wall would change during the cardiac cycle. An apical 4CH B-mode image was recorded and combined with the simulated pulse echo responses of the first setup in Tab. 5.1. Snapshots of VSMs overlaid the B-mode were extracted at six time steps through the cardiac cycle. VSMs were calculated to correspond to a ROI with 1.5 mm longitudinal length.

5.2.5 Setup for case study: Pericardium

The pericardium, surrounding the heart, is a strong scatterer compared to the myocardium. It is however almost static while the myocardium is moving. The aim of

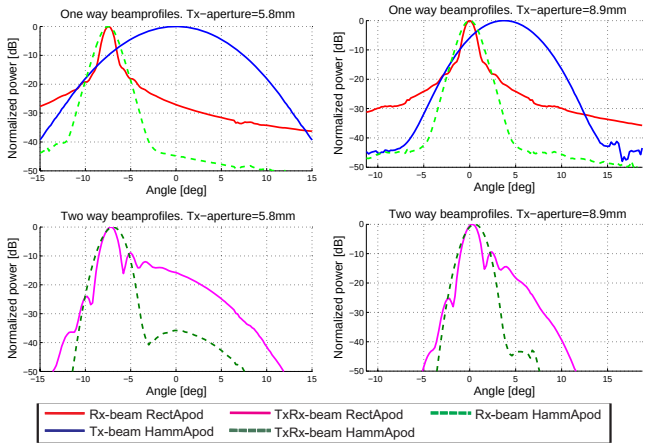

Figure 5.3: Worst case beam profiles for the investigated TDI scan setups (beam profiles were calculated as the radial mean square value of pulse-echo responses and displayed in dB scale). All profiles were simulated at a range of 80mm with transmit focus at 130mm. The two top figures are one way profiles, the bottom ones are two-way profiles. The first and second setup in Tab. 5.1 are shown to the left. The third and fourth setup to the right.

this case study was to use VSM to evaluate the signal contribution from pericardium when measuring velocities in the myocardium with and without receive apodization. A B-mode image where both pericardium and myocardium were visible was recorded of the lateral wall of a healthy adult male. A time instance of the recording where the transmit beam direction covered the pericardium and the worst case receive direction covered the myocardium was then chosen. A ROI with 1.1 mm longitudinal length was placed in this receive direction as shown in Fig 5.4 (left). In such a situation the received signal might have a large signal contribution in the direction of pericardium (the transmit direction). This might cause the measured velocity to be biased towards zero as illustrated in Fig. 5.5.

5.3 Results

B-mode images with VSM of the 4CH case are shown in Fig. 5.6. The 20 dB width of the VSMs varied between 2.3° (minimum) to 5.3° (maximum) during the cardiac cycle.

B-mode images with VSMs of the pericardium case are shown in Fig. 5.7. The corresponding averaged VSM intensity curves extracted from the depth indicated in Fig. 5.4 (right) are shown in Fig 5.8. The 20 dB width of the VSM at the selected time instance was 4.8° with Hamming apodization and 8.8° with rectangular apodization.

The intensity curves in Fig. 5.8 show that the B-mode intensity of the pericardium is 13.4 dB higher than for the myocardium. In the VSM curve for rectangular receive

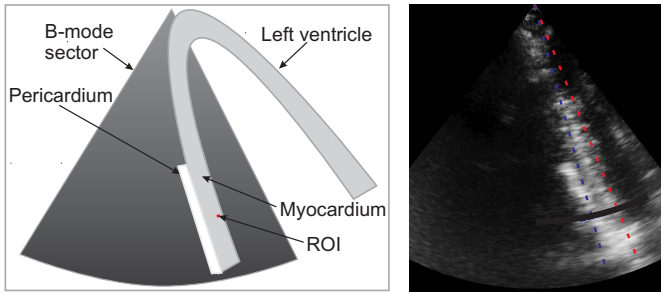

Figure 5.4: The pericardium of the heart is almost static while the myocardium is moving. Red line indicates the worst case receive direction (Rx), blue line is the corresponding transmit direction (Tx). The black sector area within the B-mode image illustrates the area/depth used when extracting data for analysis.

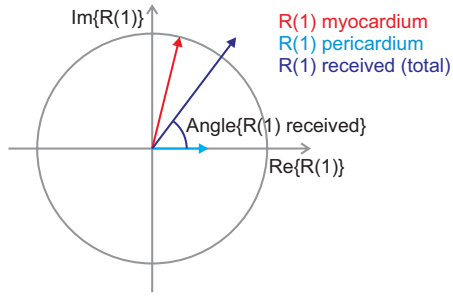

Figure 5.5: Using the autocorrelation method to estimate TDI velocities, the phase of the autocorrelation of lag one, $R(1)$, is directly correlated to the velocity estimate. In the case of a strong received signal component from pericardium, this phase shift will be biased towards zero.

apodization, the signal contribution from pericardium was only 3.3 dB lower than the contribution from the myocardium. Applying Hamming receive apodization this difference in signal contribution was increased to 21.6 dB.

The aperture size (and thereby the number of transmit beams) strongly influenced the lateral span of the two-way beam profiles. Increasing the transmit aperture from 5.8 mm to 8.9 mm (increasing the number of transmit beams from five to ten), the 20 dB width of the pulse echo beamprofile was reduced from 11.8° to 7.2° using rectangular receive apodization (Fig. 5.3, lower plots). A modest change from 5.3° to 5.0° was observed in the case of Hamming receive apodization.

Calculating VSM (merging B-mode and pulse echo response) took approx 0.1 sec for each B-mode frame (using Matlab on a Pentium M 1.5 GHz). Calculating the pulse echo response for one position in the B-mode image took on average 2.8 sec.

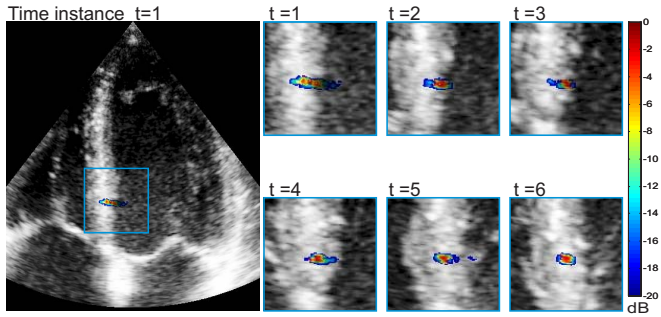

Figure 5.6: VSMs with rectangular apodization on receive extracted from six following time instances of the cardiac cycle.

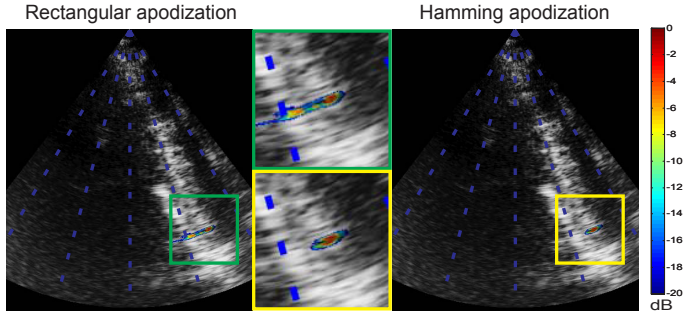

Figure 5.7: VSM with rectangular and Hamming apodization on receive in the figure to the left and right, respectively. Note the narrower VSM when applying Hamming apodization.

5.4 Discussion

This work introduced a method for velocity sensitivity mapping using simulated pulse echo responses and B-mode images as input.

The 4CH case study illustrated that the VSM is dynamic, changing simultaneously with the underlaying B-mode recording. It also illustrated that some sort of tracking is inherent in TDI, the VSM picked up areas of strong B-mode intensities even when these were not in the selected measurement direction.

In the pericardium case study, both intensity curves and the VSM indicated high signal contribution from the pericardium when measuring velocities in the myocardium direction, hence that measured velocities would be biased towards zero, as showed in Fig. 5.5.

The broad VSM, covering both myocardium and pericardium, was caused by two factors. The first factor regards the large dynamic range in backscattering from tissue. Secondly the simulated TDI-setups applied parallel beamforming in combination with few transmit beams to increase the frame rate. Inherent in such setups is an offset

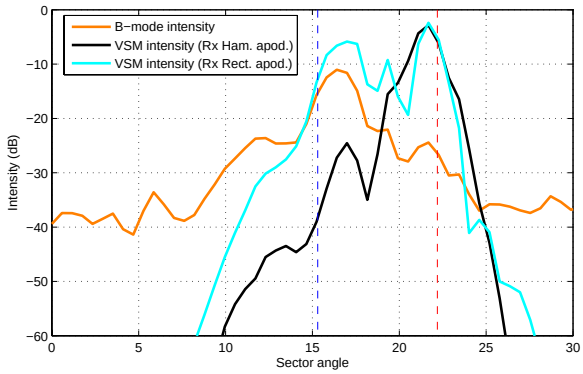

Figure 5.8: Intensity curves extracted from time instance and (black) area of interest in Fig. 5.4 (right). Red line represents Rx direction, blue line represents Tx direction. Note the improved separation between transmit and receive direction when using Hamming apodization.

between transmit and receive directions and wide, weakly focused transmit beams. This caused high side lobe levels, as can be seen in Fig. 5.3. Another aspect of parallel beamforming, not shown in this work, is significant beam-to-beam variations in the pulse-echo responses [5]. Using VSMs such variation would be apparent.

Applying Hamming apodization in the pericardium case resulted in a much narrower VSM, indicating far less signal contribution from the pericardium.

This work did not regard the impact of clutter filtering. In the pericardium case, a clutter filter would probably reduce the effect that pericardium has on lowering the myocardium velocities.

The current implementation of velocity sensitivity mapping was done through offline processing. Using pre-calculated pulse-echo responses for the whole scan sector, the total required processing time from the selection of an ROI in the B-mode image to the VSM was appearing dynamically in a loop of 40 B-mode images was approximately 4 seconds on a standard laptop. No speed optimization effort was made in this implementation. It is then reasonable to assume that an optimal implementation of this method on a scanner can reduce the processing time to real time requirements.

5.5 Conclusion

Velocity sensitivity mapping provides a visualization (Velocity Sensitivity Map, VSM) of the spatial signal contribution to velocity estimates in TDI. A VSM can thus be used to quickly evaluate the applicability of a selected ROI.

For cases with large receive beam offset to the transmit beam, the VSMs indicated that receive Hamming apodization can reduce the lateral span of the region which contributes to the estimated velocity. With a narrower VSM, signal contribution from

strong scatterers outside the intended ROI can be avoided. The simulated beamprofiles indicated that increasing the number of transmit beams would have a similar effect, but at the cost of lower frame rate.

References

[1] W. McDicken, G. Sutherland, C. Moran, and L. Gordon, "Colour Doppler velocity imaging of the myocardium," *Ultrasound Med Biol*, vol. 18, pp. 651–654, 1992.

[2] J. A. Jensen, "A model for the propagation and scattering of ultrasound in tissue," *J Acoust Soc Am*, vol. 89, pp. 182–190, jan 1991.

[3] J. A. Jensen, "Field: A program for simulating ultrasound systems," *Medical & Biological Engineering & Computing*, vol. 34, Suppl. 1, pp. 351–3, 1996.

[4] J. A. Jensen and N. B. Svendsen, "Calculation of pressure fields from arbitrarily shaped, apodized, and excited ultrasound transducers," *IEEE Trans Ultrason Ferroelectr Freq Control*, vol. 39, pp. 262–267, 1992.

[5] T. Hergum, T. Bjåstad, and H. Torp, "Parallel beamforming using synthetic transmit beams," *Proc IEEE Ultrason Symp*, vol. 2, pp. 1401–4, 2004.

Chapter 6

The Impact of Aberration on High Frame Rate Cardiac B-Mode Imaging

T. Bjåstad and S. A. Aase, and H. Torp
Dept. Circulation and Medical Imaging, NTNU

In echocardiography, especially in 3D echocardiography, achieving high frame rates is a major challenge. A suggested solution is parallel receive beamforming. Without any compensation, this approach is known to produce block-like artifacts, where each block corresponds to one parallel receive group. In this work, in vitro imaging, in vivo imaging, and simulations were used to investigate the artifacts. In vitro, imaging a tissue phantom, the artifacts were successfully compensated for. However, in vivo, imaging the heart, the compensation techniques no longer sufficed and the artifacts persisted. With in vivo imaging, aberrating tissue layers are present between the heart and the probe. To investigate the effects of aberration on a parallel receive system, an in vitro experiment was performed with and without a silicon phase aberrator in front of the probe. The aberrator caused the artifacts to appear even when compensation techniques were applied. Simulations confirmed the measured results and indicated that distorted beam profiles and decorrelation between parallel receive groups caused the artifacts. To quantify the magnitude of the artifacts, a correlation-based indicator was developed. The indicator separated images with and without artifacts and confirmed that the artifacts appeared from the combination of parallel receive beams and aberration.

6.1 Introduction

To study deformation in all phases of the cardiac cycle, sufficient temporal resolution, frame rate, is needed. Using 3D ultrasound, far more data have to be recorded in the same amount of time, thus making it more challenging to achieve a high frame rate.

To achieve high frame rates and still keep sufficient spatial resolution, parallel

receive beams can be applied [1, 2]. Using parallel receive beams, multiple scan lines are acquired for each transmit event, hence increasing the frame rate. Parallel beamforming is therefore also known as multiple line acquisition (MLA). As described in [3, 4, 5] this technique has some challenges due to misalignment of the transmit and receive beams. If not compensated for, this causes block-like artifacts in the B-mode images and also a periodical lateral gain variation pattern. These effects will be referred to as MLA artifacts.

Several compensation methods have been proposed. In U.S. patents [4] and [6], the authors describe incoherent methods for beam interpolation applied after detection of the RF signal. These methods take nonuniform lateral distribution of two-way beam profiles and gain variation into account. In [5], coherent interpolation is used to produce synthetic scan lines in between the original ones, taking advantage of the fact that the lateral bandwidth increases in the detection step. This increases the beam density and thereby reduces the required number of MLA channels. Another method for MLA correction is described in [3], where synthetic transmit beams are generated in the direction of each receive beam by interpolating the RF-signal from each transducer element prior to receive beamforming. Coherent interpolation between scan lines from different transmit pulses is sensitive to rapid motion. This limits the applicability of the two latter methods in cardiac imaging. A solution with dynamic beam steering is suggested in [7]. In this solution the receive focusing is steered dynamically in the lateral direction to compensate for the nonuniform lateral distribution of two-way beam profiles.

When imaging the heart, the transmit and receive beams of an ultrasound system will be distorted due to inhomogeneities in the body wall. This phenomenon is known as aberration. MLA systems require a specific geometric relation between the transmit and receive beams. Since aberration distorts the beams, it is likely that aberration will have an effect on the ability to correct for MLA artifacts.

We show that cardiac in vivo MLA images contain block artifacts even when beam steering and gain compensation techniques are used. A major difference between in vitro images, where compensation is successful, and cardiac images, where compensation fails, is aberration. In this paper we therefore investigate the impact of aberration on MLA imaging systems, suggesting that aberration is a major reason for failing compensation in cardiac MLA images.

The outline of this investigation is as follows: First, the artifacts of MLA are explained and demonstrated in vivo. Having established the problem, it is shown that these artifacts can be corrected when imaging a tissue mimicking phantom where no aberration is present. When placing a thin silicon aberrator between the probe and phantom, it is shown that the compensation techniques no longer suffice. Further, the effects and mechanisms of aberration in conjunction with MLA are investigated through simulations and correlation analysis.

6.2 Theory

6.2.1 Multi-Line Acquisition

The transmit and receive directions of an MLA setup are illustrated in Fig. 6.1. Thin lines indicate receive directions and thick lines the transmit directions. Several receive scan lines are formed in parallel for each transmit event and constitute an MLA group. An MLA system with four parallel receive lines in each MLA group will be referred to as a 4MLA system.

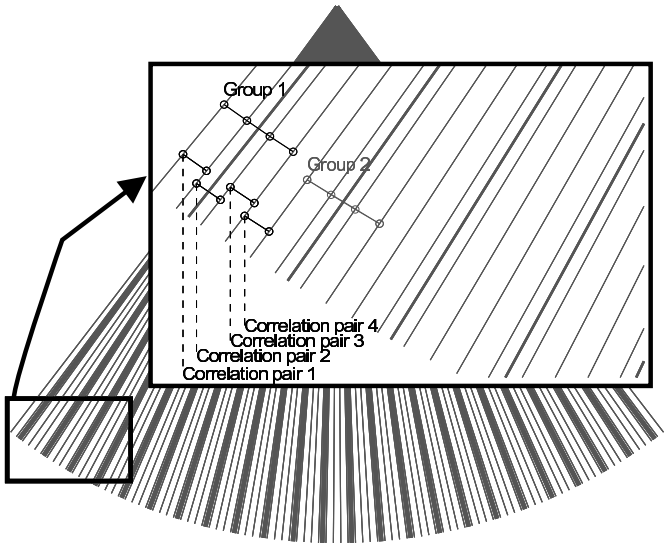

Figure 6.1: 4MLA ultrasound scan grid with Tx lines (thick) and Rx lines (thin). Magnified section: Part of ultrasound scan grid with visualization of MLA groups and scan line correlation pairs.

As described in [3], MLA image artifacts are caused by the misalignment of the transmit and receive beams. The misalignment pulls the lateral maximum of the two-way beam profiles toward the transmit beam lateral maximum. This causes irregular overlaps between adjacent two-way beam profiles. If not compensated for, there will be a gap in the sampling between the MLA groups and hence irregular sampling. This effect is referred to as warping and causes sharp lateral discontinuities in the image. The discontinuities can be seen as the edges of the block artifacts in the images. As proposed by [7], this warping can be compensated for by steering the receive beams an appropriate amount away from the transmit beam. This will result in more regular lateral sampling. Since the warping effect varies with depth, this steering should ideally be dynamic. However, a static steering offset will be sufficient as long as the beam widths of the transmit and receive beams are constant over the relevant depth range.

Another effect of the transmit-receive misalignment is that the shape of the beam profiles is asymmetric and changes from beam to beam within an MLA group. The variation in shape will result in a variation in overlap between adjacent two way beam profiles. This effect is referred to as skewing.

A third effect is that the outermost two-way beams in a 4MLA group have a lower sensitivity than the innermost. This causes a periodical lateral gain variation pattern in the image. The lateral gain variation pattern can be compensated for based either on a priori knowledge of the transmit and receive beams or on the measured gain variations in the recording. In the first approach, based on a priori knowledge, the gain compensation can be found by integrating two-way beam profiles. Estimating the gain variations from the recordings can be done in several ways. A straight forward technique is to calculate the relative gain variations internally in each MLA group. Averaging these internal variations for MLA groups in all positions, depths and frames will give a set of gain compensation values relatively independent of the imaged object. This method produces a number of gain compensation values equal to the size of an MLA group. A prerequisite for using only these compensation values is that the gain variations be constant throughout the image. This again requires the transmit and receive beam width to be constant. This will in most cases only be valid in a limited area (roughly equal to the depth of focus).

6.2.2 Correlation Analysis

The most important contributor to MLA artifacts is assumed to be irregular overlap between adjacent two way beam profiles. This causes irregular sampling of the imaged object. With correlation analysis of each pair of adjacent scan lines, the distribution of correlation values will be related to the regularity of the sampling. With regular sampling, all pairs should show similar correlation. In the case of irregular sampling, different pairs will have different correlation. To detect differences in correlation, the correlation values of each pair must be compared with the other pairs. A likelihood ratio test can be performed to find sufficient statistic for separating two different correlation values.

Letting $X = [x_1, x_2]$ where x_1 and x_2 are complex demodulated RF data from two adjacent scan lines, and modeling the signal as a zero mean complex Gaussian process, the probability density function is

$$p(X) = \pi^{-2}|C|^{-1}e^{X^H C^{-1} X}. \tag{6.1}$$

(From Eq. 15.17 in [8].) Assuming equal variance, σ^2, the covariance matrices under hypothesis H_0 and H_1 are

$$H_0 : C_0 = \sigma^2 \begin{bmatrix} 1 & \rho_0 \\ \rho_0^* & 1 \end{bmatrix}$$

and

$$H_1 : C_1 = \sigma^2 \begin{bmatrix} 1 & \rho_1 \\ \rho_1^* & 1 \end{bmatrix},$$

where ρ_0 and ρ_1 are different real positive numbers representing two different normalized cross correlation factors. H_0 could, for instance, represent a pair with high cross correlation whereas H_1 could represent a pair with low cross correlation.

The likelihood ratio is defined in Eq. 13 in [9] as

$$\Lambda(X) = \frac{p_{x|H_1}(X|H_1)}{p_{x|H_0}(X|H_0)} \tag{6.2}$$

The log likelihood ratio using Eqs. 6.1 and 6.2 reduces to

$$log(\Lambda(X)) = b \cdot (\hat{R}_{11} + \hat{R}_{22}) \cdot \left(1 - c \cdot \frac{2Real(\hat{R}_{12})}{\hat{R}_{11} + \hat{R}_{22}}\right), \tag{6.3}$$

where b and c are constants given by ρ_0 and ρ_1 and $\hat{R}_{ij} = \frac{1}{d}\sum_{r=n-d}^{n-1} x_i(r)x_j^*(r)$.

The $\hat{R}_{ij}$ estimate is calculated as correlation between data at scan lines i and j at d depths given by sample numbers r. When averaging over several depths, $\hat{R}_{11}$ and $\hat{R}_{22}$ are approximately constant, and the latter part of the expression becomes a sufficient statistic. The correlation coefficient, being an optimal test for separating two different correlation values, then becomes:

$$C_c = \frac{2Real(\hat{R}_{ij})}{\hat{R}_{ii} + \hat{R}_{jj}}. \tag{6.4}$$

Due to the normalization, C_c will range from 0, when no correlation is found between the scan lines, to 1, when full correlation is found between the scan lines.

C_c can be calculated for each adjacent pair of scan lines as shown in Fig. 6.1. To compensate for gain variation along the scan lines, C_c can be calculated in sections along the scan lines and then averaged. The calculated final C_c for each scan line pair can be visualized in a C_c plot representing all scan line pairs.

C_c values and C_c plots contain information concerning the correlation from scan line to scan line. Of special interest regarding MLA are C_c values at transitions between MLA groups compared to C_c values within MLA groups. To get a single quantitative measure for this, an indicator of fractional correlation coefficient difference, D_c, can be calculated as:

$$D_c = \frac{\frac{1}{N}\sum_{ij\in W} C_c - \frac{1}{M}\sum_{ij\in T} C_c}{\frac{1}{N}\sum_{ij\in W} C_c} \cdot 100, \tag{6.5}$$

where ij is a pair of adjacent scan lines. The set W contains all such pairs within MLA groups, and the set T contains all such pairs located at transitions between MLA groups (such as correlation pair 4 in Fig. 6.1). N is the size of the set W, and M is the size of the set T. D_c will be 0 when no repeating difference in correlation within and between MLA groups is present. When there is full correlation within MLA groups and no correlation between MLA groups, it will be 100.

Table 6.1: Scan setup

Transmit frequency	2.5 MHz
Receive frequency	2.5 MHz
# receive lines	96
Sector width	75 deg
Beam spacing	0.79 deg
Transmit aperture width	7.5 mm
Receive aperture width	Expanding (max: 2.19 cm)
Transmit apodization	Rectangular
Receive apodization	Hamming
Transmit focus	70 mm
Receive focus	Dynamic

6.3 Setup

An M3S probe and a GE Vingmed System 7 scanner capable of recording RF data was set up with the specifications given in Table 6.1. Using this setup both 4MLA and single line acquisition (SLA) were implemented. The setup was designed to be able to compensate for the negative effects of MLA. Hamming apodization on receive lowers the side lobes. This results in less skewing due to more symmetric two way beam profiles. The small transmit aperture also reduces the skewing effect due to wider transmit beams. In addition, it results in a long focus, hence enabling good compensation for the warping and gain variation effect over a long depth range. The distribution of transmit and receive scan lines is visualized in Fig. 6.1. The warp compensation was implemented by steering the inner beams of the MLA groups an additional 14% of the beam spacing away from the transmit beam directions and the outer beams of the MLA groups an additional 42%. The compensation steering offsets were found through simulations of the described setup.

The recorded RF data were processed to B-mode display by detection, time gain compensation, log compression, and scan conversion. A 40-dB dynamic range was used in the images.

Using the described setup, an ultrasound phantom (CIRS Model 40, General Purpose Multi-Tissue Ultrasound Phantom, 0.5 dB/cm/Mhz; CIRS, Inc., Norfolk, VA) was imaged while tilting the probe from side to side. The left ventricle (LV) of the heart of a healthy adult subject was also imaged.

To isolate the effects of aberration, a thin silicon aberrator, described in [10], was placed between the probe and the phantom for some recordings. This was a pure time-delay aberrator with a RMS time delay of 48.5 ns. This is similar to RMS time delays found in [11]. Since the RMS delay value for this aberrator corresponded to an abdominal body wall, a scaled-down version of the aberrator was also tested in simulations. The RMS delay value of this scaled aberrator was set to 21.1 ns. This corresponds to typical values for thoracic body walls [12]. The correlation lengths of both aberrators were also in the range of typical thoracic body walls (2.47 mm) [12].

The described setup, aberrators, CIRS phantom, and a left ventricle computer

model were also simulated in Matlab using Field II [13]. The left ventricle computer model is described in [14]. When gain compensation was applied, the gain compensation values were estimated from the recorded data and applied to the RF data before further processing.

To produce a quantitative analysis of the images, C_c values between neighboring beams were calculated (a total of 95 pairs) using data from all frames of the recordings. To emphasize the difference in C_c values between scan lines within MLA groups and between groups, every fourth C_c value is colored brighter in the bar plots. C_c analysis was performed after the data were gain corrected.

Since the gain and warp compensation are valid only throughout the depth of focus, only data from the lower 2/3 part of each image were used when estimating both gain compensation and C_c values. The extent of this area is illustrated by a gray bar at the left side of the ultrasound sector in all images.

6.4 Results

All B-mode images in this section are also available as videos. The videos provide a far better impression of the described artifacts than the still images.

6.4.1 Measurements

With the described 4MLA setup, a frame rate of 163 frames/s was achieved on the scanner. An image of the left ventricle of a healthy adult subject acquired using this setup without warp compensation is shown in Fig. 6.2. Notice the block-like appearance.

Images of the CIRS phantom are presented in Figs. 6.3 and 6.4. In Fig. 6.3, the phantom was imaged using the 4MLA setup without warp and gain compensation. The block artifacts are observable in the image/video. The C_c plot shows a repeating pattern of three high C_c values followed by a lower C_c value. In Fig. 6.4, the described gain and warp compensation has been applied. No lateral block artifacts can be seen in this image, and the repeating pattern of three high C_c values followed by a lower C_c value is not present.

A cardiac ultrasound image with gain and warp compensation using the described 4MLA setup is shown in Fig. 6.5. The block artifacts are not as obvious as in Fig. 6.2, but they are still visible. When the C_c plot is observed, the repeating pattern of three high C_c values followed by a lower C_c value is evident. Using SLA but otherwise the same setup produced the image in Fig. 6.6. There is no repeating pattern in the corresponding C_c plot.

In Fig. 6.7, the aberrator was added to the phantom. The block artifacts appeared in the image. In the corresponding C_c plot, the pattern of three high C_c values followed by a lower C_c value is very obvious.

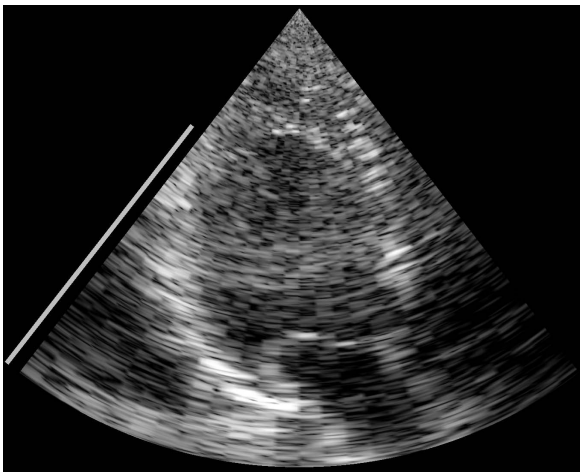

Figure 6.2: Human left ventricle imaged using the 4MLA setup without warp and gain compensation. *Thesis comment: A movie was published as part of the paper and is available at http://folk.ntnu.no/sveinaaa/Thesis/MLAAndAb/Movie02.mpg*

6.4.2 Simulations

To investigate the effect of aberration in a controlled environment, the 4MLA setup, CIRS phantom, left ventricle phantom, and silicon aberrator were implemented in Field II and Matlab. Fig. 6.8 shows the simulated results from imaging the CIRS phantom through the silicon aberrator. The B-mode image shows good correspondence with the recorded B-mode (Fig. 6.7). Fig. 6.9 shows the B-mode image and correlation values from a simulated cardiac situation. In this case, the CIRS phantom was replaced with the left ventricle phantom, and the aberration delays of the silicon aberrator were scaled to match the RMS delay values found in the literature for thoracic body walls. The block artifacts can still be seen in this B-mode image, particularly around the boundary of the ventricle model.

In the aberrated cases in all remaining figures, only the silicon aberrator was simulated. Fig. 6.10 shows four adjacent two-way beam profiles using the setup in Table 6.1 in six different imaging cases: SLA with and without aberration, uncompensated 4MLA with and without aberration, and compensated 4MLA with and without aberration. The figure illustrates the beam to beam variations of the beam profiles in the different imaging cases. In the 4MLA cases, the beam profiles of scan lines 47 and 48 belong to MLA group 12, and the beam profiles of scan lines 49 and 50 belong to MLA group 13. In the aberrated 4MLA cases (middle and bottom right plots), it can be seen that both the beam profile spacing and the beam profile shape are varying from beam to beam both before and after compensation.

In Fig. 6.11, the same imaging cases are investigated for lateral shift variance (LSV) of the point spread function (PSF). Such figures will be referred to as LSV plots. The procedure for creating LSV plots is illustrated in Fig. 6.12. First, a point

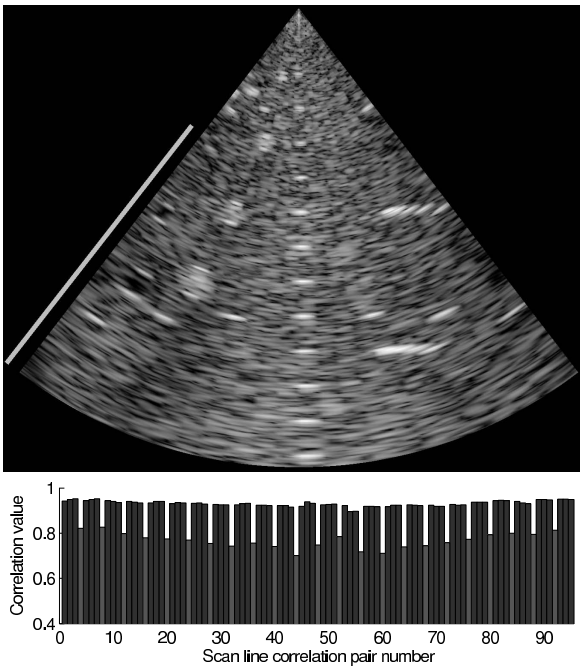

Figure 6.3: Phantom without aberrator imaged using the 4MLA setup without warp and gain compensation. *Thesis comment: A movie was published as part of the paper and is available at http://folk.ntnu.no/sveinaaa/Thesis/MLAAndAb/Movie03.mpg*

scatterer is imaged as it moves laterally at the focus depth (Fig. 6.12, top). Each image then corresponds to the PSF of the system at the position of the imaged point scatterer. Second, logarithmic radial mean square values of the point scatter images are calculated (Fig. 6.12, middle). Finally, the LSV plots are generated by stacking these logarithmic radial mean square values so that each row in the final LSV plot corresponds to a point scatterer position (Fig. 6.12, bottom). A shift invariant imaging system, where the PSF is independent of the position of the imaged point scatterer, should result in a straight diagonal structure. Deviations from a straight diagonal structure indicate that the PSF varies with lateral position and that the system is shift variant. The strong deviations from a diagonal structure in the bottom right pane of Fig. 6.11 indicate that this imaging system is shift variant. The structures visible in this pane are also similar to the block artifacts observed in the B-mode images.

Fig. 6.13 shows the aberrated beam profiles from three adjacent 4MLA groups. The figure shows on a larger scale the variation and pattern in the two-way beam profiles.

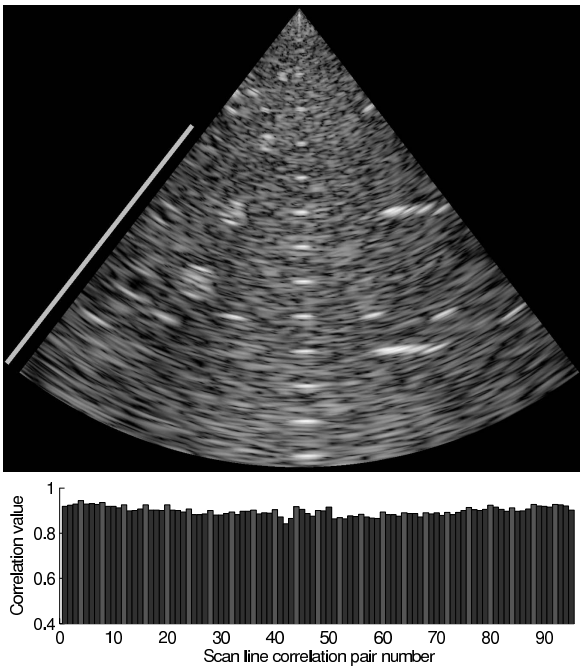

Figure 6.4: Phantom without aberrator imaged using the 4MLA setup with warp and gain compensation. *Thesis comment: A movie was published as part of the paper and is available at http://folk.ntnu.no/sveinaaa/Thesis/MLAAndAb/Movie04.mpg*

6.4.3 Simulated and Measured D_c Values

The indicator of correlation coefficient difference, D_c, was calculated for all images with C_c plots. The results are shown in Table 6.2 where "Phant." denotes measured phantom, "Sim. phant." is simulated phantom, "LV" is the measured left ventricle of a healthy subject, "Sim. LV" is a simulated left ventricle phantom, "ab.1" is aberration by thin silicon aberrator, "ab.C" is the aberration present in cardiac in vivo images, "ab.2" is aberration by thorax-scaled (simulated) silicon aberrator, and "Compensation" is warp and gain compensation.

All 4MLA setups with aberration had D_c values above 11. In the case of SLA with aberration (Fig. 6.6), the D_c value was, of course, low, as the MLA group size for SLA is one and no MLA related pattern was expected. In the case of no aberration and no MLA compensation (Fig. 6.3), a large D_c value was found. When MLA compensation was applied (Fig. 6.4), the D_c value was close to zero.

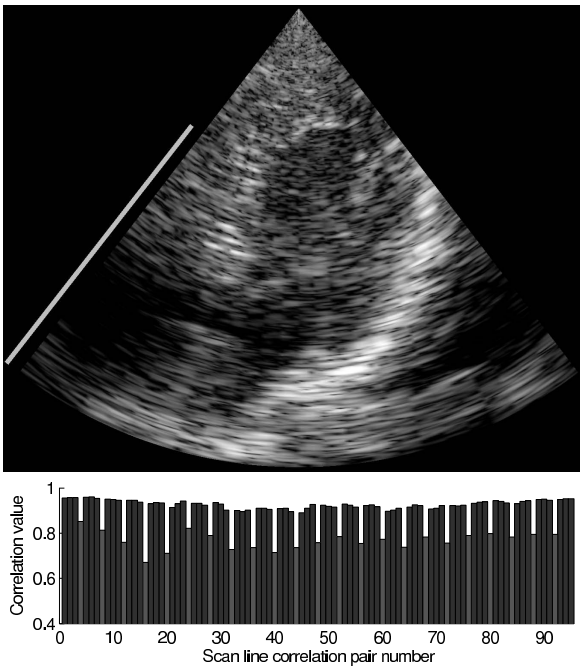

Figure 6.5: Human left ventricle imaged using the 4MLA setup with warp and gain compensation. *Thesis comment: A movie was published as part of the paper and is available at http://folk.ntnu.no/sveinaaa/Thesis/MLAAndAb/Movie05.mpg*

Table 6.2: Indicator showing differences in correlation, D_c

Object	Aberration	#MLA	Compensation	Figure	D_c
Phant.		4MLA	No	6.3	17.7
Phant.		4MLA	Yes	6.4	-1.5
Phant.	ab.1	4MLA	Yes	6.7	22.9
Sim. phant.	ab.1	4MLA	Yes	6.8	19.8
LV	ab.C	4MLA	Yes	6.5	17.4
LV	ab.C	SLA		6.6	0.02
Sim. LV	ab.2	4MLA	Yes	6.9	11.6

6.5 Discussion

The cardiac images recorded using 4MLA (Figs. 6.2 and 6.5) showed block artifacts. Although the artifacts were reduced by using warp compensation (Fig. 6.5), they were still visible.

To first study a simpler situation, a tissue mimicking phantom was used. The results showed that block artifacts in unaberrated 4MLA phantom images can be avoided by using warp and gain compensation (Figs. 6.3 and 6.4). The beam profiles

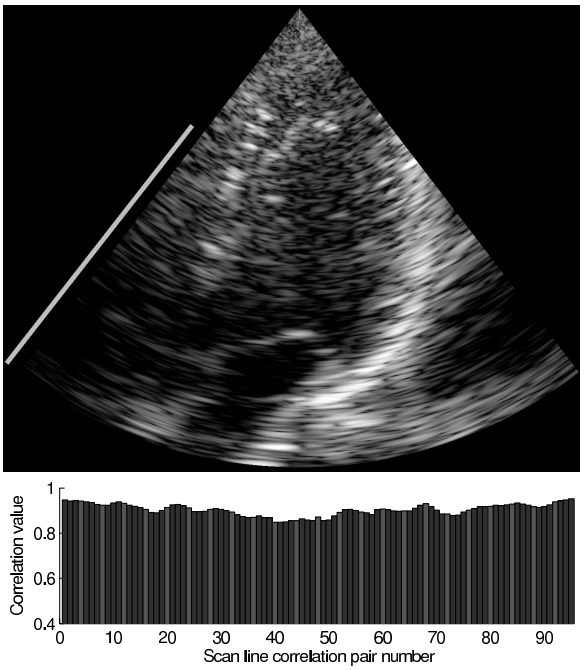

Figure 6.6: Human left ventricle imaged using the SLA setup (96 transmit beams). *Thesis comment: A movie was published as part of the paper and is available at http://folk.ntnu.no/sveinaaa/Thesis/MLAAndAb/Movie06.mpg*

in the two lower left panes of Fig. 6.10 correspond to Figs. 6.3 and 6.4, respectively. From the beam profiles, it is evident that warping is the main distorting effect. Skewing is not observable.

To emulate aberration, the thin silicon aberrator was placed between the probe and the phantom. Even though warp and gain compensation was applied, the block artifacts appeared and the C_c plot showed a repeating pattern of three high/one low C_c values (Fig. 6.7). This was the exact same setup as used when imaging the heart (Fig. 6.5). As shown in both images and both C_c plots, the same pattern emerged. This implies that the thin silicon aberrator generates some of the beam manipulating effects that influence cardiac images. Cardiac images without the use of MLA (Fig. 6.6) did not contain block artifacts and corresponding patterns in the C_c plots. These observations suggest that the combination of aberration and MLA cause the block artifacts.

The simulations supported the results from the measurements, showing that the introduction of an aberrator produces pronounced artifacts in the images. With good agreement between simulated and measured results, further insight was obtained from investigations of the aberrated beam profiles.

Fig. 6.10 shows the two-way beam profiles for four adjacent scan lines in six

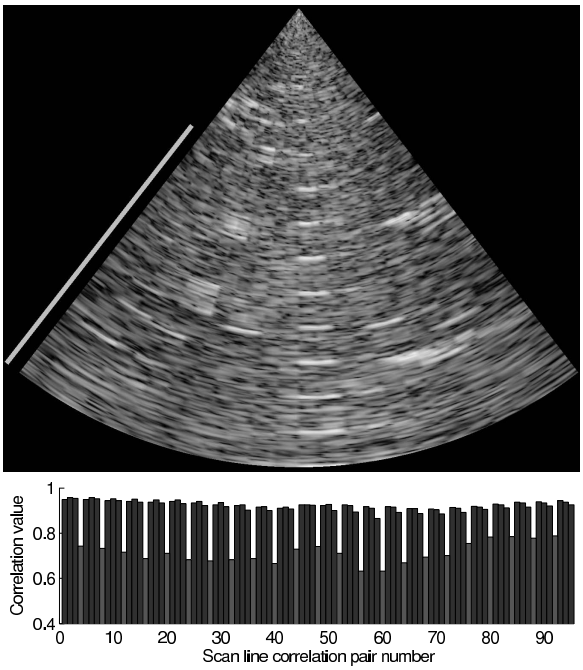

Figure 6.7: Phantom with aberrator imaged using the 4MLA setup with warp and gain compensation. *Thesis comment: A movie was published as part of the paper and is available at http://folk.ntnu.no/sveinaaa/Thesis/MLAAndAb/Movie07.mpg*

different imaging cases. On the left side, the beam profiles for the unaberrated case are presented. Using SLA (top left plot), the beam profiles are regularly spaced with maximum sensitivity in the desired steering directions. For the 4MLA case (middle left plot), the beam profiles become irregularly spaced. Scan line 48 and 49 belongs to two different MLA groups. The gap between the beam profiles from these two scan lines results in a decorrelation that appears as a sharp lateral discontinuity in the B-mode image. Several such gaps cause the blocky appearance in the B-mode images. The larger this gap is, the more pronounced the artifacts will be. Such block artifacts and decorrelation can be seen in Fig. 6.3. In the bottom left plot of Fig. 6.10, warp compensation has been applied. Since the beam profiles now once again are regularly spaced, the block artifacts are no longer present in the images (Fig. 6.4). Proceeding to the aberrated SLA case (top right plot), the two-way beam profiles are clearly distorted. However, it is worth noticing that the shape and overlap between each adjacent beam is similar. Regular sampling is thus also achieved for the aberrated case. With regular sampling, the correlation between each adjacent beam will be similar. This is confirmed by the C_c plot in Fig. 6.6. In the middle right plot of Fig. 6.10, the beam profiles for the aberrated, uncompensated 4MLA case are shown. Here, each scan line beam profile is different in shape and the spacing is irregular.

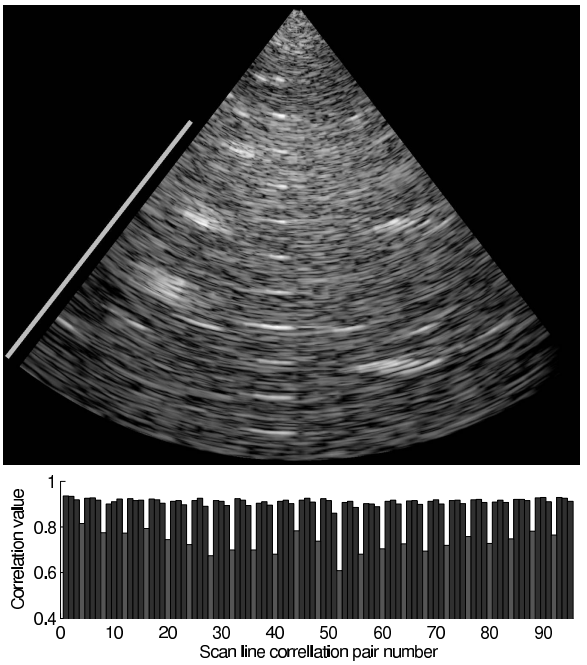

Figure 6.8: Phantom with aberrator simulated using the 4MLA setup with warp and gain compensation. *Thesis comment: A movie was published as part of the paper and is available at http://folk.ntnu.no/sveinaaa/Thesis/MLAAndAb/Movie08.mpg*

One can expect high correlation between scan lines 47 and 48 due to the large overlap between the beam profiles. Similarly, one can expect low correlation between scan lines 48 and 49 due to significantly less overlap. As in the uncompensated 4MLA case without aberration, this reduction in correlation will appear in the image as sharp lateral discontinuities between each MLA group, such as seen in the cardiac B-mode image in Fig. 6.2. The bottom right plot in Fig. 6.10 shows the beam profiles for warp-compensated 4MLA with aberration. The compensation results in a slightly more regular spacing of the beam profiles, but the fluctuation in the shape of the beam profiles still remains. Compared to the unaberrated, compensated 4MLA case, the compensation in the aberrated case is far from successful. This can also be seen in the simulated, aberrated B-mode image (Fig. 6.8), where the block artifacts are obvious.

Seemingly, the MLA artifacts were more visible when imaging objects with high dynamic range in the back scattering, such as the left ventricle phantom. The B-mode image of this phantom (Fig. 6.9) was generated using the default scan setup, 4MLA, and thorax-scaled aberration. Despite a significantly weaker aberrator, block artifacts can still clearly be seen in the image, particularly around the boundary of the ventricle model. The explanation for this can be found from the two-way beam profiles in Fig.

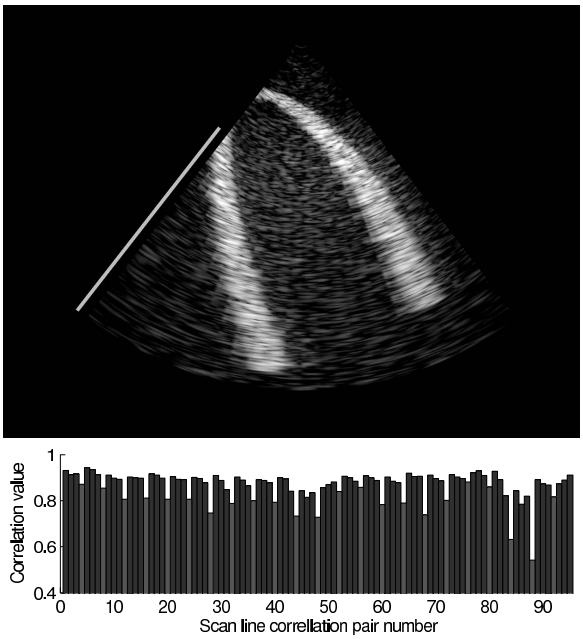

Figure 6.9: Left ventricle model with aberrator scaled according to thoracic delay values simulated using the 4MLA setup with warp and gain compensation. *Thesis comment: A movie was published as part of the paper and is available at http://folk.ntnu.no/sveinaaa/Thesis/MLAAndAb/Movie09.mpg*

6.13. This figure shows two way beam profiles from three adjacent MLA groups in the compensated, aberrated 4MLA case. A beam profile defines the lateral sensitivity of a scan line. With that in mind, consider a point scatterer positioned from an angle around -1.5 degrees to 1.5 degrees. This point scatterer will be perceived approximately equally bright in all of the scan lines generated from the beam profiles in solid line style. In the scan lines generated from the dashed beam profiles, it will, however, be perceived significantly brighter and have different brightness values in each scan line. The result is a lateral plateau of four almost equal brightness values followed by a jump in brightness value. For a point scatterer moving laterally through the scan grid, the resulting pattern is shown in the bottom right pane of Fig. 6.11. When imaging the heart, a situation similar to the one in Fig. 6.9, a transition between two areas with low and high back scattering intensity will produce the same image artifact.

Some areas of the cardiac images and the simulated cardiac situation (Figs. 6.2, 6.5 and 6.9) can give an impression of axial block artifacts. With irregular lateral sampling, the speckle pattern will not be continuous laterally. This may cause an impression of discontinuous speckle in the radial direction. For areas with high dynamic range in the back scattering, the effect can also be explained as a perception of the lateral plateau artifacts described in the previous paragraph.

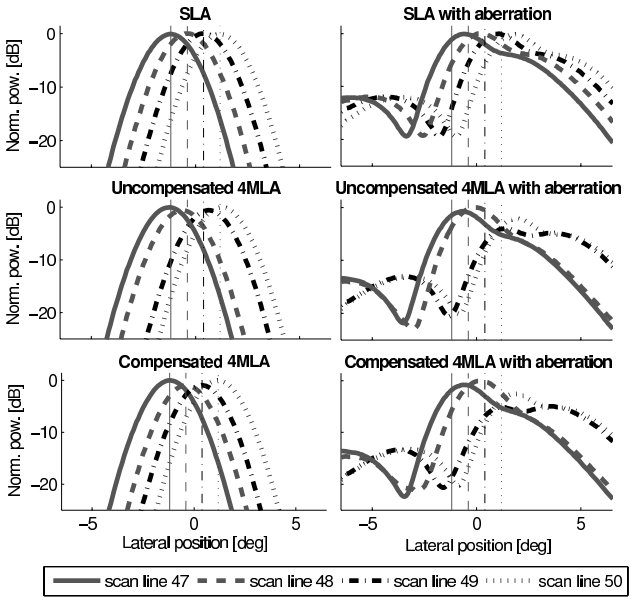

Figure 6.10: Simulated two-way beam profiles from four adjacent scan lines. The applied setup is given in Table 6.1. The vertical lines indicate the desired steering direction of the beam profiles in corresponding line style. Ideally these lines should intersect their beam profiles at their maximum. Left side: Without aberration. Right side: With aberration. Top: SLA. Middle: Uncompensated 4MLA. Bottom: Compensated 4MLA. In the 4MLA cases, the beam profiles in solid and dashed line style are the two last beams in a 4MLA group. The beam profiles in dash-dotted and dotted line style are the first two beams from the adjacent 4MLA group. Notice that with the combination of 4MLA and aberration, each scan line beam profile is different in shape, has different gain, and has irregular spacing.

Fig. 6.11 shows how the point spread function varies in shape as a function of lateral position. The figure contains the same cases as for the beam profiles in Fig. 6.10. In the unaberrated case, the shift invariance property can be restored by warp compensation (from the middle left pane to the bottom left pane). In the aberrated 4MLA case, the compensation does not suffice, and the imaging system remains shift variant (middle right pane and bottom right pane). This confirms the measured results.

Both the measured and simulated results showed that repeating patterns in the C_c plots were related to the presence of block artifacts in the corresponding B-mode images. The D_c values shown in Table 6.2 quantify the magnitude of these patterns and confirm the impression from images and C_c plots. The situation with 4MLA without aberration (Fig. 6.4) produced a negative D_c value. This indicates that the correlation at transitions between MLA groups was stronger than within the MLA groups. The reason for this might be overcompensation for the warping effect.

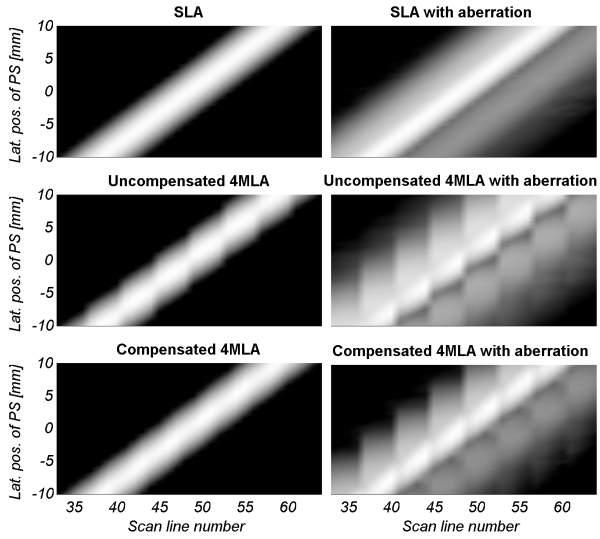

Figure 6.11: Lateral shift variance plots. Left side: Without aberration. Right side: With aberration. Top: SLA. Middle: Uncompensated 4MLA. Bottom: Compensated 4MLA. All figures are displayed with a 40-dB dynamic range.

Larger D_c values were measured with the aberrated phantom images than in the cardiac images. This was probably because the RMS delay values of the silicon aberrator were from abdominal measurements. To investigate a cardiac imaging situation, the aberrator was scaled to thoracic RMS delay values in simulations and used to image the left ventricle computer phantom. The resulting image and C_c plot (Fig. 6.9) still showed block artifacts. The D_c value was, however, lower than in the measured cardiac case. A reason for this might be that aberrations from a thick body wall were approximated with a single phase screen at the face of the transducer. Results from [15, 16] show that this approximation models only parts of the total aberration. Another reason might be further aberrations from structures beyond the body wall. A third reason might be reverberations. In the in vivo recording, reverberations with evident block artifacts were visible within the cavity. Such effects were not included in the simulations. Additionally, the LV phantom is a coarse approximation of an in vivo left ventricle. All of these factors may have contributed to make the D_c value of the simulated cardiac situation lower than in the measured situation.

The D_c value and corresponding C_c plot of Fig. 6.3 show that warping alone (no skewing present, see Fig. 6.10, middle left) will cause measurable decorrelation. Aberration in combination with MLA produces both warping and skewing effects and results in measurable decorrelation (Figs. 6.5, 6.7, 6.8, 6.9 and beam profiles in Fig. 6.10, lower right). The isolated effect of skewing on decorrelation has not been investigated. Although the D_c value of Fig. 6.3 was high, block artifacts in the

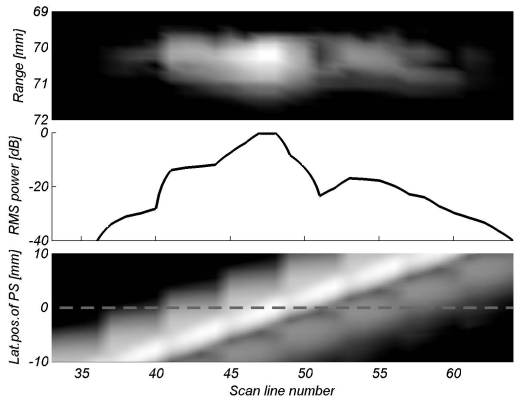

Figure 6.12: Illustration of how LSV plots are generated. Top: Image of a point scatterer at a lateral position at focus depth. Middle: Radial mean square value of the point scatterer image. Bottom: Stacked radial mean square values for several point scatterer positions. The dashed line indicates the position of the radial mean square value in the middle pane.

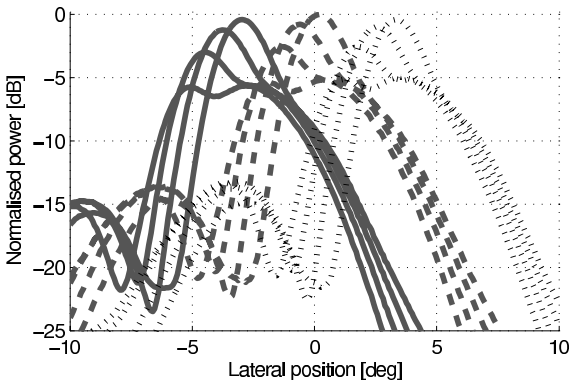

Figure 6.13: Two-way beam profiles from three adjacent 4MLA groups. The simulation setup was 4MLA with aberration and warp compensation. Group 11 plotted in solid, group 12 in dashed and group 13 in dotted line style.

image were weak but observable. This might be related to the absence of skewing, but also possibly to the uniformity of the imaged object. In Fig. 6.8 (strong aberrator, relatively uniform phantom) and Fig. 6.9 (weak aberrator, non uniform phantom), the block artifacts are approximately equally visible. This indicates that the block artifacts are more easily detected visually in images of non uniform objects.

6.6 Conclusions

Simulations and in vitro experiments showed that aberration in combination with parallel beamforming caused block artifacts similar to the artifacts observed in cardiac parallel beamforming images. Gain and beam steering compensation successful in non-aberrated in vitro cases failed in aberrated in vitro cases.

During investigation of simulated beam profiles, two underlying mechanisms were identified. The first mechanism was irregular sampling and decorrelation. This was caused by aberration distorting and pulling the beam profiles out of the original scan grid, leaving gaps between the parallel receive groups. Second, the asymmetric and variable shape of the beam profiles caused a stair-like gain variation in transitions between imaged areas with low and high intensity.

Acknowledgement

The authors thank GE Vingmed Ultrasound for access to the Vivid 7 ultrasound scanner.

References

[1] O. T. von Ramm, S. W. Smith, and H. G. Pavy, "High-speed ultrasound volumetric imaging system – part II: Parallel processing and image display," *IEEE Trans Ultrason Ferroelectr Freq Control*, vol. 38, pp. 109–115, March 1991.

[2] D. P. Shattuck, M. D. Weinshenker, S. W. Smith, and O. T. von Ramm, "Explososcan: A parallel processing technique for high speed ultrasound imaging with linear phased arrays," *J Acoust Soc Amer*, vol. 75, no. 4, pp. 1273–1282, 1984.

[3] T. Hergum, T. Bjåstad, and H. Torp, "Parallel beamforming using synthetic transmit beams," *Proc IEEE Ultrason Symp*, vol. 2, pp. 1401–4, 2004.

[4] G. L. Holley and I. M. Guracar, "Ultrasound multi-beam distortion correction system and method." U.S. Patent 5.779.640, July 14 1998.

[5] J. N. Wright, S. H. Maslak, D. J. Finger, and A. Gee, "Method and apparatus for coherent image formation." U.S. Patent 5.623.928, Apr. 29 1997.

[6] D.-L. D. Liu, J. C. Lazenby, Z. Banjanin, and B. A. McDermot, "System and method for reduction of parallel beamforming artifacts." U.S. Patent 6.447.452, Sep. 10 2002.

[7] T. J. Hunt, B. M. Herrick, K. K. Robertson, and J. M. Ziel, "Ultrasonic imaging system using line splicing and parallel receive beam formation." U.S. patent 5.462.057, Oct. 31 1995.

[8] S. M. Kay, *Fundamentals of Statistical Signal Processing: Estimation Theory.* Indianapolis, IN: Prentice-Hall PTR, 1993.

[9] H. L. V. Trees, *Detection, Estimation and Modulation Theory, Part I: Detection, Estimation, and Linear Modulation Theory.* New York: Wiley, 2001.

[10] T. F. Johansen, B. A. J. Angelsen, and W. Nordhøy, "Phase aberrations - Experiments and simulations," *Proc 23rd Scand Symp Phys Acoust*, pp. 57–60, 2000.

[11] L. M. Hinkelman, D.-L. Liu, L. A. Metlay, and R. C. Waag, "Measurements of ultrasonic pulse arrival time and energy level variations produced by propagation through abdominal wall," *J Acoust Soc Am*, vol. 95, no. 1, pp. 530–541, 1994.

[12] L. M. Hinkelman, T. L. Szabo, and R. C. Waag, "Measurements of ultrasonic pulse distortion produced by human chest wall," *J Acoust Soc Am*, vol. 101, no. 4, pp. 2365–2373, 1997.

[13] J. A. Jensen and N. B. Svendsen, "Calculation of pressure fields from arbitrarily shaped, apodized, and excited ultrasound transducers," *IEEE Trans Ultrason Ferroelectr Freq Control*, vol. 39, pp. 262–267, 1992.

[14] S. Rabben, A. Haukanes, and F. Irgens, "A kinematic model for simulating physiological left ventricular deformation patterns - a tool for evaluation of myocardial strain imaging," *Proc IEEE Ultrason Symp*, pp. 134–7, 2003.

[15] L. M. Hinkelman, T. D. Mast, L. A. Metlay, and R. C. Waag, "The effect of abdominal wall morphology on ultrasonic pulse distortion. part i. measurements," *J Acoust Soc Am*, vol. 104, no. 6, pp. 3635–3649, 1998.

[16] T. D. Mast, L. M. Hinkelman, M. J. Orr, V. W. Sparrow, and R. C. Waag, "Simulation of ultrasonic pulse propagation through the abdominal wall," *J Acoust Soc Am*, vol. 102, no. 2, pp. 1177–1190, 1997.

Appendix A

Aortic Valve Closure: relation to tissue velocities by tissue Doppler imaging and speckle tracking in a subject with infarction

Svein Arne Aase[1], Asbjørn Stoylen[1,2], Charlotte Björk-Ingul[1], Anders Thorstensen[1] and Hans Torp[1]
[1] Dept. Circulation and Medical Imaging, NTNU
[2] Dept. Cardiology, St. Olav Hospital, Trondheim, Norway

There is no common consensus in literature regarding the exact event representing Aortic Valve Closure (AVC) in tissue Doppler (TDI) velocity/time curves, neither in normal subjects nor in pathological curves. In this small example the timing of AVC as visually seen in high frame rate B-mode images of the aortic valve is compared with simultaneously recorded apical TDI and speckle tracking based velocity/time curves in a subject with inferior infarction.
The acquisition frame rate was modified to be equal for both TDI and B-mode (137.7 FPS). A narrow sector view covering the basal septum and the aortic valve was used to increase frame rate.
In this example, AVC as visible in the B-mode images occurred 47.8 ms later than the initial negative velocities after ejection in a TDI velocity/time curve from basal septum.

A.1 Introduction

Timing of Aortic Valve Closure (AVC) is important when analyzing cardiac data. The relation between events in velocity/time curves and AVC as seen in B-mode images in normals has been investigated in a previous article [1]. In this short article a comparison of AVC in high frame rate B-mode and tissue Doppler imaging (TDI)/speckle tracking based velocity/time curves is done in a subject with coronary infarction. This affects the inferior regions and can also affect the basal inferior septum of the left ventricle.

A.2 Methods

A Vivid 7 (GE Vingmed Ultrasound AS, Horten, Norway) ultrasound scanner with a M3S probe was used to examine a patient with inferior infarction. The study was approved by the regional ethical committee. Written informed consent from the examined subject was obtained. To achieve high frame rate, scanning was limited to a narrow sector covering the septum and the aortic valve. An apical long axis plane was used.

B-mode and TDI were recorded simultaneously and the instrument settings were modified for TDI and B-mode frame rate to be equal. The frame rate was 137.7 frames/s in both B-mode and TDI. This B-mode frame rate is almost three times higher than normal B-mode frame rates for full sector scanning. All analysis was performed using the GcMat (GE Vingmed Ultrasound AS, Horten, Norway) ultrasound analysis software.

The temporal position of AVC was found by visual inspection of the B-mode images as the first frame where the aortic valve was closed. At this frame the valve no longer moved independently of the aortic root. Practically, finding this frame was done in the analysis software by stepping forward and backward frame by frame and finally extracting the time stamp of the selected frame.

TDI velocity/time curves from basal septum was extracted. Radial averaging of 0.5

cm was used for calculating velocities. A velocity/time curve by speckle tracking was also produced using the speckle tracking approach described in the article concerning normal subjects [1].

The following time points were identified in both curves: the time point of initial negative velocity after ejection, the time point of peak negative velocity after ejection before the E-wave, the time point of peak positive acceleration after ejection before the E-wave and the time point of zero crossing after the initial negative velocities. All time points were compared to the time point of the chosen B-mode AVC frame.

A.3 Results

Selected B-mode frames and TDI and speckle tracking based velocity/time curves are shown in Figure A.1. B-mode frame 203 was chosen to represent AVC.

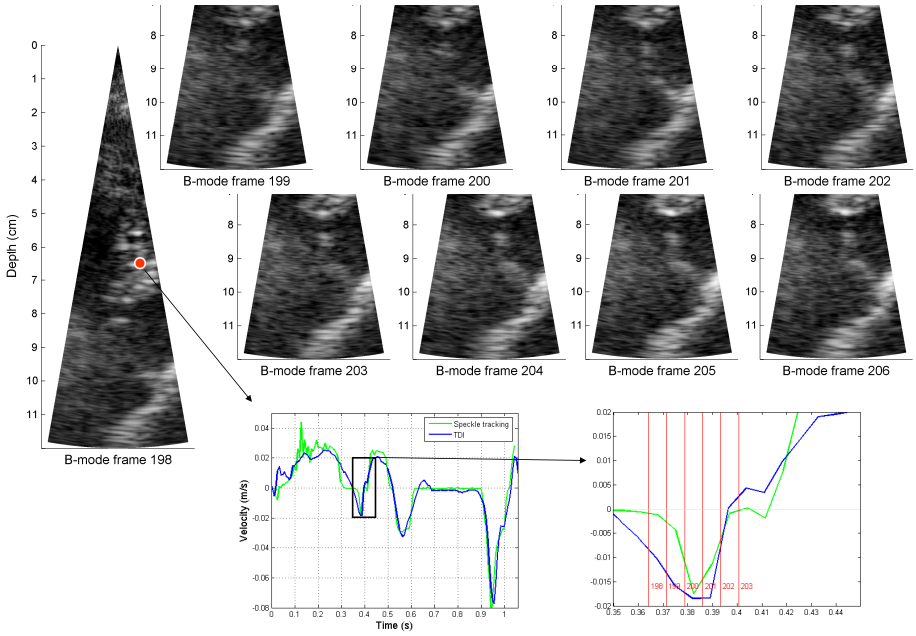

Figure A.1: Comparison between aortic valve closure as visible in high frame rate B-mode images and velocity/time curves. By the B-mode images the valve was determined to be closed in frame 203. The cusps move independently of the aortic root from frame 202 to 203. This can be seen as in frame 203 the cusps are more curved than in frame 202. From the TDI velocity/time curve, this event is clearly later than the start of negative velocities after ejection.

The time point of the first negative velocity sample after ejection in the TDI velocity/time curve occurred 47.7 ms before the time stamp of B-mode frame 203. The

corresponding time point in the speckle tracking based velocity/time curve occurred 83.6 ms before B-mode frame 203. The time point of peak negative velocity after ejection before the E-wave occurred 18.7 ms before the reference in TDI and 18.2 ms before with speckle tracking. The time point of peak positive acceleration after ejection before the E-wave occurred 7.8 ms before the reference in TDI and 7.3 ms before with speckle tracking. The time point of zero crossing after the initial negative velocities after ejection and before the E-wave occurred 4.2 ms before the reference in the TDI curve and 2.2 ms after the reference in the speckle tracking curve.

A.4 Summary

An inferior infarction will affect the basal inferior septum as visible in an apical 4CH plane more than the basal anterior septum as visible in an apical long-axis plane. But as the basal velocities are a function of the global left ventricular function, the velocities of the basal anterior septum are also often affected. From Figure A.1 this is evident, as peak post-systolic velocity is almost as high as peak systolic velocity. Thus, the curve is pathological, and despite this, AVC candidates can be accurately detected in the velocity/time curve. The sensitivity and specificity of AVC detection still has to be addressed in a study, but this case shows it to be possible. However, large anterior infarctions would affect the anterior septum to a greater degree and this may affect the accuracy of AVC detection more than in the present case.

Aortic valve closure as visible in the high frame rate B-mode images clearly occurred later than the time point of initial negative velocities in both TDI and speckle tracking velocity/time curves. From this example it seems that the time point of zero crossing after the initial negative velocities after ejection is a more representative event for AVC also in pathological velocity/time curves.

References

[1] S. A. Aase, A. Stoylen, and H. Torp, "Aortic valve closure: relation to tissue velocities by doppler and speckle tracking in normal subjects," *Accepted for publication in Eur J Echocardiogr*, 2008.